creative commons
COMMONS DEED

저작자표시-비영리-변경금지 2.0 대한민국

이용자는 아래의 조건을 따르는 경우에 한하여 자유롭게

- 이 저작물을 복제, 배포, 전송, 전시, 공연 및 방송할 수 있습니다.

다음과 같은 조건을 따라야 합니다:

저작자표시. 귀하는 원저작자를 표시하여야 합니다.

비영리. 귀하는 이 저작물을 영리 목적으로 이용할 수 없습니다.

변경금지. 귀하는 이 저작물을 개작, 변형 또는 가공할 수 없습니다.

- 귀하는, 이 저작물의 재이용이나 배포의 경우, 이 저작물에 적용된 이용허락조건을 명확하게 나타내어야 합니다.
- 저작권자로부터 별도의 허가를 받으면 이러한 조건들은 적용되지 않습니다.

저작권법에 따른 이용자의 권리는 위의 내용에 의하여 영향을 받지 않습니다.

이것은 이용허락규약(Legal Code)을 이해하기 쉽게 요약한 것입니다.

Disclaimer

dCollection

공학박사학위논문

A multiscale analysis and design of the light-responsive liquid crystal polymer using nonlinear finite element shell model

비선형 쉘 유한요소모델에 기반한 광반응 액정 고분자의 멀티스케일 해석 및 설계

2017 년 2 월

서울대학교 대학원

기계항공공학부

정 하 영

A multiscale analysis and design of the light-responsive liquid crystal polymer using nonlinear finite element shell model

비선형 쉘 유한요소모델에 기반한 광반응 액정 고분자의 멀티스케일 해석 및 설계

지도교수 조 맹 효

이 논문을 공학박사 학위논문으로 제출함

2016년 10월

서울대학교 대학원

기계항공공학부

정 하 영

정하영의 공학박사 학위논문을 인준함

2016년 12월

위 원 장 : ____________________

부위원장 : ____________________

위 원 : ____________________

위 원 : ____________________

위 원 : ____________________

ABSTRACT

The term, liquid crystal polymer (LCP), broadly refers to a hybrid structure where short and rigid liquid crystal molecules are incorporated within long and flexible polymeric chain networks. Interestingly, the combination of these two classical components has been proven to generate the coupled behaviors that render the LCP as a novel, smart material; the stimuli-responsive phase change (e.g., thermotropic) of the chromophores is reflected to the conformation of the polymer and changes the macroscopic shape of the LCP. It was recently revealed that the LCP can also be reversely actuated by light, given that the chromophores contain light-sensitive structures such as azo-benzenes. In this way, many applications are envisaged and realized, including light-driven mechanical mechanisms such as actuators, sensors, propellers, and even tweezers.

However, much of our knowledge regarding these anomalous spontaneous mechanisms is largely driven by experiments and simple analytic models because of the complex interplays between distinctive physics: light-LC, phase change-polymeric conformation, and microstate-to-macroscopic deformation. Therefore, there is a dire need for a framework that considers these distinctive physics, as well as the interdisciplinary interactions that emerge at the vicinity. To this end, this dissertation proposes a multiscale analysis framework for the photomechanical behavior of LCP. This consists of nonlinear finite element analysis and in-silico experiments to advance our understanding of the microscopic nature of LCPs.

In the first part of the dissertation, the theoretical bases found in the proposed multiscale analysis are described in depth. The present work employs finite element analysis as the solution of the photomechanical system that is equivalent to finding stress-free configurations of the LCP structures under various internal stresses that are induced by light. Herein, uniaxial liquid crystal (LC) configurations are assumed; this encompasses rotational symmetry (i.e., nematic) as well as translational symmetry (i.e., smectic). Hence, a variationally consistent constitutive equation that couples the stimuli to the stress-strain relation is described. Furthermore, in contrast to existing finite element analysis on LCP, which assumes a global linearity to simplify the problem, two sources of the nonlinearity—geometric nonlinearity and nonlinear thermomechanical behaviors—are considered. First, geometric nonlinearity is included in the model because many of the observed light-induced deflections undergo a large displacement, yet their local strains remain in the infinitesimal range. An element independent corotational formulation is utilized to consider such nonlinearity, which is saliently beneficial for both the computation and further sensitivity analysis. A molecular dynamics simulation is also undertaken in order to reveal the unprecedented nonlinearity accompanied by phase change found in the crosslinked mesogens. The fidelity of the present multiscale solutions is examined with available experiments.

In the second part of the dissertation, the possible extension of the multiscale framework to the design of LCP photo actuations is exemplified by facilitating the multi-scale nature of the material, which is the combination of microscale properties, such as the local alignment of LC, and macroscopic properties, such as the shape of the LCP or the distributions of the stimuli. The proposed results are categorized into modifications of the extrinsic (post-crosslinking) variables and the intrinsic (pre-crosslinking) variables. The influence that each variable has on the deformation is described and discussed for the first time by examining the sensitivity towards the stimuli. With regards to the extrinsic variables, the various directions of the uniaxial orientation of the LCP are studied for the first time, and the resulting change in the light-induced principal curvature direction is shown. Envisaged by the possible high-fidelity light control, a light-patterning schematic is also proposed to achieve the desired shape change. A topology optimization method, which was originally devised to compute lightweight and load-sustaining structures, is employed to compute the discrete light patterns that drive the LCP to become a desired shape specified a priori. In view of the intrinsic variables, the distorted textures of nematic LC are examined, which are possibly obtained using novel alignment techniques. An LCP with twisted nematic configuration is studied and compared to existing works based on either analytic calculations or experiments. The arbitrary textures prescribed to the LCP surface are also simulated to show the exotic shape change that consists of many hills-and-valley configurations and to determine their ability to induce photo-generated instability.

In this regard, the proposed model could possibly provide an efficient and consistent framework in which to analyze LCP behavior with complex internal structures and combined stimuli. Hence, the design of novel mechanical elements driven by light is facilitated whenever large, complex, and precise manipulation is valued over load-carrying capability.

Keywords: *liquid crystal polymer, finite element analysis, multiscale analysis, sensitivity analysis, mechanical instability, optimization*

Student number: 2010-24073

TABLE OF CONTENTS

ABSTRACT i

LIST OF FIGURES vi

LIST OF TABLES ix

Chapter 1. Introduction 1

- 1.1. Liquid crystal polymer (LCP) 1
  - 1.1.1. A self-organizing characteristic of LC 2
  - 1.1.2. LC-driven properties of LCP 3
  - 1.1.3. Synthesis: from LC alignment to Polymer Crosslinking 5
- 1.2. Theoretic Background 7
  - 1.2.1. Thermo-opto-mechanical coupling 8
  - 1.2.2. Liquid crystalline phase behavior and the microstate change 10
  - 1.2.3. Multiscale / Multiphysics coupled nature 12
- 1.3. Motivations 14
- 1.4. Organization of the present dissertation 15

Chapter 2. Multiscale photomechanical analysis of LCP 19

- 2.1. Overview of multiscale analysis of LCP 19
- 2.2. Geometric nonlinear shell formulation 23
  - 2.2.1. Kinematics-based corotational formulation 24
- 2.3. Thermo-mechanical characterization 28
  - 2.3.1. Nematic LCP 29
  - 2.3.2. Smectic-A LCP 36
- 2.4. Light-induced deflection of nematic solid 46
  - 2.4.1. Geometric nonlinearity and non-monotonicity of photobending 48
  - 2.4.2. Nonlinearity from the microscale origin 51
- 2.5. Light-induced deflection of smectic solid 54
  - 2.5.1. Pre-transitional phase behavior 55
  - 2.5.2. Light-induced bending of smectic solids 56
- 2.6. Light-induced deflection of solids with distorted nematic 60
  - 2.6.1. Curvature evolution due to distorted nematics 61

2.6.2. Experiments on TN-LCP 63
Chapter 3. Designs of LCP actuation 90
3.1. Changes of extrinsic variables: geometry and orientation 90
3.1.1. Directional orientations of nematic LCP 91
3.1.2. Directional orientations of smectic solids 92
3.1.3. Anticlastic behavior of nematic LCP 93
3.2. Optimum extrinsic property: irradiation pattern 94
3.2.1. Methodology based on topology optimization 95
3.2.2. Numerical examples on light-fueled gripper 100
3.3. Changes of intrinsic variables: Texture design for the actuation 107
3.3.1. Frank elasticity and nematic texture 107
3.3.2. Texture induced exotic shape change 111
3.3.3. Snap-through instability of LCP with Hedgehog defect 113
Chapter 4. Concluding remarks 127
References 131

LIST OF FIGURES

Figure Page

1.1.1. Illustration for the phase change of thermotropic liquid crystal 17

1.1.2. A chemical compounds that constitutes the LCP 17

1.1.3. The examples of light-responsive manipulation. The figures at the 2nd row are adapted from the references. 18

2.1.1. Multiscale schematics 67

2.2.1. Kinematics of EICR 68

2.2.2. Three-node shell formulation with 18 DOF and nematic orientation 68

2.2.3. The effect of the number of integration points within thickness on the numerical integration for mid-plane properties of nematic solids 69

2.3.1. Unit cell of a photo-responsive polymer network (LCP) with *cis*-population $n_{\text{cis}} = 0.25$ 70

2.3.2. Time-dependent bending deformation of photo-responsive polymer networks (LCPs) 71

2.3.3. Order parameter s^*, ρ_o^*, q_0^* with increasing temperature 72

2.4.1. LCP model configurations. (a) Model geometry with length, thickness, and mesogenic director ***n*** 73

2.4.2. Curvature of the cantilevered LCP 74

2.4.3. Shape change of LCP sheet with radial disclination-defect-induced instability 75

2.4.4. Photo-responsive LCP bending induced by light travelling in the –z direction 76

2.4.5. Time-dependent bending deformation of photo-responsive LCP 77

2.4.6. Bending deformation of photo-responsive LCP computed via multiscale framework compared to the classical model..78

2.5.1. Uniaxial shrinkage due to phase change of the smectic solids with different layer modulus D 79

2.5.2. Flowchart of the photomechanical analysis on smectic solids.........................79

2.5.3. Profile of light-induced derivatives in out-of-plane direction..........................80

2.5.4. Temperature dependence of photo-responsive behavior with increasing light intensity in terms of curvature 80

2.5.5. Deformed shape of smectic solids with internal change.................................81

2.5.6. Effect of nonlinearity depending on the temperature and intensity (inset) of the bent geometry of the smectic solid 81

2.6.1. Evolution of shape parameter and principal curvature...................................82

2.6.2. Characterization of synthesized TN glass cell 83

2.6.3. Experimental setup for TN specimen and the image processing 84

2.6.4. Computation of penetration depth *d* of TN strip 84

3.1.1. Effect of director rotation on the bending direction, and the emergence of twist-bend coupling 116

3.1.2. Alternation of the bending curvature depending on the uniformly deviated angle θ between layer normal $\vec{n}$ and the longitudinal direction, with fixed temperature $T = 330$ K..116

3.1.3. “Swimming” non-square LCP sheet under illumination for different aspect ratios R_x/R_y..117

3.2.1. (a) Convergence for iteration number and (b) intermediate pattern shapes found during optimization 118

3.2.2. Bending behavior and strain distribution with different *S* constraints 118

3.2.3. Curvature-constrained strain pattern 119

3.2.4. Bending behavior with various pinching location, and strain patterns obtained... 119

3.3.1. Optical textures naturally arising in relaxed state of liquid crystal distortion 120

3.3.2. Illustration of light-induced deformations whose topographies are indicated by the same alphabetic indicators as in Fig. 3.4.1.............................. 120

3.3.3. Photo-induced textures generated by nematic textures with disclination core with given strength *m* and anglular constant $c = \pi/2$.......................... 121

3.3.4. Effects of geometric nonlinearities on solution accuracy.............................. 122

3.3.5. Instability-induced shape change of LCP sheet with hedgehog disclination defect 123

3.3.6. Profile of I_{eff}^{crit} for various α, ζ, and β normalized by their original values... 123

LIST OF TABLES

Table Page

2.2.1. Simulation parameters for nematic deformation 85

2.2.2. Simulation parameters for nematic deformation 85

2.3.1. Molecular dynamics (MD)-based microstate parameters 86

2.3.2. Constitutive parameters for Landau-formulation for smectic-nematic-isotropic phase transition 87

2.6.1. A mixing ratio of TN-LCP compound... 87

2.6.2. Principal bending axis ψ for each face and LPL 88

3.2.1. Pseudocode of the present work. Hat indices indicate functions 124

3.2.2. Center position of strain pattern in S = 0.5 126

3.2.3. Gaussian-distribution fitting result for $S = 0.8$ 126

3.3.1. I_{eff}^{crit} fit parameters.. 126

Chapter 1. Introduction

1.1. Liquid crystal polymer (LCP)

A liquid crystal polymer (LCP) broadly refers the polymeric system composed of long, flexible chains and short, rigid, rod-like liquid crystal mesogenic units, by which a crystallinity states are "memorized" into the polymeric systems as liquid crystal molecules impose crystalline order to the molecular chains via crosslinking, as first postulated by de Gennes at al. [1,2]. This material has been categorized as "smart materials" that responds to environmental changes (e.g., changes in heat for shape memory alloys), and thereby has been envisaged to yield interesting phenomena, for example, increased (or decreased) polymer anisotropy in order to accommodate the increased (or decreased) orientational order of the mesogens [1]. For nematic polymers whose liquid crystalline order possesses only a rotational symmetry, for instance, experimental studies have revealed that the material shrinks/expands up to few hundred percent upon heating/cooling, which renders the material an attractive candidate for artificial muscles [3-4]. Therefore, understanding the liquid crystal phases and corresponding polymeric conformations (i.e., the geometries of representative polymeric backbone structures) is essential to comprehend the self-deforming nature of such materials.

Recently, the diverse stimuli-responsive actuations are reported, of which actuation sources vary greatly depending on the type of the liquid crystal. When photochromic agents (e.g., azobenzene and azotolane) are embedded into an LCN, their reversible isomerization, which is induced by light, perturbs the original symmetry of the microstate and thereby affects the behavior of the overall structure. Due to the benefits of optical stimuli, such as their abilities to be transmitted over long ranges and to be controlled precisely, the characteristics of photo-responsive LCNs have been widely studied both numerically [5-9] and experimentally [10,11], and it has been found that the photomechanics, for instance, change significantly if the material properties (e.g., backbone connectivity and crosslinking density) are modified. Various photo-responsive micro-scale systems have also been realized; these systems range from homogeneous strips that produce primitive deformations (i.e., bending and twisting) to composite robotics that actuate rapidly [12-18]. In overall, it is quite imperative to clarify the relations between diverse agents involved within the phenomena: stimuli-responsive liquid crystal, microstates polymeric chain, and macroscopic structure subject to internal loadings.

1.1.1. A self-organizing characteristic of LC

A self-organizing phenomena is one branch of the complex physics studies, which entices many researchers as it reveals the nature's aesthetic, representative, and practicable characters. The understanding of the configuration of a mass exhibited by its components (e.g. birds in the flock, individual molecules in the compound) is of interest in the study. Liquid crystals, which form a distinguished patterns due to the anisotropic interactions between individual molecules, are therefore representative self-organizing materials. As implied by the terminology of itself, LC refers an intermediate state between a solidified crystal, whose molecular arrangement is fixed, and a liquid, whose individual molecule retains fluidity respect to each other. It is therefore often referred as a 4th state matter, as it flows like a liquid, while it maintains symmetrical order depending on the inherent geometric characters of the constituting molecules. Such behavior is analogous to the characteristic 1-D stacking of TMV (tobacco mosaic virus), whose molecular shape is high-aspect ratio cylinder. Due to its intermediate nature, LC phase also has two distinctive characteristics as their self-organizing characteristics are not fixated.

First of all, the directionality can be alternated within the domain of interest. When the LC molecules are not treated to be aligned by force, for example, the inhomogeneous distributions of the local alignment (i.e. Schlierene texture) is observed as the hot, untreated liquid LC molecules naturally condense into polydomain structures composed of multiple uniaxial domains with different directionalities [1,19]. In such case, a continuity of director is often violated at some points, termed by disclination defect. Inversely, the aligned texture of LC is possibly distorted in order to accommodate the change of the environment. One of the pronounced effect is found in Freederickz transition [1,2], where the directors of molecules change as a response to the strong electric, or magnetic field as the external field imposes the rotational moments to the weakly polarized LC. The alternation of the directors within the domain is often interpreted in terms of the elasticity of the LC, which indicates a competition between the externally applied energy and energy penalty of the directional distortion. Note that such means of alternating alignment leads to one of the contemporary marvel in these era: a liquid crystal display (LCD).

On the other hand, the phase of LC can also be alternated. Following classical Ehrenfest classification, the ensemble-averaged order of the molecules dramatically changes whenever phase transition occurs. For example, the symmetric order of the thermotropic molecules are totally disturbed and thus the system becomes isotropic when temperature increases up to threshold order-clearing temperature. Figure 1.1.1 illustrates a phase change constituted of crystal (K), smectic (Sm), nematic (N) and isotropic (I), which emerges as ambient temperature increases [20]. Obviously, the smectic phase exhibits both translational and orientational symmetry, which are sequentially removed as temperature increases.

It is worth to remark that these two possibilities of the geometric change of LC structures, are similarly transcribed onto the LCP structure, thereby changes the phase-driven behaviors. Moreover, as these geometric changes are also a function of the internal molecular characteristics, such as the elongated Kuhn segment of the chromophore, and the functional part of the rigid molecules, the studies of the stimuli-responsive behaviors of LCP requires information that ranges from LCP's molecular constituents to their phase distortions.

1.1.2. LC-driven properties of LCP

As remarked, the characteristic behaviors of LCP are largely derived from its combination of LC molecules and polymeric chains. Although physical properties of

LC are maintained in general, chemical crosslinking distinguishes the LCP from its uncrosslinked counterpart as well. First of all, the transition of the mechanical property occurs during the polymerization; unlike LC, whose molecules are contained within the glass cell, consolidated LCP is a self-standing material that deforms by external loadings, let alone shearing. In addition, the LC phases and its alignments upon polymerization are fixated to the polymer, by which the polymer exhibit not only anisotropy but also preserved optical traits. Interestingly, such fixation produces the optical-mechanical coupling because the deformation of the LCP yields the relative displacement of the crosslinked point, which produces reorientation of the mesogenic constituents.

The LC phase transition, on the other hand, can also influence the structural behavior. For instance, aforementioned temperature-dependent behavior of thermotropic LC, of which phase undergoes transition as a response to the thermal stimuli, can be transferred to the LCP through crosslinking, in a way that optical properties are onto the structure. The first successful realization of macroscopic order-mechanical coupling is done by Finkelmann and his colleagues [12], who synthesized uniaxially aligned (i.e. nematic) liquid crystal elastomer. The elastomer sheet is proven to exhibit up to few hundreds % of reversible successive shrinkage and elongation, as an interplay between initial stretch that induces and fixes the alignment of the rigid molecules and the phase transition between nematic and isotropic states, whose chain configurations are uniaxial ellipse and direction-invariant sphere, respectively. Due to the reversibility of the transitions between LC phases, the transition-induced mechanical behaviors is hysteresis-free, likewise. The LCP-based applications, therefore, can be treated as the mechanical element that reacts to given stimuli, rather than the structure. Throughout this dissertation, the term order-mechanical coupling is used to refer such coupled, interdisciplinary behavior since the phase of LC is frequently parameterized by order to the symmetry.

Some recent studies have further explored the possibility of the photo-actuator, which is a light-driven variant of the coupled behavior Provided that incorporated mesogens exhibit photochromism, such as azobenzene chromophore that reversely changes its form to cis- (boat shape) out of an initially trans- (chair shape) state upon exposure to photons with adequate frequency, the polymeric conformation similarly changes with light. Given that actinic light is bombarded onto the surface of photo-responsive LCP, the energy of the photon is continuously absorbed into the matrix while it travels through the materials and isomerizes the photochromic molecules. An increased number of kinked molecules reduce the phase transition temperatures as these molecules lose their rigidity and cannot contribute to the order, thereby renders the state of the liquid crystal inhomogeneous in the depth-wise direction. As a result, differential photo-induced strain is generated in out-of-plane directions that simultaneously bends and elongates the specimen. Moreover, reversibility of such mechanism has been proven to generate no plastic deformation, thereby rendering the photo-bending mechanism an attractive means for the remotely controlled smart actuation [15,16,21-24], of which the behaviors are possibly alternated whenever we change the backbone, domain, and even the type of liquid crystallinity.

1.1.3. Synthesis: from LC alignment to Polymer Crosslinking

A synthesis of LCP is briefly described in the present chapter, as a preparation of the material and its characterization are crucial in order to understand the behaviors of the material, and the possibility of its manipulation on design, by which its mechanical behaviors are modified. For instance, a homogeneous directionality of the liquid crystalline alignment is possibly distorted into diverse configurations, given that mechanical/electrical loading is given during the synthesis.

The synthesis procedure is composed of the multiple steps as a liquid mixture of the compound turns into solid, a self-standing structure. In general, there are several types of LCP present to this day, distinguished by a density of the crosslinking: gel, elastomer, and densely crosslinked polymer. Although their mechanical properties (e.g. modulus) are greatly differ from one to another, their phase behaviors that bridges a light-induced dilution to mechanical shape changes are same in general; hence, the present description does not cover all the procedures applied for every types of LCP, and it is worth to remark that the densely crosslinked polymer is preferred and used throughout this study as such choice eases computational problem such as a nonconvex (i.e. micropolar) behavior present in the low-crosslinking cases. In this respect, the reader may find a simplified description about a synthesis of heavily-crosslinked LCP, in which each step is remarked along with possible modifications and their prospective effect to the phase behavior.

A synthesis step, of course, starts with the material selection, which is composed of diverse mesogenic compounds, including light-responsive ones. This step is crucial as it largely determines the mechanical behavior; a length of hydrocarbon found within the mesogen, for instance, determines flexibility and strength of the LCP. A Fig. 1.1.2 illustrates an example of chemical formulas of molecular compounds found in the literatures [13,15,26-28].

Note that rigid part, often referred as a Kuhn segment, is always present in the liquid crystal molecules, while an azodye (-N=N-) exists only in photo-reactive chromophore (see Fig. 1.1.2. (a) and (b)). The properties associated with the light absorption are determined by location and number of azodye, as demonstrated by green-light driven photo-actuator incorporating azotolane [29]. Aside of this molecule, auxiliary components such as Ingacure, a photocrosslinker, and chiral-dopant is also shown. It is worth noting that a chiral-dopant is only used to induce a twisted nematic (TN) configuration within the cell; without the dopant, the random chirality is imposed onto the structure, hence a consistent spin direction is not observed. The homogeneous mixture is then prepared through a heating and stirring.

Another important step is a glass cell fabrication, which determines a directionality of the LCP structure. Note that this process is analogous to the preparation of uncrosslinked liquid crystal cell as the alignment is similarly determined by the microgroove structure formed on the glass cell: the arrays of the groove align the mesogenic direction, in a way that the longitudinal axes of the ellipsoidal molecules are anchored by parallel to the groove direction. On the other hand, such properties are not exploited in elastomer-based LCP synthesis [2,4,10,12], of which mesogenic directionality is imposed by a mechanical loading between two steps of crosslink. Following a customary step of LC, the microgrooves are created by a rubbing process taken place after the glass cell is firmly coated. The microgrooves are generated in parallel to the rubbing direction. Therefore the attachment of the glass cell determines the surface configuration of the liquid crystal molecules; the nematic LCP is generated when two identical glass cells are attached, while twisted nematic LCP is made in case of these glass cells are attached perpendicularly. It is worth noting that the recent reports on LCP deformation often exhibits diverse alignment technique other than rubbing-based ones; a photo-alignment or a doping techniques, for example, possibly create quite exotic textures on the LCP surface that possibly induces inhomogeneous strain fields [30-33].

Lastly, a micro-spaced glass cell is prepared wherein melted LC mixture is poured into, driven by capillary forces. A UV-crosslinking is then taken place that generates a LCP. A thermal crosslinking is also possible, given that temperature range of dissociation of thermal crosslinker must agree with the nematic range of the liquid crystal. The mesogenic configuration of LCP's stress-free state (e.g. smectic solid) is determined during this process, as the LC state are fixated during the polymerization.

1.2. Theoretic Background

As described in chapter 1.1., LCP has been vigorously investigated in the attractive envisions of a novel material with anomalous phase-behaviors, which originated from the combination of polymeric elasticity and self-organizing traits of the LCs. Predominantly, such coupled behavior has three distinguished traits. (1) The actuation source may vary depending on the constituting chromophores' sensitivity to the certain stimuli (e.g. temperature if they are thermotropic LCs). (2) The actuation is basically integrated within the structure itself, by which some hurdles for the future actuation system can be circumvented. (3) Various exotic deformations are possibly generated out of seemingly equivalent models; when liquid crystalline textures are tuned either via rubbing, photo-alignment, or doping functionalized inhomogeneity [1-3, 34-37], they show unevenly distributed principal directions of local deformation.

To understand the light-driven actuation of LCP, the physics that broadly accounts a photochromic behavior of azodye, phase change of LC, and polymeric structure change is pivotal: a photomechanics. It is a combination of distinctive physics that ranges from photo-isomerization, phase behavior, to structural mechanics. In this section, the theoretical backgrounds of these fields of study and their overlapping area are described.

After describing the convoluted behavior of LCP and its possible deforming modes, a thermotropic phase transition and is concomitant mesoscopic change is described in terms of phase behaviors. For LCP material, phase behavior generally indicates the shape change of the material upon configuration change of the molecules, which requires the modeling of the interplay between polymer chains and geometric configuration inherited by liquid crystalline molecular status. The Landau model of the LC molecules is described as well as its effect to the molecular conformation. Secondly, I present an inherent multiscale nature of photomechanics, which is associated with constructing comprehensive finite element model of LCP. The bridging of the micro and macro scale, reflected onto the formulation of the LCP structure, is also discussed in brief.

1.2.1. Thermo-opto-mechanical coupling

The order-mechanical coupling has many variants; the LCP becomes responsive to the light irradiation, provided that incorporated LC molecules are reactive to the light. The chromophore that includes azodye, is a notable example to such light-sensitive molecules. E-Z isomerization of the molecule, where the geometric shape change is induced while its chemical stoichiometry of the structure is conserved, is the example of reversible light-induced isomerization shown in the azobenzene chromophore [2].

The irradiation of different wavelength of light determines the shape between chair-shaped (trans-) and boat-shaped (cis-) molecules, which are geometric isomers with different light transmittance. When the ultraviolet (UV) light is given, for example, trans- molecules, a low-energy state, absorbs the photons and becomes cis-molecules, a high-energy state. An initially ordered configuration is hence perturbed due to the shape change of the rod: from uniaxial ellipsoid to kinked rod. Such influence is described by reduction of the order parameter, which is an indicator of phase transition. The LCP system with more kinked molecule therefore becomes more susceptible to the given thermal energy and threshold order-clearing temperature decreases as a function of the number of generated cis- molecules. Subsequently, the induced phase transition results in microscopic shape change, which is often referred to a phase behavior, as the shape of a polymeric chain entanglements changes with regards to the organization of LC molecules. In short, the thermo-opto-mechanical coupling to the mechanical behavior arises when two conditions are met: (1) LC molecules are reactive monomers (i.e. polymerizable functional group attached to the rigid part), (2) the rigid part of the chromophore is sensitive to the light irradiation.

In terms of macroscopic deformation of the LCP structure, the interesting mechanical phenomena are found based on the multiphysical coupling. The light-induced bending is the representative example, in which 2D thin strip changes their shape into 3D structure when the light is irradiated. Such out-of-plane deformation is a novel characteristic when compared to classical shape-memory active material such as shape memory polymer (SMP) or shape memory alloy (SMA), whose deformation mode remains in-plane elongation/shrinkage. A gradient of light-induced strain, generated by decay of the light while it penetrates through the medium, is behind the deflection.

The remote and precise controllability is another advantage of photo-responsive behavior, thanks to the advanced optical technologies. Compared with the slow and long-range diffusion of a phonon from thermal stimuli, a photon bombarded from the laser source can be concentrated as demonstrated well in semiconducting industries. The need of contact heat source, of electric wirings accompanying traditional active material is therefore not required in this novel material.

1.2.2. Liquid crystalline phase behavior and the microstate change

In terms of energy principle, a phase transition from one state to another involves a non-convex energy functional which has multiple wells with local convex profiles. In nematic LC, for instance, there are two wells that accounts for uniaxial nematic order and isotropic random distribution.

Throughout present dissertation, a Landau model of LC phase transition is adopted [1]. The model is constituted of polynomial expansions with order parameters and constants, which are temperature-varying properties when molecules are thermotropic. Equation (1.2.1) shows a typical Landau model of nematic-isotropic transition, where the tensorial nematic order parameter **Q** is penalized by its 2nd, 3rd, and 4th power terms with parameter A,B,C.

$$f[\mathbf{Q},T]=\frac{1}{2}Atr\left(\mathbf{Q}^2\right)+\frac{1}{3}Btr\left(\mathbf{Q}^3\right)+\frac{1}{4}Ctr\left(\mathbf{Q}^2\right)^2 \tag{1.2.1}$$

The minimizer of the energy functional shown in Eq. (1) is dependent to the constituting constant A, B, and C, where only A is a temperature-dependent constant in typical analysis. By setting $A=A_0\left(T-T_c\right)$, where T_c is a critical temperature similar, but not equal to, nematic-isotropic clearing temperature T_{NI}. The 1st order phase transition is hence well-reproduced, as often shown in short rigid molecules such as 5CB. Although the Landau model is often criticized as it overestimates the order parameters in low-temperature regime, it is acceptable in photomechanical analysis in general as the regime of interest involves the phase behavior that occurs around phase transition temperature.

Note that many variants of Landau model are possible, that is, by increasing the order of the polynomial or including more internal order parameters (e.g. translational order parameters in smectic-A LC). The comprehensive review [38] on the Landau model demonstrates that fine tuning of the constitutive parameters is associated with the nature of the LC molecules such as Kuhn length, sensitivity to temperature, and even geometric shape of the molecules.

1.2.2.1. Order parameter description of uniaxial phases

There are many types of LC, as a molecular geometry and an interaction energy involve the stable configuration (i.e. shape) and phase-change characteristic (i.e. temperature). In this thesis, the LC phases that retain uniaxial geometry are considered. A nematic LC stands for the molecules with orientational symmetry only, as indicated by term “nema” derived from “thread” in Greek. It is the simplest phase when we decrease the temperature from isotropic, and the molecular configuration is mostly ellipsoidal shape. A scalar orientational order S is widely used to parameterize the degree of alignment of the chromophores with respect to their averaged direction (i.e. director), computed through ensemble average of the angle deviation. Provided that biaxiality is not provoked, the tensorial format of orientational order $\underset{\sim}{Q} = diag\left(-s/2, -s/2, s\right)$ is also frequently used.

The smectic LC, on the other hand, the translational symmetries, which require a periodic function that accounts for the spacing between each layer and the layer normal, are commonly described by the complex scalar order parameter: $\psi = \rho_o \exp\left(i\vec{q}_o \cdot \vec{n}\right)$. An order parameter ψ is defined by an amplitude of density modulation ρ_o, and a real density wave phase $\vec{q}_o$, of which the gradient indicates the layer normal.

1.2.2.2. Phase behavior: a crosslinking-medicated conformation

Upon phase transition, the symmetries of LC alternates greatly; such geometric shift induces the change of statistical distribution of the crosslinked point, which determines the conformation of the polymer. Such microscopic changes are largely investigated by prominent Verwey-Terentjev-Warner elasticity (see Eq. 1.2.2), a statistical model of the ensemble-averaged polymeric chain distribution with respect to the directionality of the LC molecules.

$$f = \mu\left[tr\left(\mathbf{L}^{-1}\boldsymbol{\lambda}\mathbf{L}_0\boldsymbol{\lambda}^T\right) + \log\left(\det\mathbf{L} / \det\mathbf{L}_0\right)\right] \qquad (1.2.2)$$

Where the $\mathbf{L}_0$ and $\mathbf{L}$ indicate deformed, and initial shape tensors of the polymeric conformation. The deformation gradients of the LCP are also presented with $\boldsymbol{\lambda}$ and $\boldsymbol{\lambda_o}$. For nematic polymer, where the microstates are approximated by a uniaxially elongated ellipsoid. Note that if the shape tensors become a tensor identity, the VTW model is degenerated to the classical neo-Hookean energy, which is a primitive form that describes the hyperelastic behaviors. The phase change from nematic to isotropic case, for instance, the initially anisotropic polymeric conformation (i.e. anisotropy radii of gyration tensor) becomes isotropic; hence, the polymer chains shrink in the principal direction of the gyration tensor that reduces the principal eigenvalue of **L**.

The modeling of **L** with respect to the external stimuli and molecular change is significant in terms of the interdisciplinary coupling; in some cases, the overall procedures are captured by the critical exponent based modeling , where nematic-isotropic transition temperature (T_{NI}), which differentiates two distinct phases, along with the scalar shape parameter r, which represents the polymeric conformations [2, 6,8,939] are utilized as internal parameters.

1.2.3. Multiscale / Multiphysics coupled nature

Concerning deconvoluted photomechanics, the existing theoretical approaches have been successful in describing each photomechanical behavior from the perspective of different physical regimes of interest. For example, a polymeric description of such micropolar materials based on continuum mechanics has succeeded in reproducing certain details concerning the anomalous behavior of nematic solids: e.g. the non-convexity of the energy landscape, the dynamics of stress evolution and diverse stress-accommodating shape change (such as bent elastica), etc. At the other side of the analysis, small-scale simulations have demonstrated that thermomechanical phase phenomena are related to the light-induced effects, and that they correlate well with the observed light-induced motions. Although a few recent studies have suggested connections between changes in nematic order and large-scale behavior, these works still resort to classical modeling by relying on Landau-de Gennes coupling along with the linear dilute model. Accordingly, such approaches fail to take into account crucial molecular details regarding light irradiation.

From this point of view, it is salient that there is a dire need to reducing the knowledge gap between the two levels (micro and macro) in order to simulate the large-scale photo-responsiveness in terms of cis-trans isomerization. More specifically, there are three mechanisms to be taken into account. Firstly, the physics of the light-sensitive molecules, which is referred as a photochromism, must be taken account to quantitatively investigate light-related parameters such as intensity, settle time for irradiation. The mesoscopic polymeric conformation also needs to be considered, to bridge between the number of stimulated molecule and the microscopic state change. In this step, the polymeric description not only in terms of isotropic, random-walk but non-overlapping flexible chains but the relative movement of the crosslinking points should be analyzed with respect to perturbed variables. As this is a molecular level of change, the microscopic characterization is underwent through molecular dynamics simulation (MD), of which atomic structures are penalized by spring constants. Lastly, the analysis of the deflection of the structure requires continuum mechanics, as internally generated stress by light irradiation must comply with governing equations and constitutive model. It is worth to remark that even though these three regimes of study are well-established with the advances of computational mechanics, their interplay are still in question; for instance, whether light-induced kinked molecule (cis-) influences the structural properties, that is, nonexisting phenomenon in liquid crystal physics.

In this dissertation, we examine the azobenzene-based acrylate side-chain LCPs, the backbones of which are composed of acrylate monomers and crosslinkers. Such glassy networks exhibit various light-induced bending behaviors, which result from the modulation of certain physical properties (e.g. Kuhn length, crosslinking density). Their in-plane shrinkage is overshadowed by out-of-plane deflection or bending, because the trans-to-cis isomerization processes are likely to induce in-plane mechanical strain caused by the high modulus of the structure.

1.3. Motivations

In recent years, there has been a surge of experimental reports focusing on the versatility of the LCP based photo-responsive systems as a building block to the mechanism.

Figure 1.3.1 exemplifies the diverse photo-responsive behaviors which ranges from uniaxial elongation to complex deformations; firstly it shows demonstrations of elementary motions generated by light: it can walk, swim, and rotates just as classical actuator does, while scaled-up to mechanisms demonstrates a precise and remote-controlled micro robotics and fast actuating system. These various deforming modes are obvious advantages of the LCP-based photoactuation, where structure and actuating material are integrated.

The improvement of the behavior of the materials is also a branch of recent investigations. The increase of the mechanical stiffness and modulus, and the shift of the operating wavelength of light [40-44] are the examples of this investigations, which narrows the gap between real operating condition with laboratory environment. Note that actuation source is possibly controlled, depending on desired deforming mode; increasing ambient temperature leads homogeneous uniaxial length change, and varying wavelength of light determines the mode of bending. Microstate of the material is possibly controlled as well; the directionality of the LC molecules incorporated within the material not only inherits the anisotropy of the LCP-based system, in a way that fiber does to laminated composites, but also determines the principal directions of induced photo-strain. Such convolution of different mechanism of actuation characterizes the photomechanics, which leads to the possibility of multiscale view of the material design.

Nevertheless, there is less interest in the field of mechanical design and its multiscale framework. In 2015, White and Broer remarked that "*One significant challenge is the extension of the basic understanding of the chemistry and physics of these materials, and their responses to stimuli, to what and how these can enable* *distinctive performance when in the hands of a mechanical designer*" in the prospecting the programmability of LCP [45]. Following the same view, the design framework is proposed in the present dissertation. Inspired by mechanical design protocol in computer-aided-engineering (CAE), the schematic design protocol that seamlessly incorporates the analysis and design are proposed. It is worth to remark that novel multi-scale computational analysis technique is employed in both analysis and design order to account the interdisciplinary nature of the photomechanics dealt in the chapter 1.3. In this regards, a finite-element-based multiscale approach with the following constraints are proposed herein: 1) apropos of the discussion of LCN heating, microscopic observables must be included with regard to optical stimuli; 2) the method should be able to simulate large deformations, especially those related to bending, twisting, and geometric instability; 3) the method must provide the user with modeling capabilities in both micro- (e.g. backbone order Q_b-to-optical order Q relation, spatially distributed mesogen $\boldsymbol{n}$) and macro- (e.g. 3D domain shape, polarity of incident light) design parameters.

1.4. Organization of the present dissertation

The present dissertation is comprised of the two chapters, which sequentially describe the multiscale modeling, and the design of the photo-responsive actuations based on the proposed modeling framework. In chapter 2, the multiscale framework where several physical disciplines are convoluted, are proposed. The photo-induced isomerization, a subsequent change of the microstates, and the up-scaled mechanical phenomena are incorporated to the framework. First of all, the geometric nonlinearity considered within the finite element is discussed in terms of the kinematic decomposition of the deformed configuration. The constitutive equations of photomechanics, derived by incorporating light-induced changes into the variationally derived tensorial equations, are presented. In addition, an *in-silico* modeling of the molecular unit cell is presented for the microscopic characterization, which provides nontrivial phase behaviors inherent to the LCP modeling. To widen the simulation capability, smectic solid, a phase-variant of the nematic LCP, and the twisted nematic (TN) configurations are also discussed in terms of its characteristic bending phenomenon. Later sections of chapter 2 are devoted to the characterizing a fidelity of the proposed model; the nonlinearities of the light-induced deformation are discussed in terms of the geometric nonlinearity, and the nonlinear phase behaviors found by the molecular modeling of the crosslinked LC.

In chapter 3, a capability of the multiscale modeling is demonstrated as the modulation of the LCP actuation, which paves the way towards the design of the light-responsive systems. The design parameters are divided into extrinsic and intrinsic part, inspired by the LC directors are fixated during the crosslinking. First of all, parametric studies of the shape of the LCP solid and the uniform rotation of the director are conducted in order to reveal the effect of extrinsic (post-crosslinking) conditions to the structures; the uniaxiality of the director remains intact throughout the study. As the light intensity is somewhat proportional to the induced strain, the search of the optimal light irradiation pattern is also presented by take advantage of the numeric optimization. Lastly, the intrinsic design parameters are also investigated; the directionalities of the LC are significantly distorted. 2D textures with defects are examined, as they frequently emerges in the experiments [17]. The exotic deformed shapes are expected in this inhomogeneous distribution of the directors, as the light-induced strains are applied parallel to the director of the mesogens; hence the nonlinearity gets severe due to the mechanical frustration. It is worth to remark that such large shape change and the relaxed configuration under the external stimuli and mechanical frustration demonstrates the newly gained insight in terms of both physics and mechanical design. Although most of the results are presented parametrically in search of sensitivity analysis, some of them are compared with experimental results reported by either available literatures, or in-house experiments.

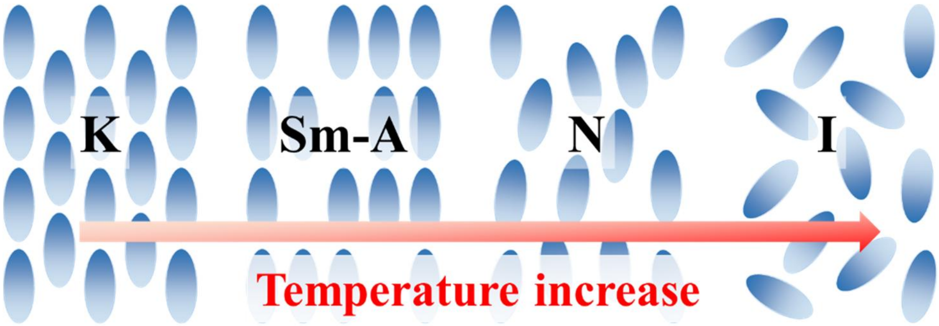
K
Sm-A
N
I
Temperature increase

FIG. 1.1.1. Illustration for the phase change of thermotropic liquid crystal (ellipse): a temperature-induced phase transition is comprised of crystal (K), smectic (Sm), nematic (N), and isotropic (I)

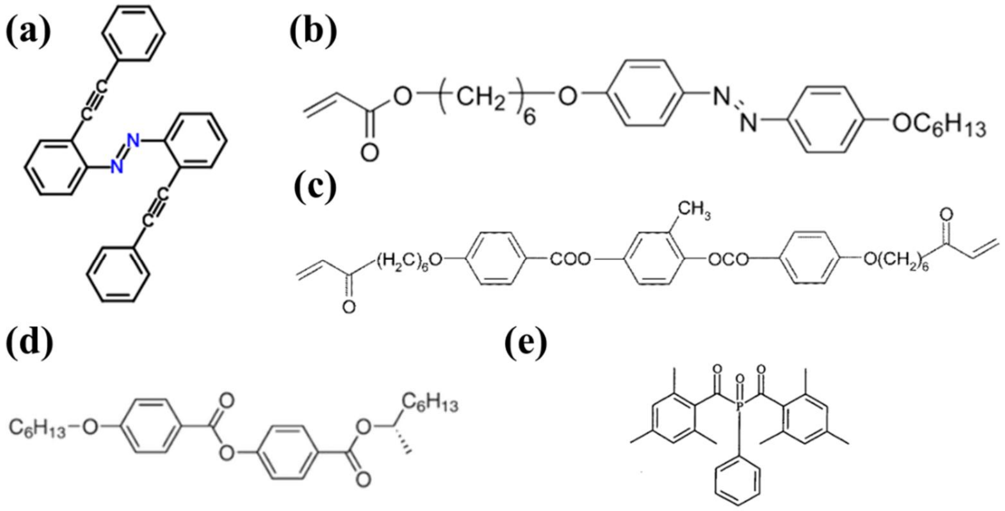
(a)
(b)
(c)
(d)
(e)
O
CH2
6
N
OC6H13
CH3
(H2C)6O
COO
OCO
O(CH2)6
C6H13
C6H13-O
P

FIG. 1.1.2. A chemical compounds that constitutes the LCP (a) azotolane (b) A6AB6, a light-responsive monoacrylate, (c) RM82, a reactive mesogen (d) S-811 chiral-dopant (e) Ingacure 819

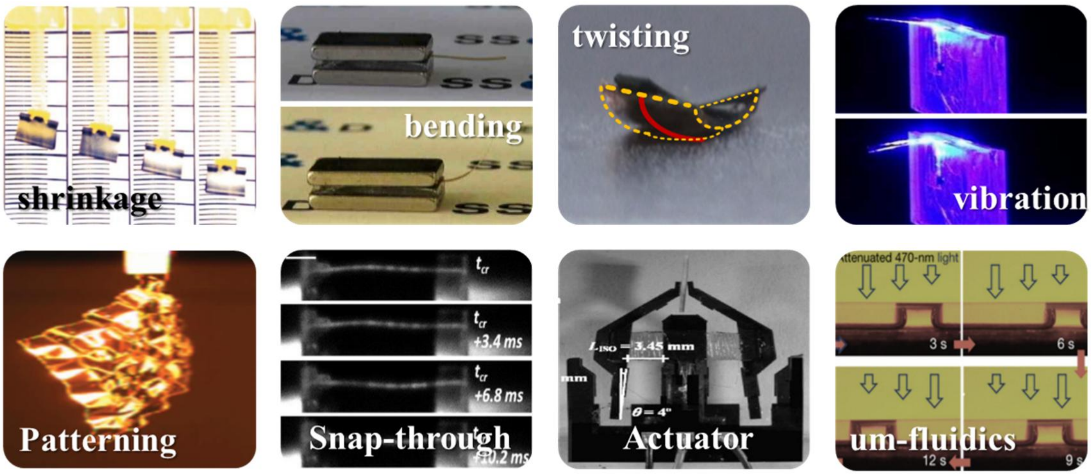
shrinkage
bending
twisting
vibration
Patterning
Snap-through
+3.4 ms
+6.8 ms
+10.2 ms
L_{ISO} = 3.45 mm
θ = 4°
Actuator
attenuated 470-nm light
3 s
6 s
12 s
9 s
um-fluidics

FIG. 1.3.1 The examples of light-responsive manipulation. The figures at the 2nd row are adapted from the references (D. Corbett and M. Warner *Liquid Crystals* (2009), M. Shankar et al. *Proceedings of the National Academy of Science* (2013), H. Jiang et al. *Nanoscale* (2013))

Chapter 2. Multiscale photomechanical analysis of LCP

In the present section, the computational framework of the photomechanics in the multiscale viewpoint is presented, distinguished by an incorporation of lower-scale information into the continuum-based description to the photo-responsive material. Such an interdisciplinary work is motivated by a strong interplay that envisions an inevitability of the interdisciplinary understandings, which is often neglected in the existing computational frameworks.

2.1. Overview of multiscale analysis of LCP

A sequential multiscale framework refers a type of simulation wherein information found at the microscopic level are reflected to the continuum level as a change of the internal variables at the constitutive equation, provided that length scales are clearly separated (i.e. each of the microscopic states is homogeneous, regardless of the macroscopic changes). In the present framework, I adopted such sequential schematics based on the following reasons: firstly, my focus lies on the bridging between optical stimuli to the macroscopic shape modulation, which requires no, or negligible amount of stress-induced phenomena because the phase behavior is basically stress-free. In short, the phase behavior dealt herein is basically molecular-scale property. Also, the sequential assumption is advantageous in the design of the material, an inverse problem, as the assumption does not require special treatment to the spurious physical properties such as reflecting waves that are frequently found in the concurrent multiscale schematics.

The success of the modeling is highly dependent to the selection of the up-scaling, or bridging parameter that exists both in a macro- and a micro- scaled physics, which in the same line of multiphysical understanding of the material. In the present work, a shape of the polymer for up-scaling parameter is employed, as the change of the shape is a basis of the phase behavior and change of stress-strain constitutive relation. The shape of the polymer is frequently approximated by a uniaxial ellipsoid elongated to the nematic director, whenever a rotational symmetry is found in the liquid crystal system. A shape parameter *r*, the square of the ratio between the backbone radius of gyration tensor calculated parallel $R_{\parallel}$ and perpendicular $R_{\perp}$ to the director, is introduced to represent the degree of anisotropy. On the other hand, a bridging between quantum to molecular level is also modeled by cis-populations (n_{cis}) of the given instance, which are determined by operation conditions such as light and temperature.

The information flow and computations involved are described in Fig. 2.1.1 and Table 2.1.1. The multiscale framework is adopted in order to upscale the microstate changes found in MD simulations; these are then used to simulate macro-scale deformation subjected to a specified molecular composition (here, the acrylate side-chain LCP), temperature *T*, and intensity of the light source I_o.

First, dn_{cis}/dt is determined as a function of I, the absorption coefficient η, and T with thermal relaxation ratio τ_c, as shown in Eq. (2.1.1) [10,12,36,46]. Unlike the temperature, which takes on a homogeneous value throughout the LCP strip, the light distribution is computed locally for each element according to the formula $I = I_o \cos^2(\phi)$, where the incident angle ϕ is the defined as the angle between each incident ray and the normal vector, which constantly changes owing to deformation. According to this formula, incident angles other than 90° decrease the absorbed number of photons [41]. I assume that the penetration depth *d* and profile of light are instantaneously equilibrated [48] (relative to the speed of the n_{cis} evolution). The implicit Euler method with a time-step of $dt = \tau^{\infty}/60$ is used for numerical time integration, in which t^{∞} indicates the approximate settling time computed by Eq. (2.1.2). A τ_c is computed in Eq. (2.1.3), assuming that the thermal-induced *trans-to-cis* isomerization follows Arrhenius-like behavior for given activation energy Δ.

$$\dot{n}_{cis} = \eta I\left(1 - n_{cis}\right) - \tau_c^{-1} n_{cis} \tag{2.1.1}$$

$$t^{\infty} = \exp(-\log(0.01)) / \left(\eta I + \tau_c^{-1}\right) \tag{2.1.2}$$

$$\tau_c = \tau_o \exp\left(\Delta / kT\right) \tag{2.1.3}$$

$$I_{eff} = W_L\left[I_{eff}^o \exp\left(I_e^o - z/d\right)\right] \tag{2.1.4}$$

The last equation (Eq. (2.1.4)) describes the profile of light intensity based on the Lambert W function (W_L), which lacks a closed-form solution. The light intensity decays non-exponentially as the light travels through the polymeric domain, and its decay profile is affected by the maximal intensity of incident light I_{eff}^o on the surface of the film, the out-of-plane position from midplane *z*, and the penetration depth *d*. *d* characterizes the saturation depth of light, possibly determined by the interplay between polymer characteristics and the crosslinking ratio of the chain. It approximates the nonlinear optical absorption and concomitant nonlinear light penetration; a photo-bleaching effect [4, 49-51] that changes both the temporal and spatial distributions of *cis*- concentration is thereby considered.

Given that a light intensity and n_{cis} is specified at the thickness integration point, a shape parameter *r* (which is equal to λ^3) [5,6] is computed by point-wise to describe the microstate, as shown in Fig. 2.1.1(b). I assume that metric shape tensors of the polymer are degenerated to a single parameter *r*, as polymeric conformation remains uniaxial before and during photomechanical deformation [52]. That is because the MD simulation [53] results show that neither biaxiality nor compressibility is provoked during the spontaneous deformation of MD unit cells.

The correlation between a light irradiation and a shape parameter is also pivotal, but, unfortunately no closed formula has been proposed to elucidate the influence of the existing polymeric backbone to the liquid crystalline phase and the effect this has upon the increase of geometrically kinked (cis-) molecules. In this study, an experimentally determined format is used on account of its simplicity, and its 2nd-order phase transition behavior. According to the experimental results [39,54], the shape parameter *r* is:

$$r = \begin{Bmatrix} \left(1+\alpha\left(T_{NI}-T\right)^{\zeta}\right)^{3} & \text{for } T \leq T_{NI} \\ 1 & \text{otherwise} \end{Bmatrix}, \quad T_{NI}\left(I\right) = T_{NI}^{0} - \beta \cdot n_{cis}\left(I\right), \tag{2.1.5}$$

with α (optical-mechanical-order coupling) and ζ (effective critical exponent) representing material-specific parameters. A shift of T_{NI} resulting from light illumination is modeled as a linear dependence on the ratio of photoisomerized cis-molecules n_{cis} (with proportionality coefficient β), as shown. In classical point of view, β remains constant throughout actuation and depends only on the interaction between rigid molecules; the *cis*- molecules are thereby treated as an inhomogeneity that 'dilutes' the order. It is worth noting that other theories, such as those regarding linear proportionality to light intensity or heat [55-57], experimental fitting [7], and molecular theories [58], can possibly be applied as an alternative to this light-temperature-parameter coupling.

A macroscopic bending deformation for a given microstructural distribution is computed quasi-statically for given time step t, in which phase behavior is coupled to a geometric nonlinear shell in order to compute large-scale deformation. The incident angle ϕ for every element is computed consecutively for a given deformation and rotation, which in turn changes the light intensity and thus the n_{cis} distribution on the surface. The loop continues until t reaches $t^{\propto}$. The simulation parameters are summarized in Table 2.1.2.

The present upscaling scheme, which uses shape parameter *r* as a bridging value, is therefore understood as a sequential method that is suitable for obtaining a quasi-static solution, as well as distinguishing the timescales of separate physical domains. These assumptions, however, are often violated if the question is related to dynamics such as rapid vibration [14], wherein mechanical energy transfer is strongly coupled to microstate evolution.

It is also worth to remark that a steady-state cis-population density n_{cis}^{∞} is also employed whenever required, following Eq. (2.1.6). To simplify the relationship between n_{cis}^{∞} and a given light intensity *I*, an effective measure I_{eff} is introduced by multiplying the intensity by the cis state lifetime τ^{-1} and absorption rate Γ :

$$n_{cis}^{\infty} = \frac{\tau\Gamma I}{1+\Gamma\tau I} \hat{=} \frac{I_{eff}}{1+I_{eff}} \tag{2.1.6}$$

Although time-dependent solutions where computed n_{cis} parameter per each timestep is then discouraged and incident angles of the material that significantly alternate the behavior cannot be analyzed, the steady-state solution is still beneficial to analyze the deformation as it elucidates the effect from geometric nonlinearity, apart from the other effects Herein, steady-state solutions are therefore composed of n_{cis}^{∞}, computed directly from amount of incident light, and *r*, a derivative of n_{cis} and *T*.

Note that the present light-temperature-order model is a legacy from various fields such as polymer physics (the freely jointed model), phase transition theory, light decay, etc. The basic formula, therefore, offers much room for improvement because there are superior methods available for tailoring [25,59] and measuring [53,60] *r* directly.

2.2. Geometric nonlinear shell formulation

Behind the shape-change phenomena of the light-responsive LCP is an energy bombardment originated from light irradiation onto the surface of the material. Part of the photonic energy is absorbed by *trans*- molecules and used to photo-isomerization; the reduction of the density of photonic energy generates a gradient in the transverse direction, which in turn result in out-of-plane motion. A geometric nonlinearity is essential to analyze such finite-strain behavior, as the rigid-body motion is dominant mode in 3D deflection such as bending. In this work, therefore, corotational formulation by which strain is decomposed into linear part and rigid-body part, is employed herein.

2.2.1. Kinematics-based corotational formulation

It is worth noting that the kinematic separation of rigid-body motions and pure deformations from element displacements distinguishes element-independent corotational (EICR) formulation from other geometric nonlinear formulations that are based on polar decompositions of deformation gradients. Thus, EICR formulation has computational advantages, since the external filtration of rigid-body motion facilitates the calculation of higher-order terms without shear/membrane-locking phenomena and enhances the accuracy of solutions that are shape-independent. The conventional polar decomposition approach, on the other hand, may hinder both computational efficiency and programing procedure due to complex gradient of higher order elements. Aside from that, the EICR is also beneficial to stimulate future works in terms of mechanical design of actuators as an analytic sensitivity has been reported in terms of geometric nonlinearity.

To analyze the deformation of 2D LCP sheets into 3D deformed shapes through bending and twisting, geometric nonlinearity that arises from significant change of slender LCP geometry is considered in the present work.

Herein, the nonlinear formulation model is based on the co-rotational formulation approach. The most salient feature of the co-rotational formulation is the procedure for separating the pure deformation and the rigid body motion from the displacement of elements. In EICR [61], the separation is based purely on kinematics and thus distinguishable from basic polar decomposition of the deformation gradient; as an external filter, EICR considerations are applied externally to the local elements and thus strain-displacement relation is completely detached from nonlinear considerations (i.e. element independence). Therefore, I efficiently implement the higher order element, and thus enhances not only the accuracy of the solution but also reduces the need of reduced integration. Therefore, EICR is the essential tool for the geometric nonlinear solution under consideration. The matrix notation used herein follows that of Ref. [61].

To enable kinematic tracking of rigid body motions over the element, co-rotational formulation requires three configurations, as shown in Fig. 2.2.1. These are the non-deformed (Ω^{o}), deformed (Ω^{D}), and co-rotational (Ω^{R}) configurations. The latter is a theoretical concept introduced to mediate between two natural coordinates, based on the premise that the rigid body part of the total displacement is executed first, before the element is deformed.

The local frame $\mathbf{e}^{i}$ and the local-to-global translation matrix **T** are calculated element-wise during each time step. Located at the centroid of each element, the local axis of $\mathbf{e}_1$ is oriented parallel to side 1-2, whereas $\mathbf{e}_3$ remains perpendicular to the element. Ω^{R} and Ω^{D} are stated upon the same local frame, as shown in Fig. 2.2, because the local frame translates and rotates as its base element does. Pure deformation is obtained by comparing the deformed shape with the co-rotational one, expressed by the pure deformation $\bar{\mathbf{u}}_d$ and the rotation $\bar{\boldsymbol{\theta}}_d$, where an overbar and a subscript *d* each indicate that the properties refer to the local frame and pure deformation, respectively. A tensorial description for separating the rigid body motion from the global shape change is given below in Eq. (2.2.1):

$$\delta\bar{\mathbf{d}}_d = \begin{Bmatrix} \delta\bar{\mathbf{u}}_d \\ \delta\bar{\boldsymbol{\theta}}_d \end{Bmatrix} = \bar{\mathbf{H}}\bar{\mathbf{P}}\mathbf{T} \begin{Bmatrix} \delta\mathbf{u} \\ \delta\phi \end{Bmatrix} \equiv \boldsymbol{\Lambda} \begin{Bmatrix} \delta\mathbf{u} \\ \delta\phi \end{Bmatrix}, \tag{2.2.1}$$

where $\boldsymbol{\varphi}$ is a pseudo-vector of the node-wise rotator **R**, and **H, P,** and **T** are auxiliary matrices of EICR formulation. Equation (2.2.1) demonstrates the sequence of the kinematics-based procedures that define EICR. After the nodal displacement is transformed to the global frame via **T**, the deforming part is extracted through the projection matrix **P,** which extracts the pure deformation part. Matrix **H** eliminates the gap between the two pseudo-vectors $\boldsymbol{\theta}$ and ϕ.

The consistent tangent stiffness matrix **K** and the local residual force **R** are calculated, as shown in Eq. (2.2.2). A conventional Newton-Raphson algorithm is used to solve the FE equations. An adaptive step size control scheme [62] is used, and step size is either increased or decreased depending on the stiffness matrix conditions.

$$\begin{aligned}\Delta\mathbf{f} = \mathbf{f}^i - \mathbf{f}^e &= \mathbf{T}^T\overline{\mathbf{P}}^T\overline{\mathbf{H}}^T\overline{\mathbf{f}}^e - \mathbf{T}^T\overline{\mathbf{H}}^T\overline{\mathbf{f}}^{ph} \\ &= \mathbf{T}^T\overline{\mathbf{P}}^T\overline{\mathbf{H}}^T\left(\overline{\mathbf{K}}^e\overline{\mathbf{d}}_d\right) - \mathbf{T}^T\overline{\mathbf{H}}^T\overline{\mathbf{f}}^{ph}\end{aligned} \quad . \tag{2.2.2}$$

In Eq. (2.2.2), $\overline{\mathbf{f}}^e = \overline{\mathbf{K}}^e\overline{\mathbf{d}}_d$ is the local force and $\overline{\mathbf{f}}^{ph}$ is the photo-stress force. The projection matrix is removed for the light-induced force term because the rigid body part of the external load should not be subtracted out, as in the case of the following force:

$$\mathbf{K} = \mathbf{K}^i - \mathbf{K}^e = \left(\mathbf{K}^i_{GR} + \mathbf{K}^i_{GP} + \mathbf{K}^i_{GM} + \mathbf{K}^i_{M}\right) - \left(\mathbf{K}^e_{GR} + \mathbf{K}^e_{GM}\right), \tag{2.2.3}$$

with

$$\begin{aligned} \mathbf{K}_M &= \mathbf{T}^T\overline{\mathbf{P}}^T\overline{\mathbf{H}}^T\overline{\mathbf{K}}^e\overline{\mathbf{H}}\overline{\mathbf{P}}\mathbf{T} & \mathbf{K}_{GR} &= -\mathbf{T}^T\overline{\mathbf{F}}_{nm}\overline{\mathbf{G}}\mathbf{T} \\ \mathbf{K}_{GM} &= \mathbf{T}^T\overline{\mathbf{P}}^T\overline{\mathbf{L}}\overline{\mathbf{P}}\mathbf{T} & \mathbf{K}_{GP} &= -\mathbf{T}^T\overline{\mathbf{G}}^T\overline{\mathbf{F}}_n\overline{\mathbf{P}}\mathbf{T} \\ \mathbf{K}^e_{GM} &= \mathbf{T}^T\overline{\mathbf{L}}^e\overline{\mathbf{P}}\mathbf{T} & \mathbf{K}^e_{GR} &= -\mathbf{T}^T\overline{\mathbf{F}}^e_{nm}\overline{\mathbf{G}}\mathbf{T} \end{aligned} \tag{2.2.4}$$

As shown in Eq. (2.2.4), the stiffness matrices are categorized according to the source of nonlinearity; the subscripts *M*, *GR*, *GM*, and *GP* stand for the variations of matrices **f, T, H, and P** respectively. Terms with the superscript e denote illumination-induced geometric stiffness, and are calculated consistently with $\overline{\mathbf{f}}^{ph}$.

The finite element formulation of the linear element is constructed by using the variational principal; its derivation is given in Eq. (2.2.5):

$$\delta W = \int_V \delta u_i\sigma_{ij,j}dV = \int_V \nabla\left(\delta u_i\sigma_{ij}\right) - \delta u_{i,j}\sigma_{ij}dV = \int_S \delta u_i t_i dS - \int_V \delta u_{i,j}\sigma_{ij}dV \tag{2.2.5}$$

The first term on the right-hand side accounts for boundary conditions; thus our focus lies with the second term. As shown in Eq. (2.2.6), stress is divided into symmetric (strain-related: $\sigma^{\varepsilon}_{ij}$) and skew-symmetric (rotation-related: σ^{ω}_{ij}) parts:

$$\int_V \delta u_{i,j}\sigma_{ij}dV = \int_V \delta u_{i,j}\left(\sigma^{\varepsilon}_{ij} + \sigma^{\omega}_{ij}\right)dV = \int_V \delta\varepsilon_{ij}\sigma^{\varepsilon}_{ij}dV + \int \delta\omega_{ij}\sigma^{\omega}_{ij} . \tag{2.2.6}$$

with $\omega_{ij} = \left(u_{i,j} - u_{j,i}\right)/2$. Due to the skew-symmetry of element rotation tensor and corresponding rotation term, $\sigma^{\omega}_{ij} = -\sigma^{\omega}_{ij}$ strain-rotation coupling is removed from the equations. Therefore, the formulation for each shell element is:

$$\delta W = \int_{\Omega} \delta\left(\boldsymbol{\varepsilon}^{o} - z\boldsymbol{\kappa}\right)^{T} \left(\boldsymbol{\sigma}^{o} - \boldsymbol{\sigma}^{ph}\right) dV \equiv \delta\bar{\mathbf{d}}_{d} \cdot \bar{\mathbf{K}}^{e} \cdot \bar{\mathbf{d}}_{d} - \delta\bar{\mathbf{d}} \cdot \bar{\boldsymbol{\Sigma}}^{ph}, \qquad (2.2.7)$$

with

$$\bar{\boldsymbol{\Sigma}}^{ph} = \left\{\hat{\mathbf{N}}^{ph}, \hat{\mathbf{M}}^{ph}\right\}^{T} \qquad (2.2.8a)$$

$$\bar{\mathbf{K}}^{e} = \left[\bar{\mathbf{K}}^{m} + \bar{\mathbf{K}}^{b} + 2\bar{\mathbf{K}}^{mb}\right] - \left[\bar{\mathbf{K}}^{r}\right] \qquad (2.2.8b)$$

$$\begin{aligned} \bar{\mathbf{K}}^{m} &= \int \mathbf{B}^{\varepsilon T} \hat{\mathbf{A}} \mathbf{B}^{\varepsilon} dA, \quad \bar{\mathbf{K}}^{b} = \int \mathbf{B}^{\kappa T} \hat{\mathbf{D}} \mathbf{B}^{\kappa} dA \\ \bar{\mathbf{K}}^{mb} &= \int \mathbf{B}^{\varepsilon T} \hat{\mathbf{B}} \mathbf{B}^{\kappa} dA, \quad \bar{\mathbf{K}}^{r} = \int \mathbf{B}^{\phi} \hat{\mathbf{G}} \mathbf{B}^{\phi} dA \end{aligned} \qquad (2.2.8c)$$

The series of **B** matrices in Eq. (2.2.8) are strain-displacement matrices unique to the linear element formulation. The superscripts ε, κ, and ϕ are related to strain, curvature, and rotation, respectively. The optimal triangular (OPT) element suggested by Felippa [63] is used to compute the membrane part of the shell behavior, which is denoted by the superscript *m*. It is based on the assumed natural deviatoric strain formulation, especially optimized for in-plane bending and free from the aspect-ratio locking problem. The OPT elements are used to calculate the $\mathbf{B}$ matrices of the membrane strain and rotation (θ_z, u_x, u_y). On the other hand, discrete Kirchhoff triangular (DKT) elements by Batoz [64] are utilized to describe the bending behavior of the shell, which is the strain-curvature relation (θ_x, θ_y, u_z). The bending part of the motion is denoted by the superscript *b*, and it describes the curvature-related part of nodal rotation and displacement. From Kirchhoff-Love plate theory, it follows that the DKT elements are free from the shear-locking issue. The construction of 3D triangular elements with 18 degrees of freedom (DOF) is assumed to be a process of unification of two different sets of DOFs, as illustrated in Fig. 2.2.2. Throughout the computations, I assume that the angle between the local frame axis 1 and nematic orientation α is maintained, in analogy to the direction of the fiber embedded in the composite structure.

Constitutive matrices and eigenstresses are integrated through the LCP sheet thickness to generate a membrane, bending stiffness matrices, and in-plane resultants, all of which are marked with hat symbols. Simpson's numerical integration scheme is used because the properties are affected by the decay of light intensity described by the non-analytic, high-order Lambert W function. As illustrated in inset of Fig. 2.2.3, the profile of light varies from linear to exponential as light intensity and decay depth change. Figure 2.2.3 shows the effect of changing the number of integration points on the integrated values in the nematic solid cases, demonstrating that 150 points along the thickness dimension are sufficient for generating stabilized mid-plane properties in all cases. Although not illustrated in the present dissertation, the integration point of more than 240 is proven to be sufficient to yield non-dependency to a number of the points. However, the increase of the computational load is not significant since the material integration is only taken for each increment, which are at most 40 when we implement adaptive step length control [5].

2.3. Thermo-mechanical characterization

Constitutive relations of the material are explained in this section. A shape parameter, which interrelates with a micro- and macro-scaled phase behavior, is found within the tensorial description of the equation. These relations are presented separately in nematic and smectic cases, as the phase behaviors of these two polymers show significant differences. Furthermore, the numerical models about the smectic solids are less investigated when compared with nematic cases due to relative complex geometry of the smectic to the nematic.

In nematic solid, the constitutive equations are firstly discussed by briefly introducing the tensorial expression of quasi-soft coupled equation suggested by Y Lin et al. [8], which is the basis of the present constitutive relation. Polymeric conformations and directional anisotropy are parameterized according to the shape parameter *r*, from which stiffness change and photo-stress evolutions are determined. The molecular dynamics studies are also employed to reveal the microscopic changes driven by a light irradiation. Such molecular-scaled descriptions are compared to the available experiments, especially about the limit of the linear dilute model, by which proposes a significant behavioral difference between liquid crystals and its polymeric variant.

For smectic solids, on the other hand, a constitutive relations are formulated from scratch; the analysis model has not been proposed by recent literatures. The variational principles and a few physical assumptions are employed herein to deduce the relation, which leave rooms for improvement by the further experiments or *in-silico* investigations.

2.3.1. Nematic LCP

2.3.1.1. Constitutive relation of nematic-LCP

For nematic LCPs, photomechanical behavior refers to the spontaneous deformation induced by optical or thermal stimuli, and originates from strong connections between various areas of physical study: for example, polymeric backbone conformation, and the transition between liquid crystalline phases (nematic vs. isotropic). As demonstrated in the Verwey-Warner-Terentjev (VWT) model ($f = \mu\left[tr\left(\mathbf{L}^{-1}\boldsymbol{\lambda}\mathbf{L}_{\mathbf{o}}\boldsymbol{\lambda}^{T}\right) + \log\left(\det\mathbf{L} / \det\mathbf{L}_{\mathbf{o}}\right)\right]$), of which derivation is a consequence of statistical descriptions regarding entropic chains and their mesogenic constituents, the shape tensor $\mathbf{L}$ and deformation gradient $\boldsymbol{\lambda}$ exhibit strong coupling. Much of the experimental results about intrinsic phenomena of LCP, for example, soft-elasticity ($\mathbf{L}$ being changed by $\boldsymbol{\lambda}$) and spontaneous deformation ($\boldsymbol{\lambda}$ being changed by $\mathbf{L}$), [21,65,66] have been widely discussed with regards to the coupling.

Recently, a full tensorial description for the constitutive model has been devised by adopting the VWT model and complementing it with a Landau-de Gennes expansion, and by further considering the first and second laws of thermodynamics with additional kinematic constraints (see Ref. [P25] for a detailed derivation). It is worth to remark that an introduction of polymeric conformation tensor $\mathbf{g}$, which coincides with scaled shape tensor (i.e. $\mathbf{g} = \mathbf{L}/\det\mathbf{L}$) is crucial during the derivation, as it relates incompressible change between nematic to isotropic configuration, and provoke coaxiality while retaining physical features of polymeric conformation.

$$\boldsymbol{\sigma} = -p\mathbf{I} + \mu\mathbf{g}^{-1}\left(\boldsymbol{\lambda}\mathbf{g}_{\mathbf{o}}\boldsymbol{\lambda}^{\mathrm{T}}\right) = -p\mathbf{I} + \mu\mathbf{g}^{-1}\mathbf{B}_{m}\,. \tag{2.3.1}$$

As shown in Eq. (2.3.1), the Cauchy stress $\boldsymbol{\sigma}$ is presented as a function of the shear modulus μ, hydrostatic pressure p, effective left Cauchy-Green tensor $\mathbf{B}_m = \boldsymbol{\lambda}\mathbf{g}_o\boldsymbol{\lambda}^T$ and the current metric $\mathbf{g}$; coaxiality between the two parameters is found at equilibrium, and hence forms a basis of soft-elasticity, which explains the stress-free rotation of mesogenic average orientation upon perpendicular stretching.

A tensorial description is directly incorporated into the classical finite element formulation, once it is linearized via the assumption of infinitesimal strain. Although it discourages large stretching and accompanying stiffness change, the assumption is valid as long as spontaneous deformation with relatively small rotation and strain is considered. The linearized model is hence beneficial to simplifying the photomechanical behavior of LCPs and implementing to the finite element; in addition, linearized approach used in this study [8] prevent complex non-convexity that requires additional assumptions or solving techniques [9,67-69].

An observable shape parameter r, the square of the ratio between the backbone radius of gyration tensor calculated parallel ($R_\parallel$) and perpendicular ($R_\perp$) to $\mathbf{n}$, is introduced to represent the degree of anisotropy of the metric tensor:

$$\mathbf{g} = r^{-1/3}\mathbf{I} + \left(r^{2/3} - r^{-1/3}\right)\mathbf{n}\mathbf{n}\,,\quad r = \left(R_\parallel / R_\perp\right)^2. \tag{2.3.2}$$

As a result, the following linearized constitutive relation is thus derived as Eq. (2.3.3a); a detailed derivation can be found in Ref. [5,8]. Strong mechanical-order coupling is presented as reported by both theory and experiment [12]; that is, stress becomes a function of not only strain ε but also rotation ω and shape parameter r. Along with the constitutive equations, the infinitesimal effective strain $\boldsymbol{\varepsilon}_g$ and the director rotation $\delta\mathbf{n}$ are also presented. It is worthwhile to mention that director rotation is determined not only by strain but also by the rotation of the elements, and is perpendicular to the initial director $\mathbf{n}$. As depicted in Eq. (2.3.3b), biaxiality and inner coupling are exempted from the equation since they are not invoked by light-induced deformation that is parallel to the director [9]:

$$\boldsymbol{\sigma} = -p\mathbf{I} + 2\mu\left(\frac{r}{r_o}\right)^{1/3} \left\{ \begin{array}{l} \boldsymbol{\varepsilon} - \left[1 - \dfrac{r_o+1}{2(r_o-1)}\dfrac{r_o-r}{r}\right]\left[\mathbf{n}_o(\boldsymbol{\varepsilon}\cdot\mathbf{n}_o) + (\boldsymbol{\varepsilon}\cdot\mathbf{n}_o)\mathbf{n}_o\right] \\ + \dfrac{2r_o}{r}\dfrac{r-1}{r_o-1}(\mathbf{n}_o\cdot\boldsymbol{\varepsilon}\cdot\mathbf{n}_o)\mathbf{n}_o\mathbf{n}_o \\ + \dfrac{r_o-r}{2r}\left[\mathbf{n}_o\mathbf{n}_o + \mathbf{n}_o(\boldsymbol{\omega}\cdot\mathbf{n}_o) + (\boldsymbol{\omega}\cdot\mathbf{n}_o)\mathbf{n}_o\right] \end{array} \right\} \quad (2.3.3a)$$

$$\begin{gathered} \mathbf{B}_m\cdot\mathbf{n} = b_m\mathbf{n},\quad b_m = r_o^{2/3} + \mathbf{n}_o\cdot\left(\mathbf{H}\mathbf{g}_o + \mathbf{g}_o\mathbf{H}^T\right)\cdot\mathbf{n}_o = r_o^{2/3} + 2\mathbf{n}_o\cdot\boldsymbol{\varepsilon}_g\cdot\mathbf{n}_o \\ \delta\mathbf{n} = \frac{2r_o^{1/3}}{r_o-1}\left\{\boldsymbol{\varepsilon}_g\cdot\mathbf{n}_o - (\mathbf{n}_o\cdot\boldsymbol{\varepsilon}_g\cdot\mathbf{n}_o)\mathbf{n}_o\right\} \end{gathered} \quad (2.3.3b)$$

Equation (2.3.4) explains additional assumptions made to model the thin LCP sheets (reported in the experiments of Refs. [13,15,29,70]) whose length-to-thickness ratio was smaller than 1:20. The assumptions express (a) plane stress, (b) how the initially homogeneous directors remain homogeneous after the light-induced order change, and (c) incompressibility:

$$\sigma_{3i} = 0 \quad (2.3.4a)$$

$$n_3^o = n_3 = 0 \quad (2.3.4b)$$

$$\mathrm{tr}(\boldsymbol{\varepsilon}) = 0 \quad (2.3.4c)$$

The 2D constitutive equation is thus expressed by Eq. (2.3.5) for plane stress conditions (the Greek letter indices are 1 or 2), which can be readily implemented into a 3D shell model.

$$\begin{aligned} \sigma_{\alpha\beta} &= 2\mu\left(\frac{r}{r_o}\right)^{1/3}\left[\begin{array}{l} -\delta_{\alpha\beta}(\varepsilon_{11}+\varepsilon_{22}) + \varepsilon_{\alpha\beta} - \left\{1 - \dfrac{r_o+1}{2(r_o-1)}\dfrac{r_o-r}{r}\right\}\left\{\varepsilon_{\beta\gamma}n_\alpha^o n_\gamma^o + \varepsilon_{\alpha\gamma}n_\beta^o n_\gamma^o\right\} \\ + \left(\dfrac{2r_o}{r}\dfrac{r-1}{r_o-1}\right)\left(\varepsilon_{\eta\psi}n_\eta^o n_\psi^o\right)n_\alpha^o n_\beta^o + \dfrac{r_o-r}{2r}\left\{n_\alpha^o n_\beta^o + \omega_{\beta\gamma}n_\alpha^o n_\gamma^o + \omega_{\alpha\gamma}n_\beta^o n_\gamma^o\right\} \end{array}\right] \quad (2.3.5) \\ &\hat{=}\, \sigma_{\alpha\beta}^o\left(\varepsilon_{\alpha\beta},\omega_{\alpha\beta},n_\alpha^o;r,r_o\right) + \sigma_{\alpha\beta}^{ph}\left(n_\alpha^o;r,r_o\right) \end{aligned}$$

As shown, the effects of external stimuli must be expressed in relation to the shape parameter; most discernible changes from previous models [7,56] and the phenomenological continuum model [2] lay in the form of photo-induced stress $\sigma_{\alpha\beta}^{ph}$ as an eigenstress form, where arbitrary numerical values are not required.

2.3.1.2. In-silico simulation of light-induced microstate anomaly

The multiscale framework presented in this work, which consists of micro-scale simulations and a scale-bridging method, incorporates information on microstate evolution and macro-scale deformation. Below I present a detailed description of the framework, although I omit certain equations and simulation conditions that can be found in the references [5,53].

I model the molecular unit cell of the acrylate-based LCP, a polymeric structure with many mesogenic constituents, following the cell construction scheme suggested by Choi *et al.*[53], which incorporates energetic relaxation and multi-step crosslinking. The molar crosslinking ratio is set to 7:1[26], and energetic interactions and equilibrated polymeric conformations are computed via a photoactive potential [53,71,72]. The dihedral parameters of the azodye, as well as the potential coefficients of peripheral atoms, surrogate those of the conventional polymer consistent force field (PCFF). The simulations are performed with the program Large-scale Atomic/Molecular Massively Parallel Simulator (LAMMPS; heating-up simulations for photomechanical effect evaluation) and are complemented by Material Studios (crosslinking and cell synthesis) from Accelrys.

A unit cell of a partially isomerized LCP system with a temperature of 300 K is shown in Fig. 2.3.1, wherein dihedral angles of azodye molecules (-C-N=N-C-) indicate the transition between *trans-* (180°) and *cis-* (0°) states. The initial alignments of the chromophores are indicated by the director vector $\vec{n}$. I observed that azodye molecules reorient vibrantly upon isomerization and heating-up simulations, which possibly changes the molecular configuration and of their networks; this is reflected in the thermodynamic behavior of LCPs parameterized by an orientational order parameter (S) and a cell shrinkage parameter (λ), which vary with increasing temperature. The orientational order parameter characterizes the long-range symmetry of mesogenic alignment; it ranges from 0 (no directionality) to 1 (perfect alignment), and is computed as an ensemble-averaged parameter (see Eq. (2.3.6)) that is a function of the mesogen-director deviation angle θ.

$$S = \left\langle \frac{3\cos^2\theta - 1}{2} \right\rangle \tag{2.3.6}$$

The shrinkage parameter λ is defined as the fractional change in length from the beginning of the simulation (300 K) to the point at which the order-clearing temperature T_c is reached. Even though T_c is defined as the point at which S becomes zero, I neglect the data after S is reduced to 0.05; it highly fluctuates around 0 (i.e. the moving average of S settles to 0) as each mesogen is free to vibrate as the mesogenic symmetry is completely lost. Parametric fitting for the thermotropic phase transition parameters α, ζ is carried out in the temperature range of $0.8\,T_c - T_c$ in order to elucidate the phase behavior near this transition.

The accurate estimation of the order parameters and the shrinkage determines the overall results of this work. MD simulations are therefore executed many times by changing the initial setup, such as the position of the *cis-* isomers, the temperature ramping-up speed, etc. As these changes significantly burden the computational load, I store and reuse the results of the thermotropic parameters by fitting in a piecewise manner in order to consider locally varying the n_{cis} value distributed on the LCP structure. Although not shown here, changing the fitting scheme to a 3rd-order polynomial does not change the results, insofar as they continue to vary monotonically.

Figure 2.3.2 illustrates the MD simulation results of microscopic changes induced by light irradiation, as well as thermal stimuli. The mesogenic portions and orientations of each LCP unit cell are parameterized by the orientational order S and cell shrinkage parameter λ. S is the ensemble average of the orientation, whereas

λ indicates the fractional change in the unit cell's length L along the direction of initial alignment.

Above all, I observe a salient linearity between S and λ [39], which demonstrates a strong interaction between the optical order and backbone conformation. The relationship between these two parameters is summarized in Eq. (2.3.7), wherein a nematic order-polymeric backbone coupling parameter α describes the sensitivity of the polymeric structure to the perturbed rotational symmetry. The phase change of the mesogenic molecules is also of interest. In contrast to the behavior associated with the ideal Maier-Saupe phase transition model of liquid crystals [1], the LCP cell exhibits a roughly 2nd-order phase transition [39,54], as shown in Eq. (2.3.8). The orientational order-temperature ($S-T$) curves are parameterized by the order-clearing temperature T_c and the critical exponent ζ, as shown in Eq. (2.3.8).

$$\lambda = L / L_{iso} = 1 + \alpha S \tag{2.3.7}$$

$$S = \left|1 - T / T_c\right|^{\zeta} \tag{2.3.8}$$

Table 2.3.1 lists the MD-derived parameters with different populations of *cis*-molecules. In contrast to the classical dilute model, wherein all parameters but T_c remain constant with light irradiation, all the listed thermotropic parameters (i.e. T_c, ζ, α) vary monotonically upon the introduction of kinked molecules.

These trends clearly demonstrate two possible effects that may result from a change in the interactions between mesogens as the concentration of *cis*- molecules increases. Figure 2.3.2 (b) illustrates the change in the shape parameter r of a LCP as a function of the *cis*- population and the temperature. The shape parameter indicates the length ratio between the longitudinal and transverse directions of the polymeric shape in the nematic case; the fact that it decreases as the *cis*- population increases suggests that the anisotropy of the polymeric structure decreases. As assumed in the classical dilute model, wherein photoisomerization decreases the number of molecules involved in uniaxial order, the increased number of *cis*- isomers lowers the thermal barrier required to clear the uniaxial distribution of mesogens.

Additional effects that stem from the polymer conformation characteristics can also be found in the present acrylate-based model. For instance, crosslinked mesogenic molecules are densely packed, and thus their long-range interactions are easily perturbed by geometrical changes in the constituents. Newly introduced kinked molecules perturb the relaxed orientation of neighboring rigid molecules, causing them to deviate from their initial alignment. As a result, this loosens the stacking of the rigid mesogens (i.e. the distance between them is lengthened and their orientations deviate from one from another), and the strength of the interaction between rigid rods therefore decreases. This modification of long-range interactions not only reduces the orientational order, but also renders the polymeric structures less responsive to the decreasing order (lower α). As a result, their phase transition behavior becomes less abrupt near the clearing temperature (higher ζ). This represents a further deviation from the ideal 1st-order phase transition as the stacking effect becomes diminished. Additionally, comparing the thermotropic parameters (α, ζ) with those of elastomer-based LCPs [53] demonstrates the aforementioned differences that result from stacking characteristics.

This line of thought, however, is not a complete description of the observed phenomena. The retained thermomechanical phase behavior when n_{cis} = 1, for example, also contradicts the basis of the dilute model that expects fully photo-isomerized cells lose their long-range interactions. Such inconsistency in the classical viewpoint may be due to auxiliary effects that possibly stem from various and unaccounted origins, not to mention the aforementioned dense stacking effect. For instance, the change of the molecular architecture from side- to main-chain [3, 10, 36] that drives the change of the photomechanical properties exemplifies such an effect; the kinked dyes (i.e., *cis*-chromophore) contribute differently to the mesogenic order. Furthermore, the MD simulation results have shown that local voids and intrinsic stresses often evolve near the area where *trans-to-cis* isomerization occurs as the atomic positions are translated. These auxiliary effects and their influence on the phase behaviors are to be discussed in future work.

2.3.2. Smectic-A LCP

In the contrary to the nematic solid associated with a nematic-isotropic clearing temperature T_{NI} and a scalar orientational order parameter S, smectic solid requires more variables to consider due to the translational symmetry of the LC layers: a smectic-A-nematic transition temperature T_{NA} and a complex order parameter $\psi = \rho_o\left(i\vec{q}\cdot\vec{r}\right)$. Recent works have demonstrated that the addition of such symmetry yields unprecedented elasticity, as the layer undulation becomes another mode of soft, unstable mechanical responses: The opacity of the material changes when uniaxial loading exceeds the threshold value [12, 20, 73]. Concerning phase behaviors, the projection of the translational symmetry on the onset of nematic-to-smectic transition significantly influences the conformation of the polymer; it flattens the overall shape in the longitudinal direction and hence induces a pre-transitional effect [2, 42, 74]; thus, the phase behavior becomes non-monotonic. To date, works on the smectic solids and their characterizations are largely indebted to experimental studies such as small-angle X-ray scattering (SAXS) based observation, and supplemented only by a few physical and numerical simulation results. For example, the mechanical instability upon mechanical loading is investigated with respect to mechanical property [20], and implemented to the numerical model via quasi-convexation [73]. Nevertheless, studies on phase behaviors and especially on light-driven behaviors are largely unfound, thereby rendering both the understanding and design of smectic-solid based systems imperative. In the present section, I present a constitutive equation for finite element model that considers Sm-N-I transition by meeting the following considerations: (i) as in the studies on nematic solids [5-9], a direct relation between stimuli and mechanical responses must be established by multiphysical stimuli-order constitutive coupling; (ii) bending is a dominant deformation model upon irradiation, the method should be capable to simulate large deformation along with rigid body motion to consider bending, twisting, etc; and (iii) in addition to stimuli-responsiveness, the method should provide users with sufficient space to design the material, both macroscopically and microscopically (e.g. spatially distributed mesogen).

2.3.2.1. Light-induced Phase behavior of smectic solid

In smectic-A liquid crystal, there is no tilting between layer normal and mesogenic alignment $\vec{n}$; we therefore reduce the dot product $\vec{q}_o \cdot \vec{n}$ to the scalar layer spacing q_o. Equation (2.3.9) describes the values of order parameters for each given phase.

$$\begin{aligned} &s = 0, \quad \rho_o = 0, \quad q_o = 0 &&: \text{isotropic (I)} \\ &s \neq 0, \quad \rho_o = 0, \quad q_o = 0 &&: \text{nematic (N)} \\ &s \neq 0, \quad \rho_o \neq 0, \quad q_o > 0 &&: \text{smectic (SmA)} \end{aligned} \tag{2.3.9}$$

In order to comprehend the 1st order phase transition between each state, various models have been proposed since McMillan et al.'s [65] work, which utilizes the modified Maier-Saupe nematic model (see Ref. [38] for a comprehensive review on a theoretical model for the multi-phase model). In the present work, we employ the simple polynomial Landau model; it is not only theoretically practical due to the energetic convexity given that the parameters abide by the numerical constraints, but it can also be extended to reflect the variants of the liquid crystal composition such as molecular flexibility and external field. An adapted form of the recent work on unified phase transition [66] is presented in Eq. (2.3.10) as a Landau model; it models the comprehensive transitions between smectic (Sm), nematic (N), and isotropic (I), and even their tricritical points.

$$\begin{aligned} F\left[\underset{\sim}{Q},\psi\right] &= \int_\Omega \sigma_{LdG}\left(\underset{\sim}{Q}\right) + \sigma_{el,sm}\left(\nabla\psi\right) + \sigma_{sm}\left(\left|\psi\right|\right) + \sigma^{(1)}_{n,sm}\left(\underset{\sim}{Q},\left|\psi\right|\right) + \sigma^{(2)}_{n,sm}\left(Q,\nabla\psi\right) dv \\ &= \frac{2}{9}\left\{3as^2 - b\,s^3 + cs^4\right\} + \left\{b_1\rho_o^2 q_o^2 + b_2\rho_o^4 q_o^4\right\} + \left\{\tilde{a}\rho_o^2 + \tilde{c}\rho_o^4\right\} + \frac{2}{3}\left\{-\tilde{b}\rho_o^2 s^2 + e\rho_o^2 q_o^2 s\right\} \end{aligned} \tag{2.3.10}$$

Where σ_{LdG} , $\sigma_{el,\mathrm{sm}}$, σ_{sm}, and $\sigma_{n,sm}$ refer to the Landau-de Gennes energy in the nematic state, elastic-smectic coupling, smectic, and nematic-smectic coupling energy. These penalize a nematic phase transition, a layer dilatation, an onset of smectic phase, and a nematic-smectic transition, respectively. Note that liquid crystal distortion energy (i.e. Frank elasticity) is not considered and ρ_o, q_o, and s are presented as the variables of functional F in polynomial form because the phase behavior, in which directional distortions of LC are assumed to be negligible, is the primary consideration of the present work; hence the director distortion within the layer or the self-organizing effect of the directors are not an objective of the present work. However, it is worth to noting that such LC elasticity must be taken account whenever the alignment is distorted significantly, such as the inner coupling between mechanical load and mesogen distribution or Schlieren texture, because the present assumptions are violated due to the nonzero $\nabla\vec{n}$ that affects $\nabla\psi$.. Moreover, by ruling out the Sm-C consideration, the numerical non-convexity (e.g. chevron distribution) that stems from energy invariance regardless of the tilting direction is not considered herein. Considering the aforementioned assumptions and schematics, the present phase transition free energy is easily computed with either numerical optimization or analytic approaches. Following Ref. [66], the constitutive parameters are assumed to consider (1) the existence of solutions and (2) thermotropic Sm-A – N – I transition upon critical temperatures, T_{NA} (N - Sm-A transition) and T_{NI} (N-I transition).

$$
\begin{gathered}
b>0, \quad c>0, \quad b_2>0, \quad \tilde{c}>0, \quad \tilde{b}>0, \quad c>0, \quad e\leq 0 \\
\tilde{a}=\hat{a}\left(T-T_{NA}\right)+\frac{2}{3}\tilde{b}s_+^2, \quad b_1=\hat{b}\left(T-T_{NA}\right)-\frac{2}{3}es_+, \quad a=a_o\left(T-T_{NI}\right) \\
\hat{a}>0, \quad \hat{b}>0, \quad a_o>0
\end{gathered}
\tag{2.3.11}
$$

Figure 2.3.3 exemplifies the evolution of the order parameters during temperature change; a detailed description of the parameters is given in Table 2.3.2.

However, two aspects of the evaluation of the order parameter need to be improved. Firstly, even though the constitutive parameters presented in Table 2.3 are carefully selected in order to retain the order parameters within the acceptable range found in the experiment [65], the parameters still need to be evaluated by either fitting from the experiment or low-scale *in-silico* simulation in order to improve their physical accuracy. Additionally, the transitions between Sm-A - N and N - I are both 1st-order, marked by the C0 continuity in the graphs, which differ from the experimental results on polymerized mesogens [75], where the formation of the symmetries is attenuated by the presence of the vicinal polymeric chains.

Concerning the light-induced effect, we employ aformentioned classical dilution model (Eq. (2.3.12)), by which the characteristic temperatures for phase transition (T_{NI} and T_{NA}) are assumed to decrease in linear proportionality by the ratio of cis-molecules based on the reduction of the rigidity of the chromophores due to trans-to-cis isomerization [1, 2, 54].

$$T_{NI}\left(I\right)=T_{NI}^{0}-\beta\cdot n_{cis}\left(I\right),\quad T_{NA}\left(I\right)=T_{NA}^{0}-\beta\cdot n_{cis}\left(I\right) \tag{2.3.12}$$

In the present work, the normal layer of the liquid crystal's lamellar form and nematic director remains coaxial since the smectic-A solid is considered; a uniaxial shape conformation (i.e. shape parameter r) that is defined by the square of the ratio between the principal radii of gyration is therefore similarly used. Following the nematic description, the conformation matrices are described by r and nematic description $\vec{n}$. However, determining the shape parameter found in the smectic solid is non-trivial. The statistically based shape parameter, as in the nematic case, is not obtained due to the translational symmetry; in the nematic case, mesogenic distribution is parameterized by a unit ballS^3, whereas the smectic case requires an additional two variables for amplitude and wavelength. Therefore, in the present work, the shape parameter of the nematic case, r_n = 1+3s $r_n=1+3s$, is modified by considering additional constraints found in the experiment [42] and by definition of order parameters [66]. First, the sign invariance of ρ_o is required, as a sign of the ρ_o is trivial as shown in Eq. (1.2.1). Also, the pre-transitional effect between Sm-A and N, which flattens the uniaxial anisotropy, must be reflected, although it should increase as the temperature decreases in either the deep smectic-A or the nematic regime. Lastly, the right-handed limit of the orientational order parameter of $s^{+}\equiv\lim_{T\to T_{NI}^{+}}s$ must be included in the model, in order to build a shape parameter that comprehensively explains both the Sm-A – N – I transition and the Sm-A – I transition. The resulting shape parameter is described in Eq. (2.3.13),

$$r\left(s^*,\rho_o^*,q_o^*;\alpha,\beta,\gamma\right)=1+3\alpha s^*-\beta s^+\left[\frac{1}{\left\{1+\exp\left(-\gamma\left|\rho_o^*\right|q_o^*\right)\right\}}-0.5\right] \tag{2.3.13}$$

Here, the asterisk indicates the minimizers of smectic phase free energy, and the parameters with Roman letters (*α, β, γ*) are tunable variables where *α* is 1 when a freely jointed chain is assumed. It is worth noting that shape parameters can be obtained either by experiment or full-atomistic multiscale simulation. For the sake of brief simulation, we assume $\alpha=\beta=\gamma=1$. Note that the pre-transitional flattening effect is considered to be caused by the shifting of the sigmoid function by -0.5, which is zero in either the nematic or isotropic case (i.e. $\rho_o^*=q_o^*=0$) and rapidly settles to βs^+. In contrast to the Heaviside step function, the present term retains C^1 continuity for all real domains. This is not only beneficial to the continuity of the shape function, but also mitigates the abruptness of the 1st-order phase transition, thereby removing unphysical "jumps" during the photomechanical analysis. It is also worth noting that such a trait is also favored in analytic differentiation in gradient-based analysis such as optimization [55-56].

2.3.2.2. Constitutive relation of smectic-LCP

Concerning the constitutive equation, the elastic energy of the smectic-A solid f_{el} is considered as well as the incompressibility condition. The total potential energy functional is constructed as in Eq. (2.3.14).

$$\Pi=f_{el}\left(\underset{\sim}{\lambda},\vec{n}_o,r_o,r\right)-p\left(\det\left(\underset{\sim}{\lambda}\right)-1\right) \tag{2.3.14}$$

$\underset{\sim}{\lambda}$ is a deformation gradient and p is a Lagrange multiplier for constraint $\det\left(\underset{\sim}{\lambda}\right)\equiv J=1$. By statistical modeling of the crosslinking points of polymer strands lying on the liquid crystalline lamellar layer, a neo-classical form of the smectic-A free energy is presented in Eq. (2.3.15).

$$f_{el}=\frac{\mu}{2}tr\left(\underset{\sim}{l}^{-1}\underset{\sim}{\lambda}\underset{\sim}{l}_{o}\underset{\sim}{\lambda}^{T}\right)+\frac{B}{2}\left(\left|\underset{\sim}{\lambda}^{-T}\cdot\vec{n}_{o}\right|^{-1}-1\right)^{2} \tag{2.3.15}$$

where μ and B are the shear and layer modulus, respectively, $|\cdot|$ indicates an L^2 norm. The first term corresponds to a trace formula found in Verwey-Terentjev-Warner (VTW) energy, whereby anisotropic Neo-Hookean material is analyzed. Without biaxiality, the shape tensor $\underset{\sim}{l}$ and $\underset{\sim}{l}_o$ are uniaxial and serve as metric tensors and thus are positive definite. Equation (2.3.16) describes such a metric, comprised of a shape parameter r and a layer normal $\vec{n}$, where subscript o indicates that they are reference properties.

$$\underset{\sim}{l}_{o}=\underset{\sim}{g}_{o}=r_{o}^{-1/3}\left(\underset{\sim}{I}+(r_{o}-1)\vec{n}_{o}\otimes\vec{n}_{o}\right) \tag{2.3.16a}$$

$$\underset{\sim}{l}^{-1}=\underset{\sim}{g}^{-1}=r^{1/3}\left(\underset{\sim}{I}+(r^{-1}-1)\vec{n}\otimes\vec{n}\right)=r^{1/3}\left(\underset{\sim}{I}+(r^{-1}-1)\left|\underset{\sim}{\lambda}^{-T}\cdot\vec{n}_{o}\right|^{-2}\lambda^{-T}\left(\vec{n}_{o}\otimes\vec{n}_{o}\right)\lambda^{-1}\right) \tag{2.3.16b}$$

Note that an affine transformation from the reference to the deformed coordinate is assumed in the layer normal vector; the rotated layer normal is $\vec{n}=\underset{\sim}{\lambda}^{-T}\vec{n}_{o}/\left|\underset{\sim}{\lambda}^{-T}\vec{n}_{o}\right|$, while $1/\left|\underset{\sim}{\lambda}^{-T}\vec{n}_{o}\right|$ is the layer-to-layer distance dilatation. It is worth to remark that the present hypothesis is valid as long as the phase behavior of the material is the regime of interest, where the noncovexity of the energy is not evoked due to mechanical loading; otherwise, the layer rotation must be penalized by LC distortion energy (i.e. Frank-Oseen elasticity), such as the inner coupling that induces free soft-modes of LC rotation.

Differentiation by $\underset{\sim}{\lambda}$ of elastic energy is therefore

$$\frac{\partial}{\partial\underset{\sim}{\lambda}}\left\{\frac{\mu}{2}tr\left(\underset{\sim}{l}^{-1}\underset{\sim}{\lambda}\underset{\sim}{l}_{o}\underset{\sim}{\lambda}^{T}\right)\right\}=\mu\underset{\sim}{l}^{-1}\underset{\sim}{\lambda}\underset{\sim}{l}_{o}+\frac{\mu r^{1/3}\left(r^{-1}-1\right)}{2}\frac{\partial\left(\vec{n}\otimes\vec{n}\right)}{\partial\underset{\sim}{\lambda}}\underset{\sim}{\lambda}\underset{\sim}{l}_{o}\underset{\sim}{\lambda}^{T} \tag{2.3.17}$$

,while several equalities are required as described as Eq. (2.3.18) (where $\vec{x}$ denotes $\underset{\sim}{\lambda}^{-T}\vec{n}_{o}$)

$$\frac{\partial\lambda_{ij}^{-1}}{\partial\lambda_{pq}}=-\lambda_{ip}^{-1}\lambda_{qj}^{-1}\quad\rightarrow\quad\frac{\partial\lambda_{ij}^{-T}}{\partial\lambda_{pq}}=\frac{\partial\lambda_{ji}^{-1}}{\partial\lambda_{pq}}=-\lambda_{jp}^{-1}\lambda_{qi}^{-1} \tag{2.3.18a}$$

$$\frac{\partial n_i}{\partial \lambda_{pq}} = \frac{\partial}{\partial \lambda_{pq}} \frac{x_i}{|\vec{x}|} = -x_i \frac{x_m}{|\vec{x}|^3} \frac{\partial x_m}{\partial \lambda_{pq}} + \frac{1}{|\vec{x}|} \frac{\partial x_i}{\partial \lambda_{pq}} = n_p \lambda_{qm}^{-1} n_m n_i - n_p \lambda_{qi}^{-1} \quad (2.3.18b)$$

$$\frac{\partial x_m}{\partial \lambda_{pq}} = \frac{\partial \lambda_{ma}^{-T}}{\partial \lambda_{pq}} n_a^o = -\lambda_{ap}^{-1} \lambda_{qm}^{-1} \vec{n}_a = -x_p \lambda_{qm}^{-1} \quad (2.3.18c)$$

In short, the 1st order derivative of elastic energy as shown in Eq. (2.3.19).

$$\frac{\partial f_{el}}{\partial \underset{\sim}{\lambda}} = \mu \underset{\sim}{g}^{-1} \underset{\sim}{\lambda} \underset{\sim}{g}_o + \mu r^{1/3} \left(r^{-1} - 1\right)\left(\left(\vec{n} \cdot \underset{\sim}{B}_{eff} \cdot \vec{n}\right)\left(\vec{n} \otimes \vec{n}\right) \underset{\sim}{\lambda}^{-T} - \left(\vec{n} \otimes \vec{n}\right) \underset{\sim}{B}_{eff} \underset{\sim}{\lambda}^{-T}\right) \quad (2.3.19)$$

where $\underset{\sim}{B}_{eff}$ indicates an effective strain measure $\underset{\sim}{\lambda} \underset{\sim}{l}_o \underset{\sim}{\lambda}^T$ found in the literature on nematics [5, 6, 8]. The 2nd term of RHS of Eq. (2.31) is also derived, by employing aforementioned equalities (Eq. (2.3.18)).

$$\frac{\partial}{\partial \lambda_{pq}} \frac{B}{2} \left(\frac{1}{|\vec{x}|} - 1 \right)^2 = B \left(\frac{1}{|\vec{x}|^2} - \frac{1}{|\vec{x}|} \right) \left(\vec{n} \otimes \vec{n}\right) \underset{\sim}{\lambda}^{-T} \quad (2.3.20)$$

The Cauchy-stress $\underset{\sim}{\sigma} = \underset{\sim}{P} \underset{\sim}{\lambda}^T / \det\left(\underset{\sim}{\lambda}\right)$ is therefore

$$\underset{\sim}{\sigma} = \begin{bmatrix} \mu \underset{\sim}{l}^{-1} \underset{\sim}{B}_{eff} + \mu r^{1/3} \left(r^{-1} - 1\right) \left\{ \left(\vec{n} \cdot \underset{\sim}{B}_{eff} \cdot \vec{n}\right)\left(\vec{n} \otimes \vec{n}\right) - \left(\vec{n} \otimes \vec{n}\right) \underset{\sim}{B}_{eff} \right\} \\ + D\left(\left| \underset{\sim}{\lambda}^{-T} \vec{n}_o \right|^{-2} - \left| \underset{\sim}{\lambda}^{-T} \vec{n}_o \right|^{-1} \right) \left(\vec{n} \otimes \vec{n}\right) \end{bmatrix} - p\underset{\sim}{I} \quad (2.3.21)$$

Note that Eq. (2.3.21) is reduced to

$$\begin{aligned} \underset{\sim}{\sigma} = \mu \left(\frac{r}{r_o} \right)^{1/3} & \left[\left(\underset{\sim}{\lambda} \underset{\sim}{\lambda}^T + (r_o - 1) \underset{\sim}{\lambda} (\vec{n}_o \otimes \vec{n}_o) \underset{\sim}{\lambda}^T \right) + \frac{\left(r^{-1} - 1\right) r_o}{\left| \underset{\sim}{\lambda}^{-T} \vec{n}_o \right|^4} \left(\underset{\sim}{\lambda}^{-T} (\vec{n}_o \otimes \vec{n}_o) \underset{\sim}{\lambda}^{-1} \right) \right] \\ & + D\left(\left| \underset{\sim}{\lambda}^{-T} \vec{n}_o \right|^{-4} - \left| \underset{\sim}{\lambda}^{-T} \vec{n}_o \right|^{-3} \right) \left(\underset{\sim}{\lambda}^{-T} (\vec{n}_o \otimes \vec{n}_o) \underset{\sim}{\lambda}^{-1} \right) - p\underset{\sim}{I} \end{aligned} \quad (2.3.21)$$

that is a function of initial parameters and deformation gradient. Frame invariance is guaranteed as $\underset{\sim}{\sigma}\left(\underset{\sim}{\hat{R}} \underset{\sim}{\lambda}\right) = \underset{\sim}{\hat{R}} \underset{\sim}{\sigma} \underset{\sim}{\hat{R}}^T$ where $\underset{\sim}{\hat{R}}$ is rotation matrix. A governing equation of mechanical equilibrium is derived as in Eq. (2.3.22), where $\underset{\sim}{P}$ and $\underset{\sim}{\sigma}$ are the 1st P-K and Cauchy stresses, respectively.

$$\begin{aligned}\frac{\partial\Pi}{\partial\underset{\sim}{\lambda}}=\underset{\sim}{P}&=\begin{bmatrix}\mu\underset{\sim}{g}^{-1}\underset{\sim}{\lambda}\underset{\sim}{g}_o+\mu r^{1/3}\left(r^{-1}-1\right)\left(\left(\vec{n}\cdot\underset{\sim}{\lambda}\underset{\sim}{g}_o\lambda^{T}\cdot\vec{n}\right)\left(\vec{n}\otimes\vec{n}\right)\underset{\sim}{\lambda}^{-T}-\left(\vec{n}\otimes\vec{n}\right)\left(\underset{\sim}{\lambda}\underset{\sim}{g}_o\right)\right)\\ +B\left(\left|\underset{\sim}{\lambda}^{-T}\vec{n}_o\right|^{-2}-\left|\underset{\sim}{\lambda}^{-T}\vec{n}_o\right|^{-1}\right)\left(\vec{n}\otimes\vec{n}\right)\underset{\sim}{\lambda}^{-T}\end{bmatrix}-pJ\underset{\sim}{\lambda}^{-T}\\ &=\begin{bmatrix}\mu\left(\dfrac{r}{r_o}\right)^{1/3}\left\{\left[\underset{\sim}{\lambda}+\left(r_o-1\right)\underset{\sim}{\lambda}\vec{n}_o\otimes\vec{n}_o\right]+\dfrac{r_o\left(r^{-1}-1\right)}{\left|\lambda^{-T}\vec{n}_o\right|^{4}}\left(\underset{\sim}{\lambda}^{-T}\vec{n}_o\otimes\vec{n}_o\underset{\sim}{\lambda}^{-1}\underset{\sim}{\lambda}^{-T}\right)\right\}\\ +B\left(\left|\underset{\sim}{\lambda}^{-T}\vec{n}_o\right|^{-4}-\left|\underset{\sim}{\lambda}^{-T}\vec{n}_o\right|^{-3}\right)\left(\underset{\sim}{\lambda}^{-T}\left(\vec{n}_o\otimes\vec{n}_o\right)\underset{\sim}{\lambda}^{-1}\underset{\sim}{\lambda}^{-T}\right)\end{bmatrix}-pJ\underset{\sim}{\lambda}^{-T}\end{aligned}\qquad(2.3.22a)$$

$$\underset{\sim}{\sigma}=J^{-1}\begin{bmatrix}\mu\left(\dfrac{r}{r_o}\right)^{1/3}\left\{\left[\underset{\sim}{\lambda}\underset{\sim}{\lambda}^{T}+\left(r_o-1\right)\underset{\sim}{\lambda}\vec{n}_o\otimes\vec{n}_o\underset{\sim}{\lambda}^{T}\right]+\dfrac{r_o\left(r^{-1}-1\right)}{\left|\lambda^{-T}\vec{n}_o\right|^{4}}\left(\underset{\sim}{\lambda}^{-T}\vec{n}_o\otimes\vec{n}_o\underset{\sim}{\lambda}^{-1}\right)\right\}\\ +B\left(\left|\underset{\sim}{\lambda}^{-T}\vec{n}_o\right|^{-4}-\left|\underset{\sim}{\lambda}^{-T}\vec{n}_o\right|^{-3}\right)\left(\underset{\sim}{\lambda}^{-T}\left(\vec{n}_o\otimes\vec{n}_o\right)\underset{\sim}{\lambda}^{-1}\right)\end{bmatrix}-pI\qquad(2.3.22b)$$

As can be seen, the derived constitutive equations incorporate initial and current shape parameters, an initial director, and a deformation gradient, demonstrating the opto-mechanical coupling considering that the shape parameter is a derivative of the optical order parameters. Note that symmetries are found in the Cauchy stress tensor, which is analogous to the nematic case wherein a coaxiality between $\underset{\sim}{g}$ and $\underset{\sim}{\lambda}\underset{\sim}{g}_o\underset{\sim}{\lambda}^{T}$ is given by a rotational equilibrium. In the present case, the strong constraints on the affine deformation of the layer normal generate such inexistence of inner coupling, thereby concluding that the material is non-Cosserat. Objectivity is then satisfied in both stress measures. It is worth noting that the present findings on the inner coupling do not necessarily indicate the uniqueness of the solution; the nonlinear model of the stretching-induced buckling instability [20,73] that avoids the layer undulation is equivalent to the zero-shear stress condition of the 1st P-K stress in Eq. (2.3.22). . Let layer normal is parallel to y, and in-plane condition is employed within x-z plane. Following undulation instability condition found in reference [73], the layer spacing and the shape parameter are assumed to be maintained throughout deformation.

Assuming incompressibility, deformation gradient becomes Eq. (2.3.23) without losing generality.

$$\begin{bmatrix} \lambda_{xx} & 0 & 0 \\ 0 & \dfrac{1}{\lambda_{xx}\lambda_{zz}} & 0 \\ \lambda_{zx} & 0 & \lambda_{zz} \end{bmatrix} \tag{2.3.23}$$

Cauchy-stress is therefore expressed as

$$\begin{aligned}
\sigma_{11} &= -\frac{B\lambda_{xx}^{3}\lambda_{zx}^{2}\lambda_{zz}}{\left(\lambda_{xx}^{2}+\lambda_{zx}^{2}\right)^{5/2}} - \frac{B\lambda_{xx}\lambda_{zx}^{4}\lambda_{zz}}{\left(\lambda_{xx}^{2}+\lambda_{zx}^{2}\right)^{5/2}} + \lambda_{xx}^{2}\left(\mu + \frac{\left(B+\mu-r\mu\right)\lambda_{zx}^{2}\lambda_{zz}^{2}}{\left(\lambda_{xx}^{2}+\lambda_{zx}^{2}\right)^{2}}\right) - p \\
\sigma_{22} &= \frac{\mu}{\lambda_{xx}^{2}\lambda_{zz}^{2}} - p \\
\sigma_{33} &= -\frac{B\lambda_{xx}^{3}\lambda_{zz}\left(\lambda_{xx}^{2}+\lambda_{zx}^{2}-\lambda_{xx}\sqrt{\lambda_{xx}^{2}+\lambda_{zx}^{2}}\lambda_{zz}\right)}{\left(\lambda_{xx}^{2}+\lambda_{zx}^{2}\right)^{5/2}} + \mu\left(\lambda_{zx}^{2} + \frac{\left(\lambda_{xx}^{4}+2r\lambda_{xx}^{2}\lambda_{zx}^{2}+r\lambda_{zx}^{4}\right)\lambda_{zz}^{2}}{\left(\lambda_{xx}^{2}+\lambda_{zx}^{2}\right)^{2}}\right) - p \\
\sigma_{13} = \sigma_{31} &= \mu\lambda_{xx}\lambda_{zx}\left(\mu + \frac{B\lambda_{xx}\lambda_{zz}}{\left(\lambda_{xx}^{2}+\lambda_{zx}^{2}\right)^{3/2}} - \frac{\left(B+\mu-r\mu\right)\lambda_{xx}^{2}\lambda_{zz}^{2}}{\left(\lambda_{xx}^{2}+\lambda_{zx}^{2}\right)^{2}}\right)
\end{aligned} \tag{2.3.24}$$

Plane stress condition is satisfied when $p = \mu / \left(\lambda_{xx}\lambda_{zz}\right)^2$. Onset of the instability is computed by letting $\left\{\lambda_{xx}, \lambda_{zx}\right\} = \left\{\sqrt{\lambda_c} / \lambda_{zz}, 0\right\}$. The onset condition of the critical stretch ($\lambda_{zz} = \lambda_c$) is obtained through shear-free condition ($\sigma_{31} = 0$), which is reduced to

$$g\left(\lambda_c\right) = \frac{-B\left(-1+\lambda c\right)\lambda_c{}^2 + \mu\left(1+\left(-1+r\right)\lambda_c{}^3\right)}{\sqrt{\lambda_c}} = 0 \tag{2.3.25}$$

Equivalent condition is also found in the Ref. [20], where analytic solution is evaluated.

In recent works, the aforementioned non-uniqueness of the solution was investigated in view of the evolution of the microstructure. Such complexity stems from the non-quasiconvex governing potential; several methods have been proposed to circumvent the issue, such as quasi-convexation [76] and numerical relaxation [57]. The linearization scheme [5,8], although ruling out the unconstrained microstructure evolution (e.g. stress-free rotation of the mesogen), is proven to be sufficient whenever phase-behavior is of interest. In contrast to the soft-modes, for example, which consider mechanically induced mesogenic rotation, light-induced bending or heat-induced shrinkage does not provoke large-scale microscopic changes, possibly because they are similar to stress-free configuration for given eigenstress.

In this work, we therefore linearize the present nonlinear constitutive equation by the given assumptions: (1) due to substantially higher layer modulus than shear one, the layer dilatation remains near 1; (2) elongation tensor $\underset{\sim}{\lambda}-\underset{\sim}{I}=\underset{\sim}{H}$ is infinitesimal. The first and second assumptions are reflected by the assumed equalities presented in Eq. (2.3.26a) and (2.3.26b), respectively.

$$\begin{aligned}
\underset{\sim}{\lambda}\underset{\sim}{\lambda}^{T} &\mathrel{\hat{=}} \underset{\sim}{I}+\underset{\sim}{H}+\underset{\sim}{H}^{T} \mathrel{\hat{=}} 1+2\underset{\sim}{\varepsilon}, \quad \underset{\sim}{\lambda}^{-1} \mathrel{\hat{=}} \underset{\sim}{I}-\underset{\sim}{H} \\
\underset{\sim}{\lambda}\left(\vec{n}_o\otimes\vec{n}_o\right)\underset{\sim}{\lambda}^{T} &\mathrel{\hat{=}} \left(\vec{n}_o\otimes\vec{n}_o\right)+\underset{\sim}{H}\left(\vec{n}_o\otimes\vec{n}_o\right)+\left(\vec{n}_o\otimes\vec{n}_o\right)\underset{\sim}{H}^{T} \\
&\mathrel{\hat{=}} \left(\vec{n}_o\otimes\vec{n}_o\right)+\left(\underset{\sim}{\varepsilon}+\underset{\sim}{\omega}\right)\left(\vec{n}_o\otimes\vec{n}_o\right)+\left(\vec{n}_o\otimes\vec{n}_o\right)\left(\underset{\sim}{\varepsilon}-\underset{\sim}{\omega}\right)
\end{aligned} \tag{2.3.26a}$$

$$\begin{aligned}
&\underset{\sim}{C}\equiv\underset{\sim}{\lambda}^{T}\underset{\sim}{\lambda}, \quad \left|\underset{\sim}{\lambda}^{-T}\vec{n}_o\right|=\sqrt{\vec{n}_o\cdot\underset{\sim}{\lambda}^{-1}\underset{\sim}{\lambda}^{-T}\vec{n}_o} \\
&1/\sqrt{\vec{n}_o\cdot C^{-1}\vec{n}_o}^{\,4}=1+4\left(\vec{n}_o\cdot\underset{\sim}{\varepsilon}\cdot\vec{n}_o\right) \\
&\sqrt{\vec{n}_o\cdot C^{-1}\vec{n}_o}^{\,-4}-\sqrt{\vec{n}_o\cdot C^{-1}\vec{n}_o}^{\,-3}=\left(\vec{n}_o\cdot\underset{\sim}{\varepsilon}\cdot\vec{n}_o\right)
\end{aligned} \tag{2.3.26b}$$

By introducing scaled layer modulus $\hat{b}\mathrel{\hat{=}}B/\mu\left(r_o/r\right)^{1/3}$, the linearized constitutive equation is obtained as in Eq. (2.3.27).

$$\sigma=\mu\left(\frac{r}{r_o}\right)^{1/3}\begin{bmatrix}
\underset{\sim}{I}+2\underset{\sim}{\varepsilon}+\left(\vec{n}_o\cdot\underset{\sim}{\varepsilon}\cdot\vec{n}_o\right)\left(\vec{n}_o\otimes\vec{n}_o\right)\left\{4\left(\frac{r_o}{r}-r_o\right)+\hat{b}\right\} \\
+\left\{\underset{\sim}{\varepsilon}\left(\vec{n}_o\otimes\vec{n}_o\right)+\left(\vec{n}_o\otimes\vec{n}_o\right)\underset{\sim}{\varepsilon}\right\}\left(2r_o-\frac{r_o}{r}-1\right) \\
+\left\{\underset{\sim}{\omega}\left(\vec{n}_o\otimes\vec{n}_o\right)-\left(\vec{n}_o\otimes\vec{n}_o\right)\underset{\sim}{\omega}\right\}\left(\frac{r_o}{r}-1\right) \\
+\left(\vec{n}_o\otimes\vec{n}_o\right)\left(\frac{r_o}{r}-1\right)
\end{bmatrix}-p\underset{\sim}{I} \tag{2.3.27}$$

In contrast to the conventional stress-strain equation, the present constitutive equation contains both infinitesimal strain $\underset{\sim}{\varepsilon}$ and rotation $\underset{\sim}{\omega}$. A fourth term indicates an eigenstress induced by phase behavior, which is a function of the initial/current shape parameters and initial director.

In order to maintain flexibility with comprehensive smart actuation, liquid crystal polymer is frequently fabricated in the form of a thin strip; a flat faceted shell is therefore formulated herein. We assume that plane stress condition is applied in the z direction by assuming that both the nematic director and the layer normal found in the smectic liquid crystal are located within the x-y plane. The present assumed directions correspond to the alignment methods, by which director remains in-plane, as well as the principal modes of actuation such as uniaxial elongation and bending, driven by a gradient generated in the transverse (z) direction. Equation (2.3.28) shows the plane stress condition, whereby the Lagrange multiplier p is determined on the basis of incompressibility (i.e. $Tr\left(\underset{\sim}{\varepsilon}\right)=0$).

$$\begin{aligned} &\sigma_{33}=\mu\left(\frac{r}{r_o}\right)^{1/3}\left[1+2\varepsilon_{33}\right]-p=\mu\left(\frac{r}{r_o}\right)^{1/3}\left[1-2\varepsilon_{11}-2\varepsilon_{22}\right]-p=0 \\ &\sigma_{3\alpha}=0 \end{aligned} \tag{2.3.28}$$

In conclusion, the constitutive equation of plane stress is derived as Eq. (2.3.29). The elastic term ($\sigma_{\alpha\beta}^{\varepsilon}$) and eigenstress term ($\sigma_{\alpha\beta}^{ph}$) are found, where the Roman indices range between integer 1 and integer 2.

$$\begin{aligned} &\sigma_{\alpha\beta}=\sigma_{\alpha\beta}^{\varepsilon}\left(\underset{\sim}{\varepsilon},\underset{\sim}{\omega},r,r_o,\vec{n}_o\right)+\sigma_{\alpha\beta}^{ph}\left(r,r_o,\vec{n}_o\right) \\ &\sigma_{\alpha\beta}^{\varepsilon}=\mu\left(\frac{r}{r_o}\right)^{1/3}\left[\begin{array}{l} 2\left(\varepsilon_{11}+\varepsilon_{22}\right)\delta_{\alpha\beta}+2\varepsilon_{\alpha\beta}+\left(n_\gamma^o\varepsilon_{\gamma\eta}n_\eta^o\right)n_\alpha^o n_\beta^o\left\{4\left(\frac{r_o}{r}-r_o\right)+\hat{b}\right\} \\ +\left\{\varepsilon_{\alpha\gamma}n_\gamma^o n_\beta^o+n_\alpha^o n_\eta^o\varepsilon_{\eta\beta}\right\}\left(2r_o-\frac{r_o}{r}-1\right)+\left\{\omega_{\alpha\gamma}n_\gamma^o n_\beta^o-n_\gamma^o n_\alpha^o\omega_{\gamma\beta}\right\}\left(\frac{r_o}{r}-1\right) \end{array}\right] \\ &\sigma_{\alpha\beta}^{ph}=\mu\left(\frac{r}{r_o}\right)^{1/3}\left(n_\alpha^o n_\beta^o\right)\left(\frac{r_o}{r}-1\right) \end{aligned} \tag{2.3.29}$$

In contrast to the nematic cases, shear modulus does not converge to 0 regardless of the ratio of the shape parameters. Such effect arises due to the rigid constraint on the layer normal, and indicates that shear-induced softness is significantly alleviated in the smectic case.

2.4. Light-induced deflection of nematic solid

In this chapter, out-of-plane displacements induced by prescribed light and thermal stimuli are discussed. A primary finding includes the amount of the induced curvature and the deflection of that material where a geometric nonlinearity and a non-monotonicity are demonstrated. An anomalous phase behavior observed in the photon-bombarded material is also found to be correlated with experiments.

Light-induced bending behaviors observed in both nematic and smectic solids are firstly presented in terms of curvatures in the longitudinal direction. By examining steady-state solutions of light-induced shape change, nonlinearities either stem from the photobleaching effect or from large geometric deformations are found to be significant; the deflections and curvatures are both *overestimated* if linear solution is assumed. Such nonlinearities are found and discussed via comparison to linear solutions. I compare the light conditions and temperature stimuli that lead to two solutions.

To further demonstrate the capability of the present work, radially-distributed director with circular domain is examined next with parametric changes of incident light. This is in the same line of the experiment [33], which generates either conic (radial expansion) or sombrero (radial shrinkage) shape upon different stimuli conditions.

Lastly, the effects of the anomalous phase behavior with respect to photo-bending are investigated. This is compared to the results based on linear assumptions: (1) the dilute model that assumes the *cis-* molecule as a dormant inhomogeneity hence linearly reduces clearing temperature, and (2) negligible effect from chemical crosslinking, which indicates rotation and kinking of the *trans-* azobenzene is stress-free mode.

Figure 2.4.1 shows an LCP sheet model investigated throughout this work. L_x and L_y denote the length in the x and y directions, respectively; h represents the thickness of the model, whereas $f(z)$ represents the angle between the director $\boldsymbol{n}$ and the polarization angle of linearly polarized light (LPL), which varies with thickness. Material parameters were set to their experimentally fitted values whenever not specified otherwise (T_{NI}^{o} =340 K, α =0.22, ζ =0.195, and β =11.8), which correspond to polymeric compositions comprised of pendent- and crosslinked-type molecules (BMAzo, PBB, DiUB; full names of these materials can be found in Ref. [54]). A shear modulus μ is set to 10^4 [Pa], following experimental reports [39,54] on elastomeric LCPs.

2.4.1. Geometric nonlinearity and non-monotonicity of photobending

Upon *cis*- to *trans*- isomerization, clearing temperatures of the order, by which nematic-to-isotropic and nematic-to-smectic is divided, decreases. A decaying energy of the traveling photons inevitably generates a local gradient of such temperatures, thereby induces out-of-plane curved shape. In this section, curvatures and deflections found in the deformed shape is parameterized by amount of the stimuli and discussed in terms of nonlinearity and non-monotonocity.

Due to the spatially graded strain generated in the out-of-plane direction, the LCP strip bends when it is exposed to UV illumination. If the nematic orientation is aligned parallel to the direction of length (***n***//***x***), which generates surface-dominant longitudinal contraction, the LCP strip bends towards the light source. The effects of light intensity and penetration depth on the bending behavior are investigated (Fig. 2.4.2). The bending behavior is characterized by the bending curvature κ evaluated through 3rd-order polynomial fitting (Eq. (2.4.1)) of the *x*-*z* profile of the deformed shape in order to alleviate the complexity of comparing surface curvatures.

$$\begin{gathered} u_z = a_i x^i, 0 \le i \le 3; i \in \mathbf{Z} \\ \kappa\left(x=0\right) = u_z''\left(x=0\right) \Big/ \left(1+u_z'\left(x=0\right)^2\right)^{3/2} = 2a_2 \Big/ \left(1+a_1^2\right)^{3/2} \end{gathered} \tag{2.4.1}$$

In Fig. 2.4.2(a), the penetration depth *d* is varied while the temperature *T* is fixed at 298 K, for which liquid crystals are deeply within the nematic phase. As previous works have asserted [5, 8, 9], I also found that the bending behaviors are highly nonlinear for increased intensities of light, as they are dependent upon the spatial gradient through the thickness [see inset of Fig. 2.4.2(a)]. The influence of geometric nonlinearity on the solution is also demonstrated by comparing the curvatures computed from linear and nonlinear finite element solutions. Despite the small curvatures, Fig. 2.4.2(b) exhibits the salient gaps between linear (dotted line) and nonlinear (solid line with marks) solutions for increased temperature. In general, nonlinearity trends follow the profile of deflection as this indicates a higher bending moment; the gap between linear and nonlinear models is profound when the penetration-depth-to-thickness ratio (d/h) is 0.4, where a maximal gap (44%) is found at the apex of the profile. On the other hand, for d at both extremes (0.01 and 10) compared to the thickness, the deformation is in-plane dominant; therefore, geometric nonlinearity and bending deflection are both restricted. Although not discussed herein, geometric nonlinearity of the LCP cantilever with uniform mesogenic orientation, thickness has no influence as long as the ratio of light penetration over thickness d/h remains constant.

Concerning the temperature, for an elevated temperature (310 K) smaller than the transition temperature T_{NI} (=340 K), both curvature discrepancy and displacement increase due to the significant uniform decrease of the shape parameter. These results assert not only the nonlinear sensitivity of intensity to external stimuli, but also to the LCP sheet design criteria, because light-order parameters such as penetration depth d and the phase-and-light connecting parameter α are determined during the synthesis process [2]. Therefore, more extensive experimental and theoretical studies on the synthesis are required, because they may enhance the capability of the proposed framework. Incidentally, it is also found that the light intensity at the curvature peak and overall shape do not coincide. This is another indication of nonlinearity because it demonstrates that, contrary to the linear case, larger bending does not necessarily yield larger curvature.

To dramatically demonstrate the nonlinear behavior of the anisotropic solid with light irradiations, the disclination defect imprinted on the LCP directors is also studied. Radially distributed mesogens, for instance, induce contractile photostrain in the radial direction, as well as positive photostrain in the azimuthal direction. Accordingly, geometric instability inevitably occurs and drives an initially 2D plate to become a 3D structure. Here, I investigated a radial topology defect with a strength of +1, and with a missing row in the center, in order to demonstrate two aspects: (1) the extent of external stimulation required for the instability onset, and (2) the reproduction of the experimentally reported topological changes.

In Fig. 2.4.3, the disclination-driven instability produced by imprinted radially distributed mesogens and actuation due to the light irradiation and elevated temperature are illustrated respectively. A quarter of the model (R_x=R_y=20mm, with thickness 0.4) is simulated, and clamped conditions are applied at the center node. The dramatic effect of nonlinearity is illustrated in Fig. 2.4.3(a). The two LCP sheets under different conditions are significantly different, even though they have similar geometric properties (i.e., thickness and radius) and are subject to the same stimulation conditions (i.e., temperature and light intensity). The difference stems from the geometric instability that arises from the radial distribution of light-induced strain and its Poisson effect. In the linear solution, the LCP behavior is bending-dominated, yielding the Mexican hat shape. On the other hand, the LCP sheet becomes unstable following irradiation by light, and exhibits buckling-like behavior at the bifurcation point. The observed shape of anticlastic curvature with an apex at the center agrees well with recently reported experimental results [17,18,33]. Ground states from other mechanically frustrated cases, such as s = -1, s = -2 can also be solved via same numerical method.

To quantify the bifurcation point, after which the nontrivial deformation solution can be obtained, a scaled standard deviation of out-of-plane displacement shown at the boundary nodes (W) is proposed. The onset of instability is clearly illustrated in Fig. 2.4.3(b), where the threshold is set to 0.1. A Mexican hat shape is shown for the pre-bifurcation linear regime, whereas a saddle shape is observed elsewhere. The present study also discloses the dependence of the critical light intensity on temperature and *d/h*. According to this study, the critical intensity is smaller for increased depth of light penetration, and continuously decreases even when *d/h* is much larger than unity. It is worth to remark that such a snap-through instability in deep-nematic condition is provoked by a membrane compression, which increases continuously with respect to light. These phenomena are well explained by an analogy to an analytic solution of radial FGM sheet instability [77], which suggests that only the ratio of membrane resultant to bending rigidity, N_{rr}^{ph} / D_{rr}, contributes to the critical amount of external loading.

2.4.2. Nonlinearity from the microscale origin

Aforementioned nonlinear behaviors are originated from either the finite strain measure, or the distribution of the light-induced moment. On the other hand, the material-related nonlinearity is discussed in this subsection; networked rigid molecules, in the contrary to the un-functionalized liquid crystal molecules, show an distinguished phase behavior as they are affected not only by neighboring molecules but also polymeric hydrocarbon networks.

With the aid of the multiscale-based framework, I investigate the bending behaviors by which a light-responsive LCP deforms under actinic light. As shown in Fig. 2.4.4(a), a cantilevered thin LCP strip is bombarded with light (intensity: I_o) that travels in the −z direction, as well as a separate stimulus for elevating the temperature T; these external stimuli drive the *trans-to-cis* isomerization and the thermal-induced *cis-to-trans* isomerization, respectively. Herein the deformations related to light and temperature are discussed in a scaled manner by introducing the reference light intensity I^{ref} and time constant τ_c. The initial director ($\vec{n}$) is aligned along the x-axis, so the LCP's deflections and rotations are each defined by the nodal displacement in the z direction and rotation of the normal vector along the y-axis, as the significant bending curvature change is observed in the x-z plane. A deep nematic phase is assumed to exist prior to and during crosslinking. I refer to the initial temperature as T_o, which is lower than the clearing temperature T_c^o ($T_o = 0.7 T_c^o = 322.35\ \mathrm{K}$) under non-irradiated conditions; the initial polymer structure is therefore highly anisotropic (i.e. shape parameter $r > 1$).

The results presented in Fig. 2.4.4 illustrate the deformation of the strip (color indicates the value of r) as well as the varying shape parameter along the transverse z direction found at points A, B, C, and D, which are plotted along the x-axis; in this context, h represents the thickness of the strip. These results indicate that the bending behavior is strongly affected by varying the stimuli. Typical bending occurs where the surface-dominant shape parameter change is observed under weak light conditions, which follow Beer's law. For intense light conditions ($I_o / I^{ref} = 8$), on the other hand, light penetrates deeply into the material, which is known as the photo-bleaching effect, and thus the gradient of the shape parameter is reduced; r converges to unity (i.e. the polymeric shape becomes isotropic and thus shrinks in the longitudinal direction) near the base of the LCP cantilever as a large number of *cis*- molecules are stacked, which reduces T_c closer to the operating temperature. In this way, in-plane shrinkage overshadows the bending moment. Elevating the temperature ($T_o / T_c^o = 0.9$) significantly enhances the backward reaction of isomerization and provides polymeric flexibility, thereby reducing deformation.

The overall behavior of the LCP is summarized in Fig. 2.4.5. Figure 2.4.5(a) illustrates the tip deflection (z-position) with respect to time; here we can clearly observe non-monotonic deflection. The saturated value of the final deflection increases with intensity for low-intensity light conditions (i.e. $I / I_{ref} \leq 4$), though it decreases as the intensity increases beyond this threshold, as the shape parameter profile suggests. Furthermore, as shown for $I_o / I^{ref} \geq 6$, the reduced deformations do not settle and continue to decrease even beyond the time constant $\tau^{\propto}$.

At a point near the base (i.e. point A in Fig. 2.4.4(a)), the accumulated high cis-population significantly dilutes the mesogenic order, and hence renders the local polymeric structure isotropic. The tip of the LCP is subsequently lowered because of the flattened base, which decreases the incident angle ϕ, and hence the local equilibrium is attained again. At this stage, the deflection is then further decreased until the LCP becomes totally flat [42]. The time required to obtain a specific tip deflection (h* = 16 h or 20 h) is examined in Fig. 2.4.5(b). A decaying profile can be observed as the characteristic time becomes more sensitive to light for lower intensities. The relaxation of the polymeric segment due to increased temperature is also reflected in the shift of the curves for different values of *T*. This behavior provides insight into the LCP's experimentally observed characteristic bending phenomena [40,42], which could not be explained solely based on a priori estimations based on photo-strain [56].

In order to exemplify the benefits of the methodology presented in this work, we also compare the results obtained by the present framework to those from the classical dilute model, as shown in Fig. 2.4.6. All classical results present hereafter (marked as "Dilute") are obtained using the previous finite element study with constant thermotropic parameters (α =1.4, ζ =0.33, and $T_c^o = 462.52$) through MD simulations under non-irradiation conditions (n_{cis} =0). Additionally, the order-clearing temperature is assumed to decrease linearly according to the following formula: $T_c = T_c^o - \beta \cdot n_{cis}$, where $\beta = 88.8$. In both computations, $I^o / I^{ref} = 4$, $d / h = 0.4$, and rotations and displacements are obtained at the tip at time $\tau^{\propto}$.

First, a rotation is computed across a wide range of LCP thicknesses (Fig. 2.4.6(a)). A deflection of 90° for the tip is expected for thin sheets; such a configuration is widely observed in experiments (see Figs. 2.13(d) and (e)) concerning side-chain acrylate LCPs. As Fig. 2.4.6 (a) illustrates, the multiscale framework provides a better estimation of the shape change over the other solution. In particular, the deflection of the tip computed by the classical dilute model is significantly underestimated; the deflection remains far below 90° even when the bending stiffness is significantly reduced owing to the high length-to-thickness ratio (>70). Furthermore, the results of tip displacement (Fig. 2.4.6(b)) similarly indicate that the classical solution underestimates the shape change.

Such deviation can be attributed to the slope of the reduced anisotropy r/r_o curve, as illustrated in Fig. 2.4.6(c). The two models are utilized for the case of identical geometry, light intensity, and temperature; accordingly, they yield the same n_{cis} distributions. A stronger gradient of r in the multiscale model is therefore induced by a decrease/increase in α / ζ , as reflected in Fig. 2.3.2(b). It encompasses an additional effect from trans-to-cis isomerization that affects the order itself; the classical results, insofar as they do not account for the stacking characteristic, therefore underestimate the deformations.

It is worth mentioning that such effects from polymeric architecture can also be found in the silicon-based side-chain liquid crystal elastomer when it incorporates crosslinked-type azobenzene (aside from the pendant variety). More specifically, it undergoes order change with an increasing number of cis- isomers. This similarity clearly demonstrates that the multiscale simulation and concomitant lower-scale in silico experiment are capable of accounting for the molecular conformation in general opto-mechanical structures. However, the effects of changes in the polymeric structure upon the mechanical properties, such as the optimum actuation temperature and light-induced stress, cannot be validated in the present work, as we only provide preliminary considerations of the effects on bending and nonlinear photomechanics. It is therefore necessary to consider temperature-induced molecular flexibility (considered separately from order-induced change) in future studies.

2.5. Light-induced deflection of smectic solid

In this section, we present various aspects of the phase behaviors of smectic solids. Materials deform to accommodate the internally generated stress owing to the change of the order of the parameters (i.e. degree of symmetries and anisotropy of the microscopic conformation). Equation (2.5.1) is a paraphrased relation that computes deformation u (midplane displacement) and θ (midplane rotation) for given shape parameter *r*; being a stress-free configuration, the solution of the equation is essentially equivalent to the eigenstrain problem frequently found in numerous multiphysical studies.

$$\sigma_{\alpha\beta} = \sigma_{\alpha\beta}^{el}\left(u,\theta;r,r_o\right) + \sigma_{\alpha\beta}^{ph}\left(r,r_o\right) = 0 \tag{2.5.1}$$

It is worth noting that the constitutive relationship does not converge to the nematic case [8] when neither the reference nor the current states are in the smectic-A phase, due to the violations of the assumptions imposed on the smectic layer: affine deformation of the normal vector, and nonzero layer modulus. Therefore, the phase behavior analysis of the non-smectic-A solid, of which the crosslinked and reference traction-free state are nematic or isotropic is not carried out herein. Accordingly, a deep smectic phase is assumed to be created upon crosslinking in all simulations (i.e. $T_o = T_{NA} - 30K = 320K$), while the operating temperature $T \in [320, 360]$ and effective intensity of incident light $I_{eff} \in [0,2]$ vary. The temperature-induced effects other than phase behavior are ignored herein, as the behavior of the LCP is dominantly governed by polymeric conformation change when compared to thermal expansion [2].

2.5.1. Pre-transitional phase behavior

Without light, the temperature increment uniformly changes the shape parameters, as in the order parameters (s^*,ρ^*,q^*) found in all material points. The thin strip thereby undergoes uniaxial shrinkage as shown in Fig. 2.5.1.

Upon heating, the length of the specimen shows a non-monotonic decrease as found in the experiment [42], wherein pre-transitional anomalies are found between the smectic-A and nematic phase; such behavior is already depicted in the shape parameter, of which the relation to deformation is illustrated in the inset of Fig. 2.5.1(b). The uniaxial change also agrees well with the one-dimensional (1-D) material behaviors (marked by dots) based on the nonlinear equation directly originating from $\partial f / \partial \lambda = 0$, combined with the uniaxial deformation gradient $\underset{\sim}{\lambda} = diag\left(\lambda^{-1/2},\lambda^{-1/2},\lambda\right)$, where λ is a scalar valued extension. This demonstrated that the effect from assumptions made during formulation and linearization are found to be virtually negligible when layer modulus B is higher than 20, so that dilatation does not significantly deviate from unity. It is also worth noting that mechanically induced layer undulation (i.e. CMHH instability [78] is not provoked as the phase behavior is stress-free behavior, and the elongation mode thus does not compete with the shear modes.

2.5.2. Light-induced bending of smectic solids

As a primary objective of the present work, light-induced deformation is also investigated via numerical simulations. A combination of multiphysical consideration and FEA is shown in Fig. 2.5.2., which is similar to that in the previous study on the steady-state light-responsive behavior of nematic solids; modifications have been made in the phase transition computations, conformations, and constitutive equations.

Provided that two temperatures (crosslinking T_o and operation T) and the intensity of light irradiation I_{eff} are specified, the spatial distribution of the order parameters can be computed via a dilute model and light decay profile, which in turn computes the shape of the polymer conformation. Figure 4 shows the normalized light intensity and light-affected change of the internal properties; the gradients in the transverse direction, which originated from light decay, are essential to compute the light-induced curvature of the specimen.

Note that light decay follows the classical Beer's law, which is often substituted by the nonlinear Lambert-W function that describes the photobleaching effect [49-51] as there is no experimental evidence of such phenomena in smectic solids. Nevertheless, the derivatives of light, such as n_{cis} and r , possess nonlinear thickness-varying profiles. In addition, a sigmoid term found in the shape parameter in the pre-transitional regime generates a non-monotonic form.

The dimensions of the smectic-A strip are 20 mm x 1 mm x 500 um by Length (L) x Width (W) x Thickness (h), respectively, in which the length-to-thickness ratio is higher than 20 to retain the validity of the thin-plate assumption. 1280 mesh is used, the size of which is assumed to be uniform. We assume that the left boundary ($x = 0$) is clamped, while the director vector is $\{1,0,0\}^T$, which is in the longitudinal direction. We also set μ = 1.5 Gpa, B / μ = 20, and *d/h* = 0.4; these material properties are fixed hereafter, unless otherwise specified.

2.5.2.1. Temperature-alternating bending direction

Due to the gradients generated in the out-of-plane direction, the thickness-varying modulus and the eigenstress are present, which are analogous to the functionally graded material (FGM). Consequently, an out-of-plane deflection in agreement with the boundary conditions is generated. Figure 2.5.4 illustrates the light-induced bending in terms of the curvature with various temperatures and penetration depths. A deflection curve evaluated at the middle of the width ($y / W = 0.5$) is well-fitted using the quadratic polynomial function (||Goodness of fit|| ~ 0.99), Eq. (2.5.2) computes the principal curvature at the center of the specimen.

$$\begin{gathered} u_z = a_i x^i, 0 \le i \le 3; i \in \mathbf{Z} \\ \kappa\left(x = L/2\right) = u_z''\left(x = L/2\right) \Big/ \left(1 + u_z'\left(x = L/2\right)^2\right)^{3/2} \end{gathered} \tag{2.5.2}$$

As shown in Fig. 2.5.4(a) and 2.5.4(b), the profiles of bending curvature with light increment exhibit salient nonlinearity and non-monotonicity. In terms of the operating temperature T that ranges from T_{NA} *- 30K*, to T_{NA} *+ 10K*, three different regimes are found as we increase the temperature: smectic-dominant, pre-translational, and nematic-dominant. If the diluted transition temperature remains higher than the operating temperature T (T < 330 K), the curvature is proportional to the irradiation; an increase of the degree of symmetry is directly reflected in the shape parameter. Upon an increase of the temperature below T_{NA}, the curvature profile reverses: it first bends away from the incident direction at low intensity, and bends towards the light at a higher intensity. Such phenomenon originates from the assumption of the shape parameter that bears the sigmoid term which reflects the pre-transitional state: As long as the initial state resides in deep smectic phase, the materials undergo a subsequent transition from smectic, nematic, and isotropic as temperature increases. Hence the eigenvalue to the principal direction of the metric tensor first increases as soon as the effective temperature at the material point exceeds T_{NA}, and later decreases when its state becomes nematic and isotropic. The alternating bending direction, therefore, distinguishes the smectic solids from nematic ones, which exhibit monotonic bending behaviors. Finally, the photomechanical behavior of the smectic solids operating above the T_{NA} exhibits a consistent bending direction. Such temperature dependent bending phenomenon agrees well with the experimental reports on smectic-A liquid crystal polymer [74] that undergoes sequential phase transition from smectic-A, to nematic, and then to isotropic. The transition points of the slope also agree, whereby the T at the material points partially becomes higher than T_{NI} (i.e. isotropic) due to the dilution of the T_{NI} temperature. The curvature slope obtained thereafter is analogous to that of the nematic-isotropic photomechanical behaviors reported in previous work [5].

The penetration depth of the light is also investigated parametrically by fixing the operating temperature at 330 K, which shows the aforementioned alternating bending direction as it is within the intermediate regime. Upon an increase in the penetration depth, by which light travels further into the material, a stronger gradient of the conformation is developed, as demonstrated by the large deviation between the two bending curvatures at the maximal bending-away-from and bending-toward the light.

For each photomechanical computation, the local rotation of the layer normal (ϕ) as an auxiliary parameter is also investigated. It is not only an important observation in optics (e.g. polarized microscopy), but also serves well in demonstrating the quasi-softness of the material. Obtained from Eq. (2.48), the profile of ϕ with respect to the light intensity and spatial locations (A, B, and C) are plotted in Fig. 2.5.5. Note that the local rotation possibly changes the elasticity of the LC layers and alignments, as is often considered in terms of Frank elasticity, which is assumed to be negligible in the present work due to the infinitesimal rotation induced by phase transition and the nonconvex nature of the energy. If such elasticity is included within the model, we presume that the rotation is further restrained due to penalization. Hence the rotation presented in the present study must be considered as the upper bound, given that only a phase behavior is provoked by either thermal or optical stimuli.

$$\vec{n} = \{\cos\phi, \sin\phi\}^T = \underset{\sim}{\lambda}^{-T}\vec{n}_o / \left|\underset{\sim}{\lambda}^{-T}\vec{n}_o\right| \cong \left(1-\underset{\sim}{\varepsilon}\right)\vec{n}_o / \left|\left(1-\underset{\sim}{\varepsilon}\right)\vec{n}_o\right| \qquad (2.5.3)$$

As shown in Fig. 2.5.5(a), the rotation is found to be distributed inhomogeneously in the bent solid, where larger rotations (both positive and negative) are found near the clamped boundary. Such distribution accords with the shear strain distribution found in the bent plate that is subject to the clamped boundary, since ϕ is strongly dependent on the shear strain; such effects are therefore possibly analyzed only by considering the boundary conditions and not by the 1-D beam model [8 ,79]. To further discuss the influence from the boundary condition, the three different locations (A: at the clamped base (*x/L* = 0.1), B: at the middle (*x/L* = 0.5), and C: at the tip (*x/L* = 1) are investigated. Upon the increase of light intensity, the rotation found at each position evolves. However, the gradient and signs of the rotation profile with respect to the y position (i.e. width direction) differ from each other. Especially, the profile found in position A has an inverse slope, and a magnitude that is one order higher than the others; such behavior demonstrates the boundary effect, which is analogous to the Saint-Venant boundary layer. It is worth again noting that such distribution of the rotation is one of the pivotal properties in optics, as it changes the amount of opacity of the material. Even though no experimental proof has been provided to date, the authors believe that: (1) the opacity of the specimen is not evenly distributed after bombardment of the UV light and (2) such distributions are strongly correlated with the boundary conditions, both of which are easily validated through a polarized microscope.

2.5.2.2. Effect of geometric nonlinearity

The influence of geometric nonlinearity on the solution is also demonstrated in

Fig. 2.5.6, wherein the curvatures computed from linear (dot) and nonlinear (line) finite element solutions are presented respectively.

Even though the curvature itself is within 0.1 /mm for all explored ranges of light intensity and temperature, its deviation in percentile is proven to be substantial, which means we might severely underestimate the curvature of the light-responsive smectic solid if linear solution is employed. As in nematic solids, nonlinearity is generally proven to be substantial when the magnitude of curvature increases. The use of nonlinear finite element solution is therefore recommended, regardless of the operating condition, as the direction and the magnitude are strongly non-monotonic and thus, estimating their pick values is non-trivial. Otherwise, we might produce an incorrect estimation to the point where the sign of curvature changes. Moreover, such overestimation can produce error in the internal parameters as shown in the inset in Fig. 2.5.6, wherein the linear case shows a more dramatic contrast of the rotation as shear strain near the tip is strongly influenced by the rigid body rotation. Considering that rotation ϕ is pivotal in the optical characterization of solids, the linear solution might cause severe degradation of the computation. Although not shown herein, this finding is in the same line with that of the curvature evaluated at the clamped end, and the maximal deflections are overestimated in the linear case. Moreover, these deviations are alleviated when simply-supported boundary conditions are imposed.

2.6. Light-induced deflection of solids with distorted nematic

The liquid crystal molecules confined within a planar cell forms an optical texture. With no aligning treatment, for example, the molecules are organized around the disclination defect (i.e. a point where director vectors exhibit discontinuity) that is often referred as “Schlieren texture”. Such distribution is contrary to the texture obtained after the rubbing process, on the other hand, where the molecules are aligned uniformly. The term ‘intrinsic variable’ that imposes the modulation in pre-crosslinking steps is inspired by the fact that such inhomogeneous distribution of nematic vectors induce similar strain field, which generates nontrivial shape change; in the contrary to extrinsic ones, small-scale design parameters indicates a changes of local liquid crystallinity, which can be determined before crosslinking. The potentials and challenges of such design schematics are well documented in the recent review [45]. In this subsection, the thickness-wise variation of the nematic distortion, and the in-plane texture of the LCP is discussed along with their potential usage.

2.6.1. Curvature evolution due to distorted nematics

Figure 2.6.1 shows a configuration of the thickness-wise alignment of liquid crystal underwent twisted nematics (TN) distortion. Assuming that pitch of the twist is irrelevant to the phase transition, a negative strain of which principal direction linearly changes with thickness. Through the experiment [17], LCP with TN configuration exhibits saddle shape whenever thermally-induced phase change is executed.

A change of principal direction due to the change of mesogen director imprinted on the LCP film is the mechanism underlying the deformation. The twist configuration of mesogens, one of the Fredericks transitions that evolves within the material thickness is examined in this subsection. In addition to temperature-induced deformation, the shape of which can be determined analytically [80], light intensity and decaying profile dependent deformation are analyzed.

During crosslinking, when liquid crystal molecules retain their orientational mobility, external conditions (such as mechanical loading) produce depth-dependent mesogenic orientations. In the twist configuration shown in Fig. 3.3.1(a), directors remain in-plane while direction gradually changes from top to bottom. This generates eigenstress (or eigenstrain) as a function of depth z, yields maximal anticlastic curvature ($\kappa_{xx}= \kappa_{yy}$) when heated [80], and twists when irradiated [81]. In addition, angles with respect to LPL are also inspected; when the angle of the Poynting vector does not coincide with the axis of the chromophore, the effective intensity of the chromophore extracted from photonic vibrations decreases. The simplest model for such phenomena is given by Eq. (2.6.1).

$$I_{eff}(\phi) = I_{eff}^{o} \cos^2(\phi) \tag{2.6.1}$$

Figure 2.6.1(a) exhibits the modeling of the twist configuration and its effect on the shape parameter r that evolves in the out-of-plane direction. The midplane angle $\phi_o = \phi(z=0)$ is assumed to be π/4, while the span of surface to bottom rotation is fixed at π/2. When the LPL is incident on the surface, minimal energy is transmitted to the molecules at the top, which smoothly increases as ϕ grows smaller and decreases as the decay of light overwhelms the phenomena. Increased intensity generates deeper and more isotropic-like behavior, while retaining the general shape parameter profile. On the other hand, the penetration depth d strongly affects the behavior in terms of both value and depth of shape parameter profile. Increased temperature simply shifts the profile, as decaying influence is extracted from the model. Such a profile of shape parameter, by which the depth-varying principal direction of the eigenstress model is induced, emphasizes the modeling capability of the present work for two main reasons. First, additional aspects of shape parameters that change in the vertical direction can also be simulated, such as in the case of doped nanoparticles [59] and the positional modulations of azobenzene chromophores [25]. Second, a dependence of optical stimulus can be investigated with respect to the decaying profile and polarization.

Figure 2.6.1(b) shows the ratio of curvature of the LCP sheets. For all computations, the absorbance rate model was assumed to be equal to the planar mesogen alignment. The clamped condition was imposed only at the center of the squared sheet. L_x and L_y were set to 10 mm, and h to 0.5 mm. Distinctive trends are found depending on the irradiation condition. For LPL irradiation, where the order at the midsurface is mainly diluted due to the increased number of cis- molecules, the ratio of curvatures converges around 2; roughly, such a value emerges when the bending momentum M_{xx} is about half of M_{yy} due incompressibility, and likewise for non-polarized light with planar distribution ($\mathbf{n_0}=(1,0,0)^T$). The convergence profiles, however, vary extremely as penetration depth changes; as shown in Fig. 2.6.1(a), the photoisomerization mainly occurs at the midplane for light penetration depth, while uniaxial contractions were evoked near the bottom for deeper penetration. Similar remarks apply to non-polarized light (NPL) irradiation, wherein the photomechanical behaviors are governed only by light decay, and the ratio converges around 0.5 for light penetration; uniaxial contraction dominates in this case. For higher penetration, on the other hand, the ratio converges to unity as light increases and mesogens isomerize uniformly, regardless of the thickness, which is analogous to the heated condition; although not reported herein, the heated condition produces exactly the same eigenstrain (κ_{xx}=κ_{yy}) as reported in Ref. [80]. It is worth to remark that thickness h is of critical importance in twisted configuration, in contrast to uniformly distributed mesogen, as Kirchhoff assumption is often violated in the LCP structure due to transverse shear resulting from strain compatibility [80].

2.6.2. Experiments on TN-LCP

As shown in the previous section, a LCP with twisted nematic configuration deforms into a non-conforming surface, while its curvature ratio between x- (lower surface alignment) and y- (upper surface alignment) curvatures differs depending on the temperature and light irradiation. Note that the saddle shape is apparently similar to the nematic case, although their origins are significantly differ; the transversely changing principal direction induces the saddle shape in TN, while Poisson effect is salient in the uniaxial nematic cases.

Such adaptivity to the stimuli has been underwent thorough investigations [13,21,28], as they are closely tied to the smart actuations. Moreover, the TN configuration is known to produce maximal saddle shape in which the weak spontaneous strain is induced onto the base [80], by which a TN solid is preferred over nematic as the amount of deformation is a prevailing issue in LCP-based applications.

Nevertheless, such anticlasticity is suppressed frequently, as the irregularities such as initial curvatures and the suppression of the curvature are imposed to the material [80]. The densely crosslinked LCPs (e.g. acrylate system [13, 26]), for instance, demonstrate a spring-like behavior regardless of the stimuli; the platelet upon synthesis, is initially curved and becomes upon strip (planar) or spring (twisted) depending on their orientational axis and the light stimuli. The imposed stimuli determine the pitch of a spiral and the spin axis: the material that sustains the load of ferromagnet therefore transports the magnet, possibly tune the magnetic field upon light bombardment [28]. Note that such finding suggests the one of bases of the present photomechanical consideration are violated: the equal distribution of the mesogen and its concomitant properties (e.g. mechanical stiffness).

In this regards, the present study investigate the effect of such violation to the photomechanics. The author firstly execute the experiment about light-induced motions of TN-LCPs, as there is no available literature that examine photomechanical behaviors with scrutiny. The results are then compared with the simulation results, by which an unknown parameter of photomechanics is extracted out. It is worth to remark that the present experiment emphasize the importance of interdisciplinary understanding to the light-responsive material.

2.6.2.1. Experimental setup

According to the definition, π/2-twisted nematic LCP indicates that the directionality is distorted locally in a way that directors found in the upper surface of the LCP is perpendicular to those found in the lower surface. Such distortion is induced by a strong surface anchoring between liquid crystal molecules and the rubbed polymer bonded onto the surface of the glass; the microgroove generated by the rubbing process forces the LC molecules aligned in the specific directions. The glass cell with microgrooves, as a mold, is generated through subsequent steps: cleaning, spin coating with Elvamide (*Dupont*), rubbing. The slides with perpendicular direction are evenly spaced by 20um, and fixated via photocuring in 365nm.

The constituents and their mixing ratio of the chemical compound is found in the

Table 2.6.1. RM82 and A3ZA3 are mesogenic material, where the latter one is light-sensitive; note that the large amount of the LCP is composed of light-inactive materials. The chiral-dopant [28] is incorporated herein, in order to impose consistent spin direction; without it, the linear gradient of the directors with random order in transverse direction are expected, as the perpendicular anchoring microgrooves generated onto the glass face are the only constraint imposed to the mesogens. The catalytic amount of Ingacure, a photocrosslinker, is also mixed.

The mixture is firstly heated to the melting temperature (110°C) and cooled down to the vicinal of nematic-isotropic temperature T_NI (80°C), in which the compound is injected to the glass cell. The photocrosslinking is then taken place Hg lamp (maker) for 2 hours to ensure that the material is fully crosslinked (see Fig. 2.6.2 (a)). The LCP is then peeled-off and cut in square shaped as shown in Fig. 2.6.2(b). It is worth noting that the initial curvature is not considered herein, as its effect is not severe when characteristic length of each nematic directions are similar, and when it is heated. The optical characterizations are also executed as shown in Fig. 2.6.2 (c-e), which ensures a nematicity the material is constructed as desired.

Linearly polarized light (LPL) is irradiated onto the heated (85°C) specimen with minimal ambient light (see Fig 2.6.3(a) for apparatus setup). Throughout the experiment, bending deformations with suppressed anticlasticity are observed, wherein the principal direction is determined by given polarized direction. An irradiation is persisted for 10 seconds and off for the thermal-induced restoration to flat geometry, before next irradiation with different polarized direction. The restoring duration is 30 sec when with fluorescent ambient light, or 2 minutes in dark condition. Throughout the experiment, the temperature is maintained. Since the image taken is inevitably skewed due to the UV laser location, a primitive image processing technique is utilized to extract a non-distorted image of the bending direction. Figure 2.6.3 (b) contains steps for the process, composed of capture, masking into binary image, and projective transform. The checkerboard pattern shown in the inset of the figure is employed as it is useful to extract out the projective transformation tensor with the aid of image processing toolbox™ implemented within the MATLAB.

The light irradiation intensity are vary in order to clarify the bending directions; the irradiated face during crosslinking (side A) demonstrates smaller curvature than the another face (side B), where the latter case often demonstrates the geometry-induced suppression of the curvature and thereby generates rolled geometry regardless of LPL, which renders the principal axis indiscernible. It is worth to note that the principal bending axis ψ is a valuable parameter throughout the present study, as they are invariant to the size of the photostrain and Poisson ratio that may ranges from 0 (i.e. suppression of perpendicular curvature) to 0.5 (i.e. incompressibility of the polymer)

2.6.2.2. Results and Discussions

Aforementioned violation of the equal distribution of the mesogens, which is driven by the mesogenic mass flux during photo-crosslinking, is presumed reason behind the initial curvature; unequal distribution of the molecule induces the gradient of the stiffness and strain, which in turn generates an initial curvature. In this respect, it is desired to elucidate its possible effect to the photomechanics, which can be summarized into two exclusive possibilities in terms of light absorption: 1. a different in-plane strain gradient evolves in transverse directions; 2. only the amounts of photostrain are differ, while the gradients are retained. The latter postulation is closely related to the order-coupled constitutive relation (Eq. 2.3.3), where the modulus change and stress is only dependent to the change of r; hence the gradient of the strain within the material is largely untouched, and mostly governed by the penetration profile of the light. Note that the number of light-sensitive molecules herein is relatively small, so it is natural to assume their effect to the light profile is negligible.

Firstly, we compute the characteristic depth for light penetration, by given principal bending direction for each LPL condition. We assume a simple Beer's light decay model as shown in Eq. 2.6.2, where a z is a transverse coordinate, h is a thickness of the material, and d is a penetration depth. Note that the decaying property is derived by scaled value d/h, regardless of the light-intensity in contrary to Lambert-

W model. Nematic configuration in transverse direction is assumed to be linear $\pi/2$-twisted. The absorption of the light by mesogens at each layer is modeled by simple Beer's law.

Figure 2.6.4 illustrates principal bending axis ψ with respect to LPL direction, which are compared with the calculated axes with various penetration conditions. ψ. A large map of ψ with given LPL direction and logarithmic scaled penetration depth is illustrated by Fig. 2.6.4(a), where the non-monotonicity are found with increasing d. The side A's experimental data about ψ is used for comparison, where the min-max gap of ψ is utilized as a scalar criterion. As shown in Fig. 2.6.4(b), two values of d_1 and d_2 are found to be coinciding with the given gap, while a calculation based on d_1 reproduces consistent profile as shown in the inset.

In summary, the changes of ψ for given LPL, and the penetration depths are tabulated within the Table 6.2.2. Although the mesogenic densities of each face are greatly differ as demonstrated by face-dependent bending behavior, their penetration depth remains largely unchanged; hence the light profile is proven to be similar. Through the finding, it is possible to suggest that the photomechanical behavior of TN is attained, given that the weight percent of light-reactive mesogen remains small compared to the inactive constituents.

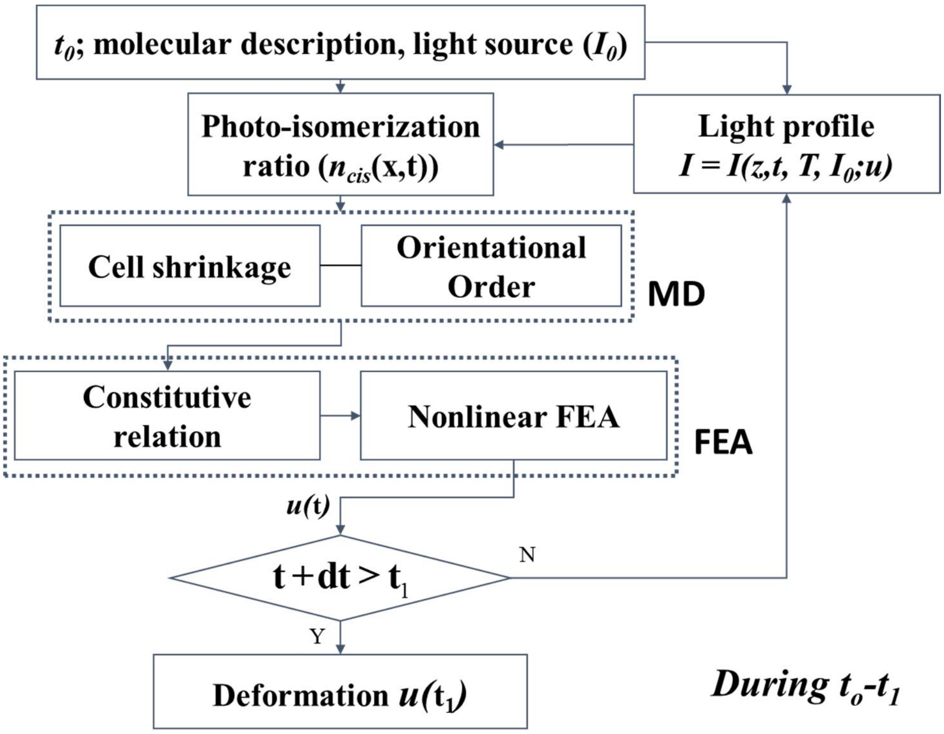
t_0; molecular description, light source (I_0)
Photo-isomerization ratio (n_{cis}(x,t))
Light profile $I = I(z,t, T, I_0;u)$
Cell shrinkage
Orientational Order
MD
Constitutive relation
Nonlinear FEA
FEA
u(t)
t+dt > t_1
N
Y
Deformation $u(t_1)$
During t_o-t_1

FIG. 2.1.1. Multiscale schematics. A photoisomerization ratio at time *t* is computed for a given light intensity I_o and temperature *T*; it is then used for molecular dynamics (MD) simulations, which provide microscopic information to the nonlinear finite element analysis (FEA).

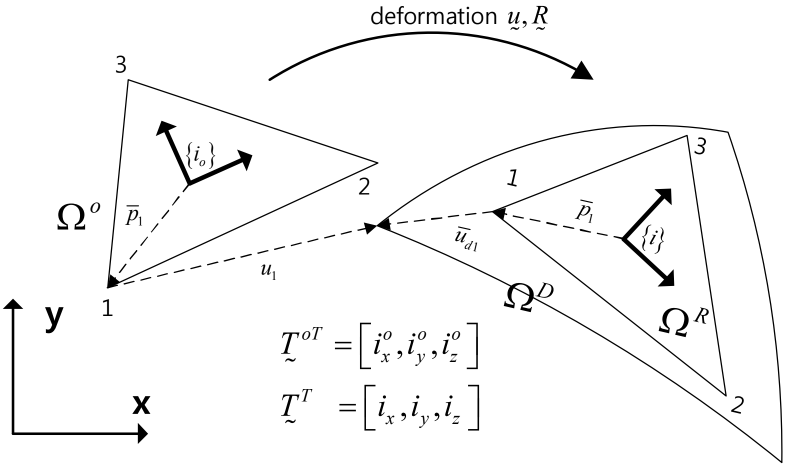
deformation $\underset{\sim}{u}, \underset{\sim}{R}$
3
$\{i_o\}$
2
Ω^o
$\bar{p}_1$
u_1
1
y
x
$\underset{\sim}{T}^{oT} = [i_x^o, i_y^o, i_z^o]$
$\underset{\sim}{T}^{T} = [i_x, i_y, i_z]$
1
3
$\bar{p}_1$
$\bar{u}_{d1}$
$\{i\}$
Ω^D
Ω^R
2

FIG. 2.2.1. Kinematics of EICR.

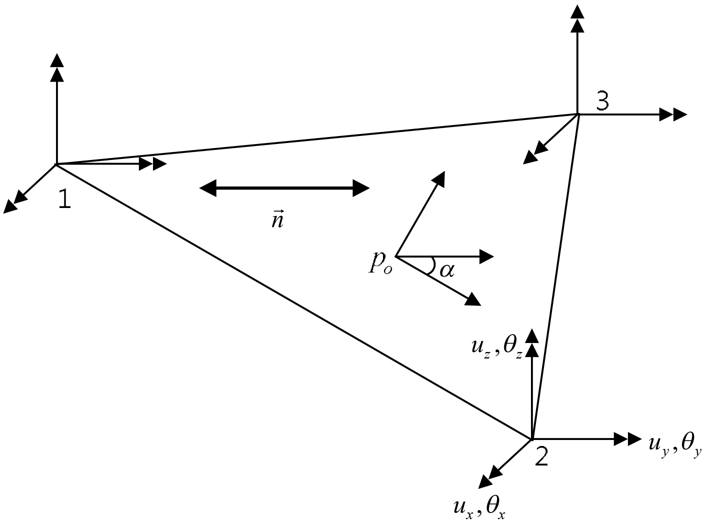
3
1
$\vec{n}$
p_o
α
u_z, θ_z
2
u_y, θ_y
u_x, θ_x

FIG. 2.2.2. Three-node shell formulation with 18 DOF and nematic orientation.

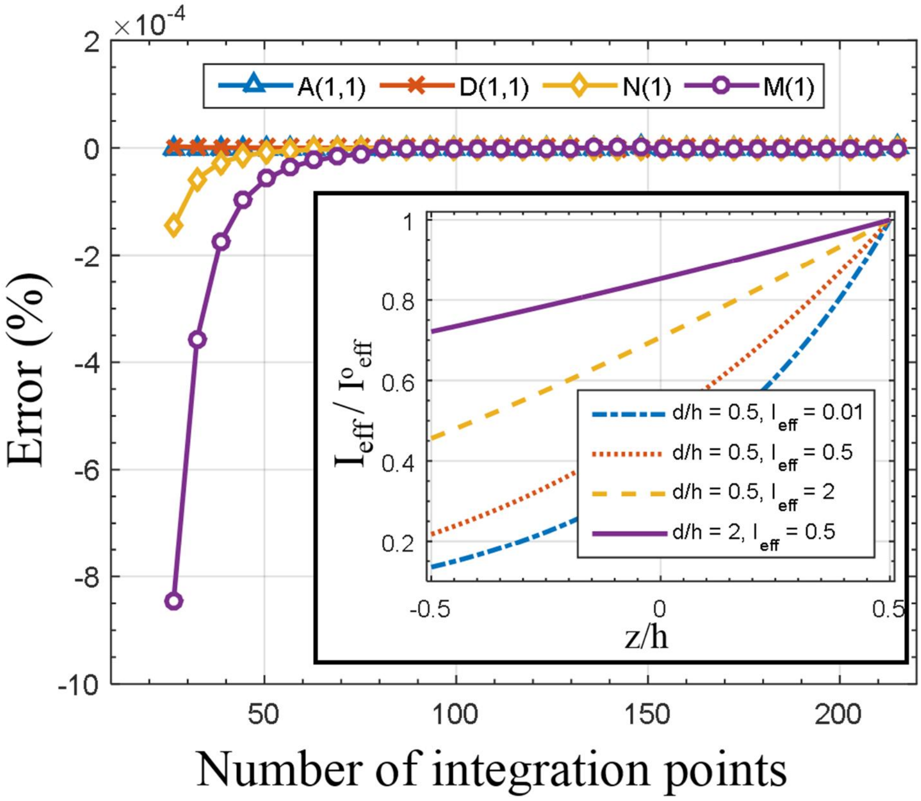

FIG. 2.2.3. The effect of the number of integration points within thickness on the numerical integration for mid-plane properties of nematic solids. Inset: properties of light decay for various values of penetration depth and intensity.

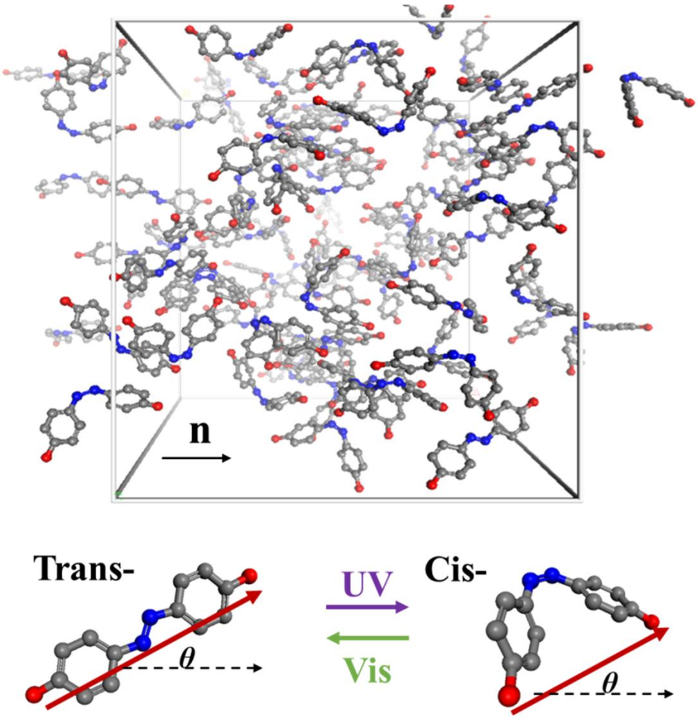

FIG. 2.3.1. Unit cell of a photo-responsive polymer network (LCP) with *cis*-population $n_{\text{cis}} = 0.25$ (flexible hydrocarbon networks are removed for readability) and *trans*- and *cis*- state molecules with angular deviation (θ) from the nematic director ($\vec{n}$).

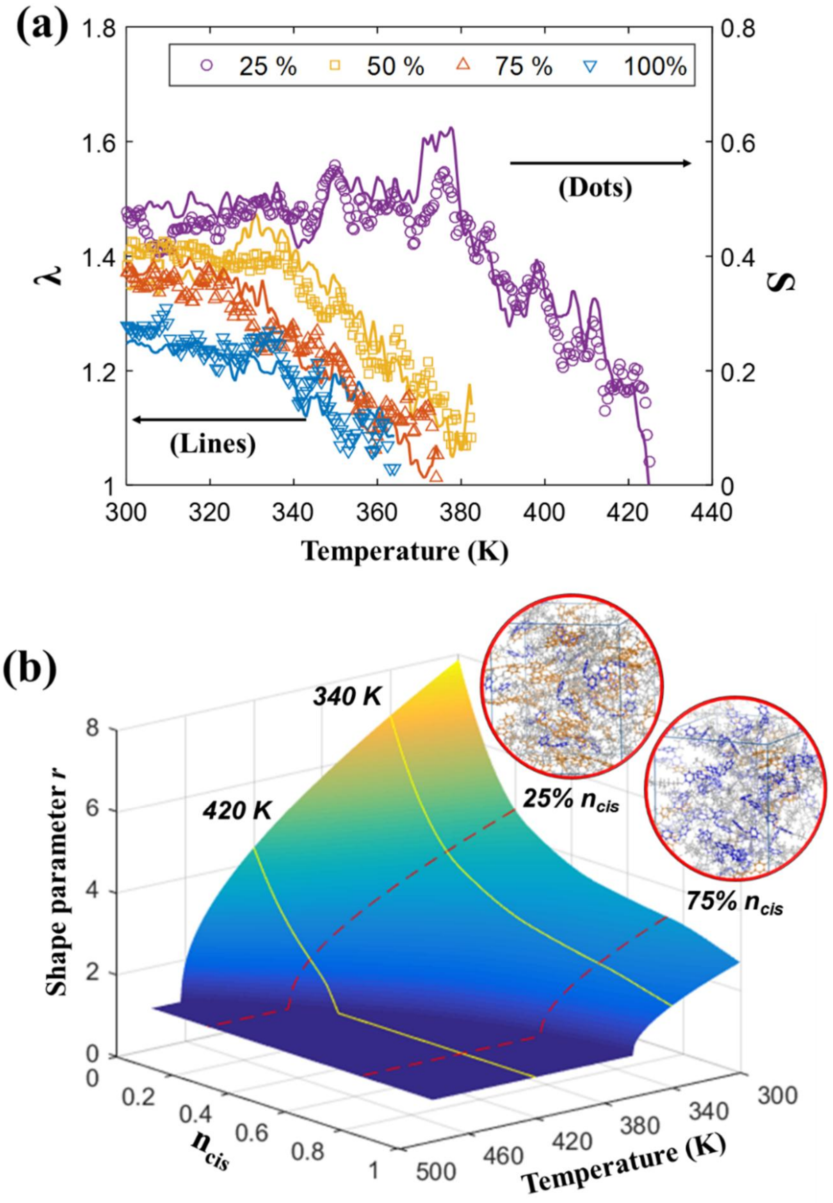

FIG. 2.3.2. Time-dependent bending deformation of photo-responsive polymer networks (LCPs). (a) Tip deflections compared with various light intensities I/I_{ref}, wherein nonlinearities such as bending-unbending behavior [42] are found. (b) Characteristic time required to obtain specific deflections (h*) with different operating temperatures, wherein the thermal relaxation effect with the photo-bleaching effect is demonstrated. (h represents the thickness of the strip.)

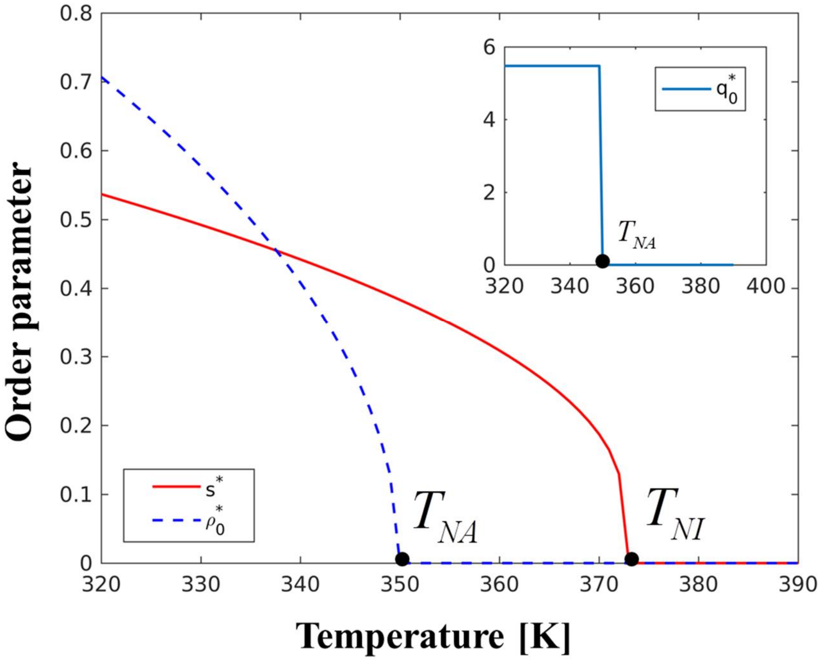

FIG. 2.3.3. Order parameter s^*, ρ_o^*, q_0^* with increasing temperature; 1st order phase transition is observed due to assumed Landau form of free energy.

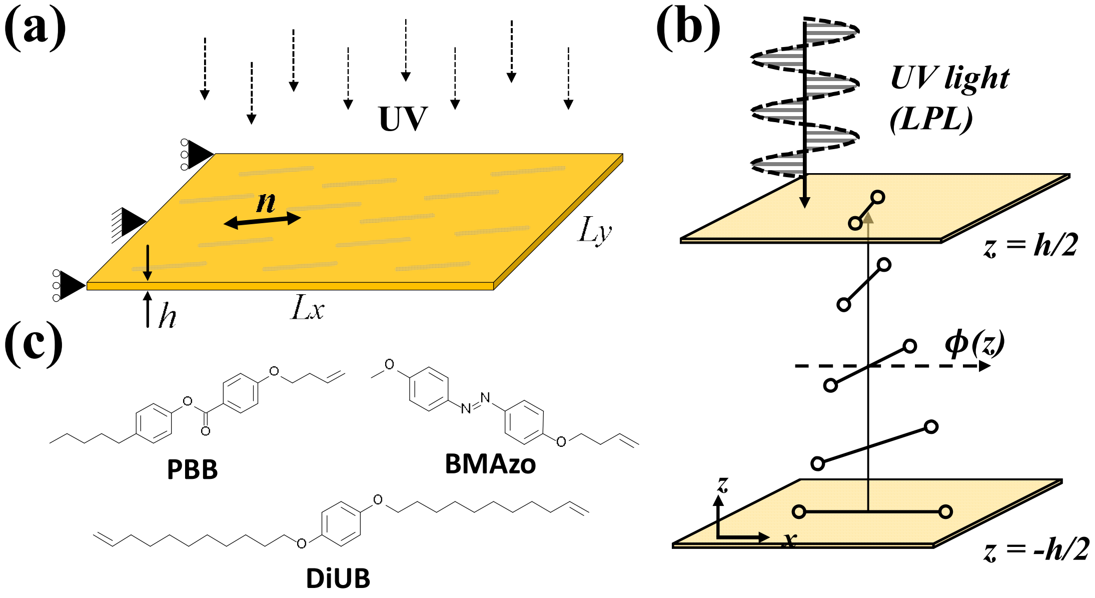
(a)
UV
n
Ly
h
Lx
(b)
UV light
(LPL)
z = h/2
ϕ(z)
z
x
z = -h/2
(c)
PBB
BMAzo
DiUB

FIG. 2.4.1. LCP model configurations. (a) Model geometry with length, thickness, and mesogenic director ***n***. (b) Depthwise angle *f* between LPL and the director. (c) Structural formula of molecules used herein (components of Azo18 [54]).

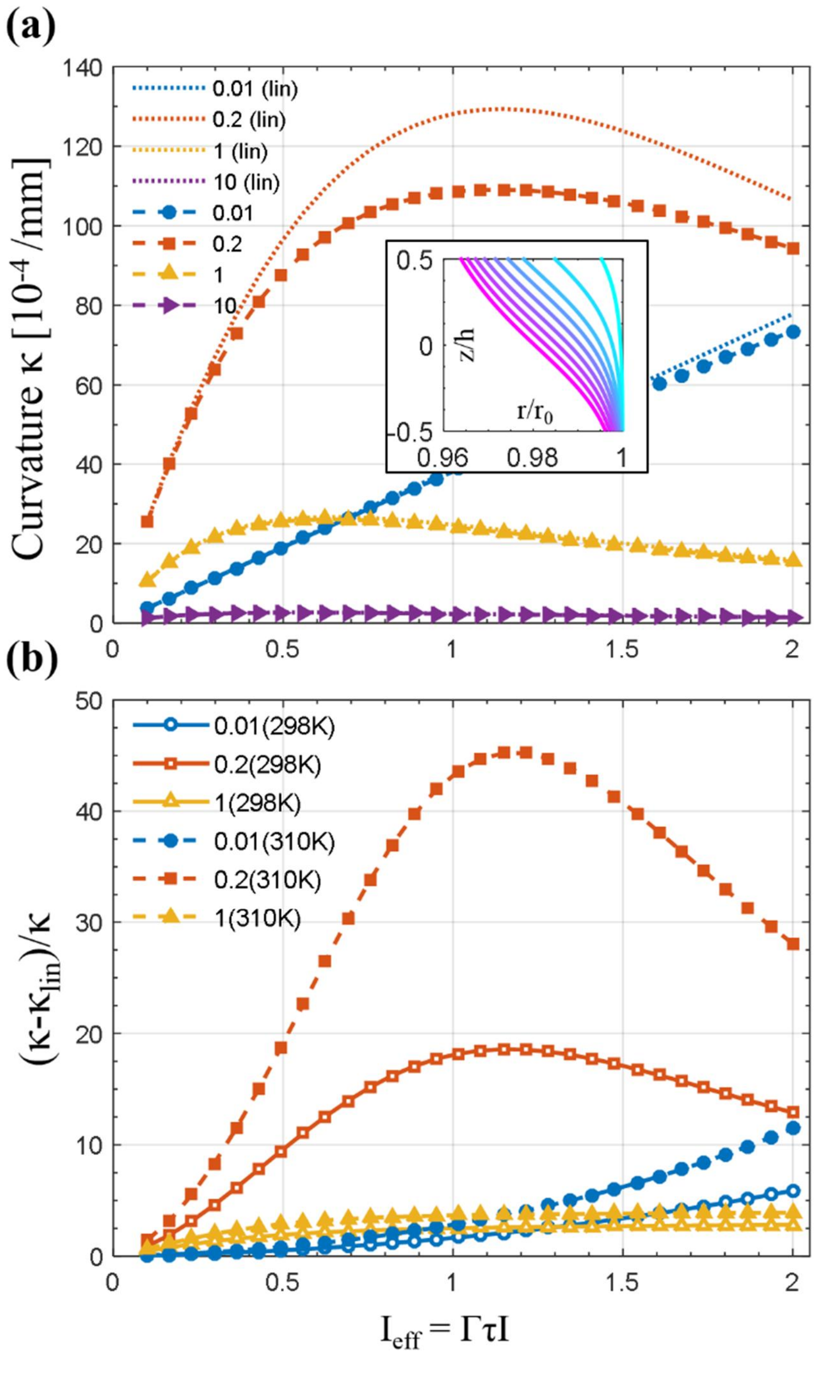

FIG. 2.4.2. Curvature of the cantilevered LCP (***n***//***x***, h = 0.5 mm, L_x = 10 mm, L_y = 1 mm) for various penetration depths d. Inset: changing profile of normalized shape parameter r/r_o (y-axis) with weaker (bluish) and stronger (reddish) light.

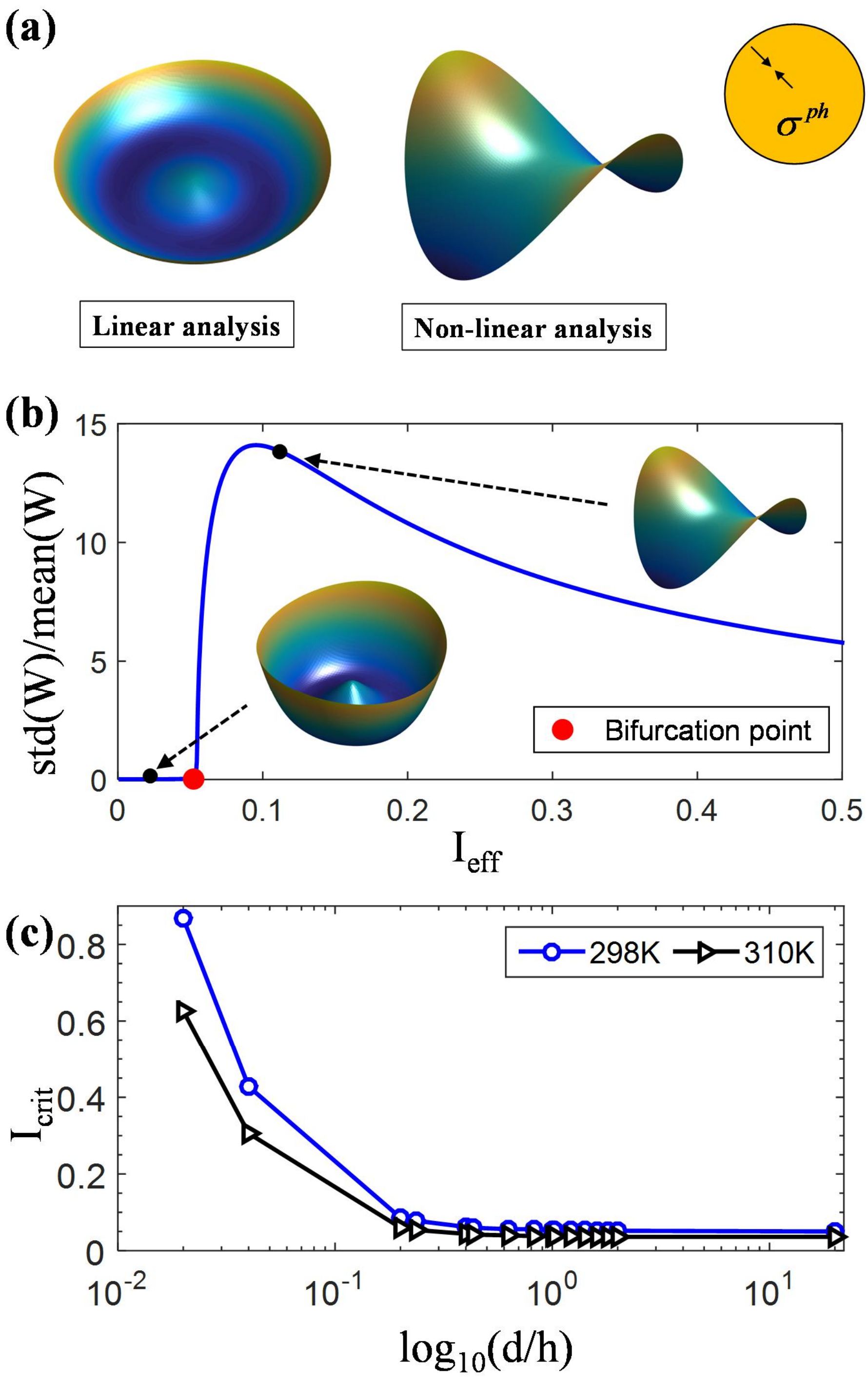

FIG. 2.4.3. Shape change of LCP sheet with radial disclination-defect-induced instability. (a) Linear vs. nonlinear solution. (b) Instability onset. (c) Trends of critical intensity (I_{crit}) at the bifurcation point.

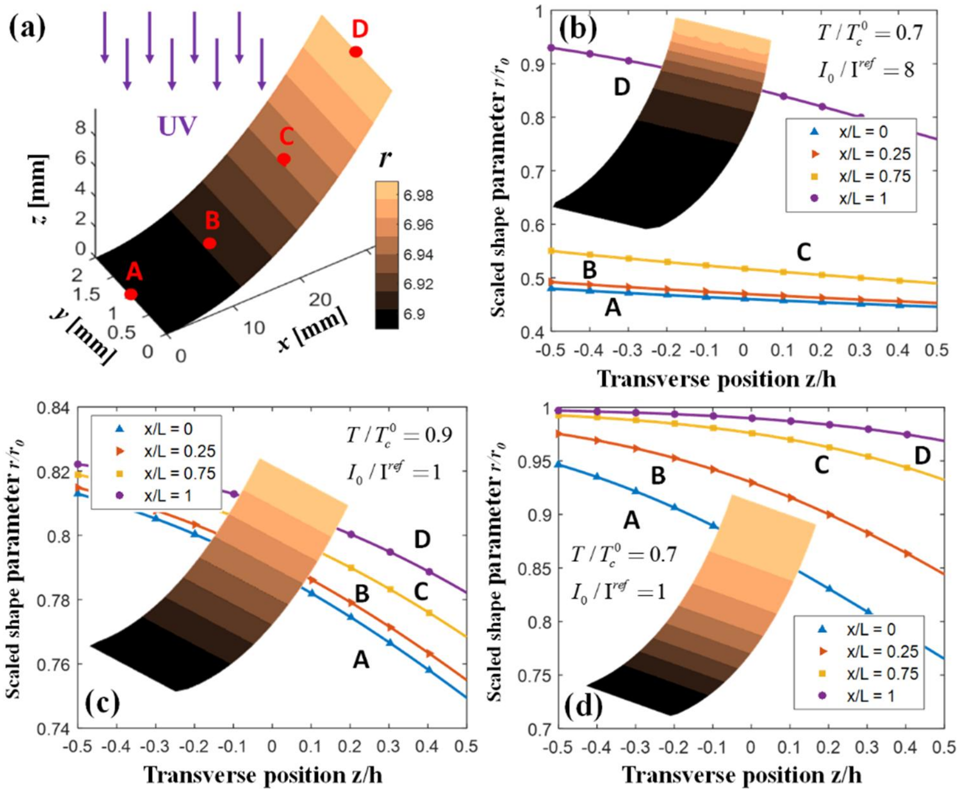

FIG. 2.4.4. Photo-responsive LCP bending induced by light travelling in the –z direction. Coloring indicates the shape parameter r of the upper surface. For equally spaced positions (i.e. A, B, C, and D), the transverse position vs. normalized shape parameters of different intensities (I_o / I^{ref}) and temperatures (T / T_c^o) is plotted. (h represents the thickness of the strip.)

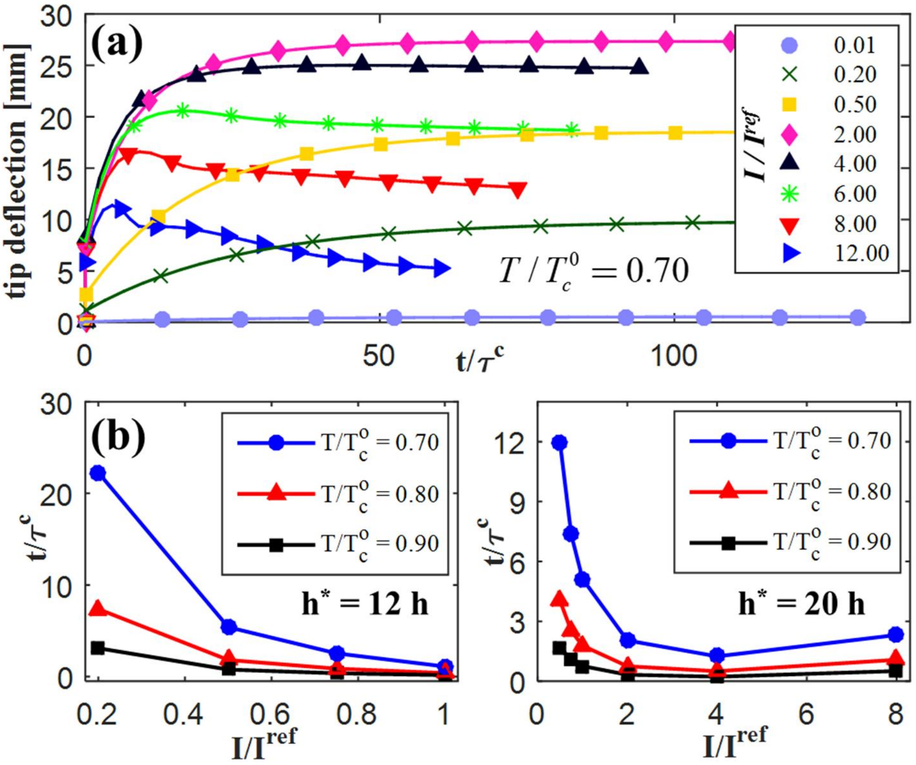

FIG. 2.4.5. Time-dependent bending deformation of photo-responsive LCP (a) Tip deflections compared with various light intensities *I/Iref*, wherein nonlinearities such as bending-unbending behavior [42] are found. (b) Characteristic time required to obtain specific deflections (h*) with different operating temperatures, wherein the thermal relaxation effect with the photo-bleaching effect is demonstrated. (h represents the thickness of the strip.)

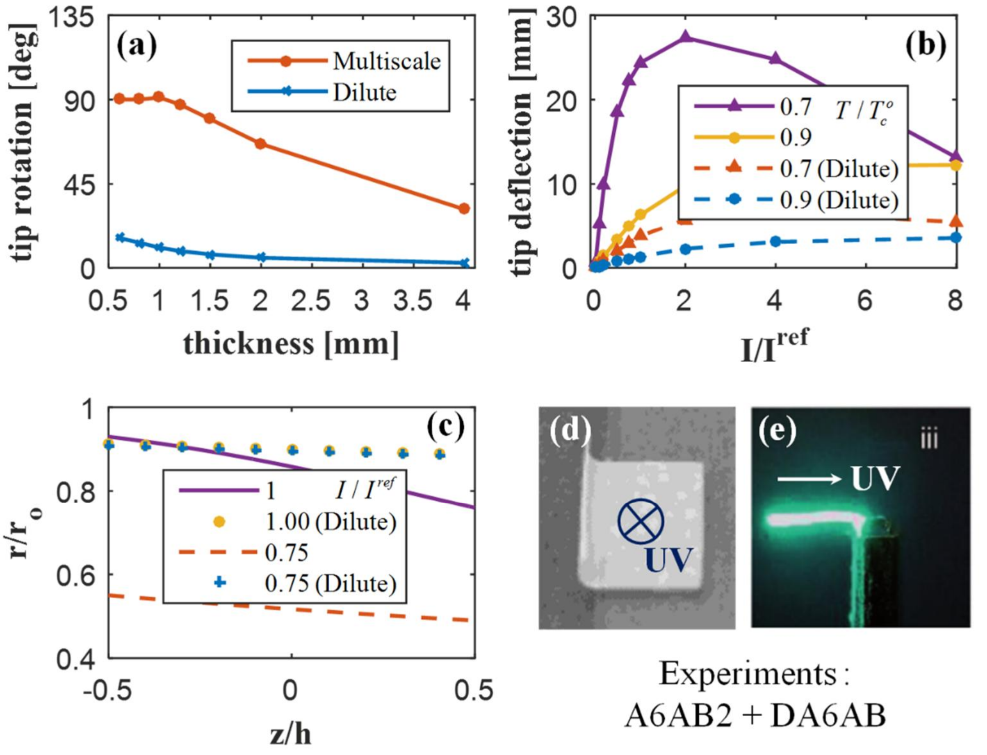

FIG. 2.4.6. Bending deformation of photo-responsive polymer network (LCP) computed via multiscale framework compared to the classical dilute model suggested by Hogan et al.[39] Substantial differences are found in both (a) tip rotations and (b) tip deflections with various values of T / T_c^o. (c) With different light intensities, thickness gradients of the shape parameter r / r_o of the multiscale model (lines) are compared to those of the classical model (dots) in order to explain these differences. A 90º tip rotation is commonly observed in experiments of side-chain acrylate LCPs whenever irradiated (d) from above or (e) from the left. Figure (d) is adapted with permission from Yu *et al.*[11] (DOI: 10.1021/cm035092g). Copyright 2004 American Chemical Society. Figure (e) is adapted from White *et al.*[14] (DOI: 10.1039/B805434G) with permission of Royal Society of Chemistry.

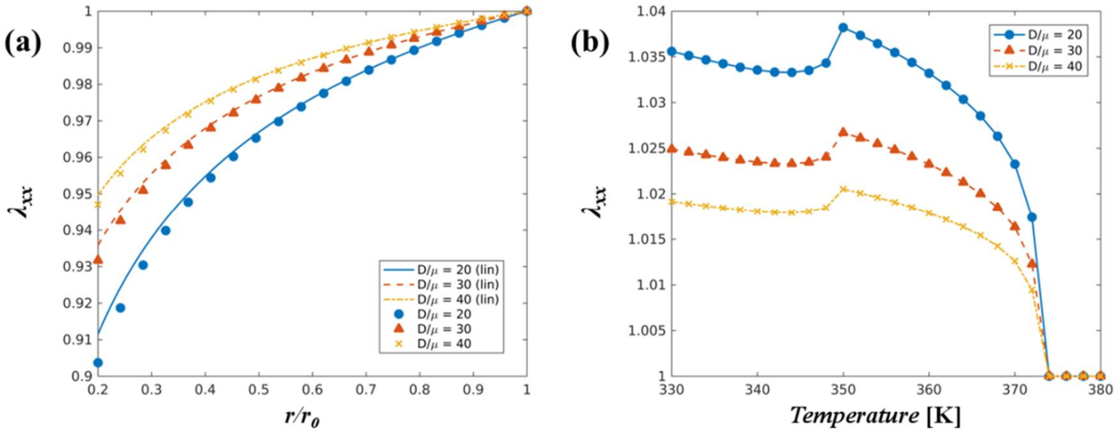

FIG. 2.5.1. Uniaxial shrinkage due to phase change of the smectic solids with different layer modulus D (a) length change vs. changing shape parameter *r* (b) length change vs. operating temperature. Non-monotonic shrinkage is observed, as shown in the experiment [42, 74].

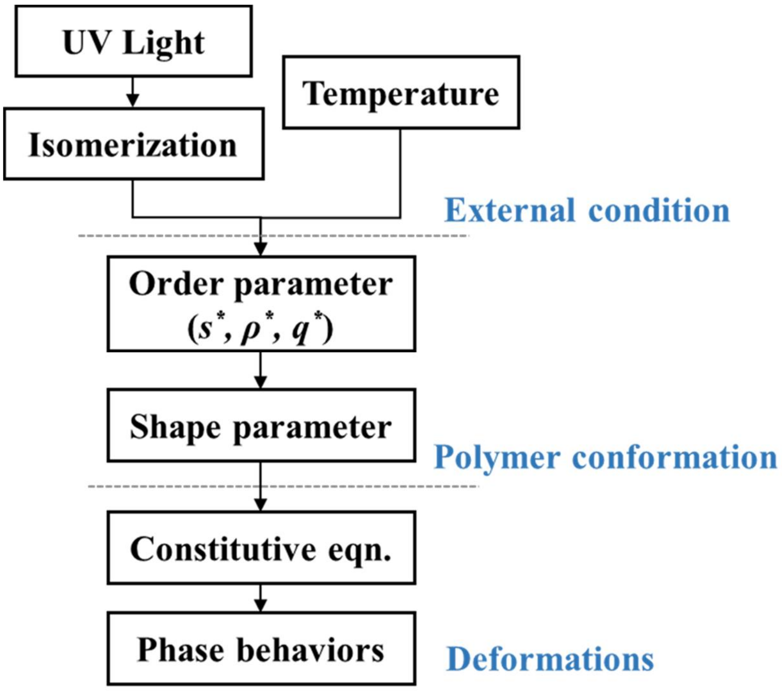
UV Light
Isomerization
Temperature
External condition
Order parameter
(s^*, ρ^*, q^*)
Shape parameter
Polymer conformation
Constitutive eqn.
Phase behaviors
Deformations

FIG. 2.5.2. Flowchart of the photomechanical analysis on smectic solids, which is a combination of microscopic polymeric conformation and finite element analysis (marked by deformations).

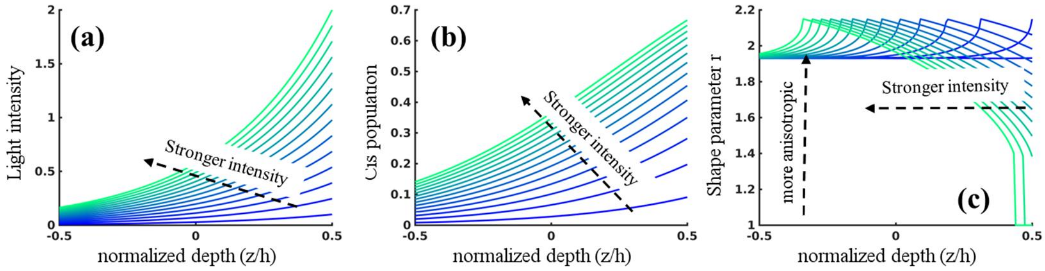

FIG. 2.5.3. Profile of light-induced derivatives in out-of-plane direction. (a) Decay of the light intensity depending on Beer's law (b) steady-state *cis*- population n_{cis} , (c) shape parameter *r*, wherein monotonicity is observed.

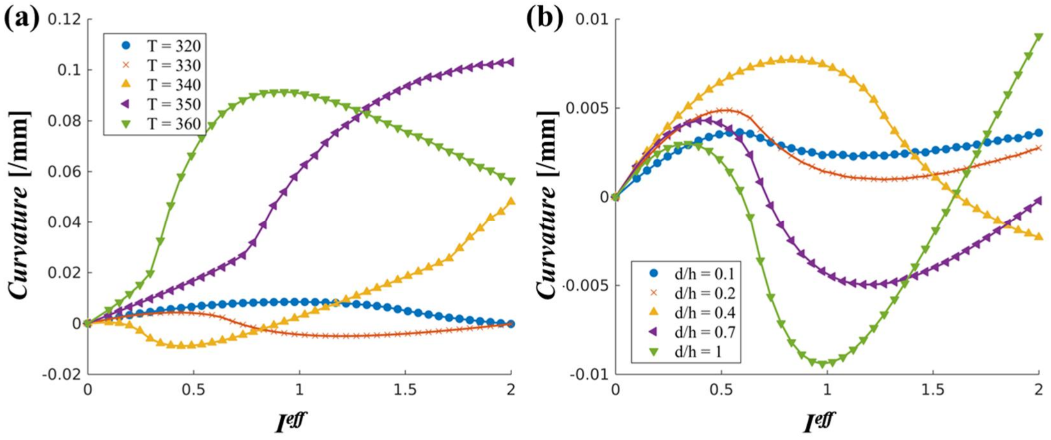

FIG. 2.5.4. Temperature dependence of photo-responsive behavior with increasing light intensity in terms of curvature. (a) Temperature variation with fixed penetration depth (*d/h* = 0.4) and (b) variation of penetration depth *d* with fixed temperature (*T* = 330K) .

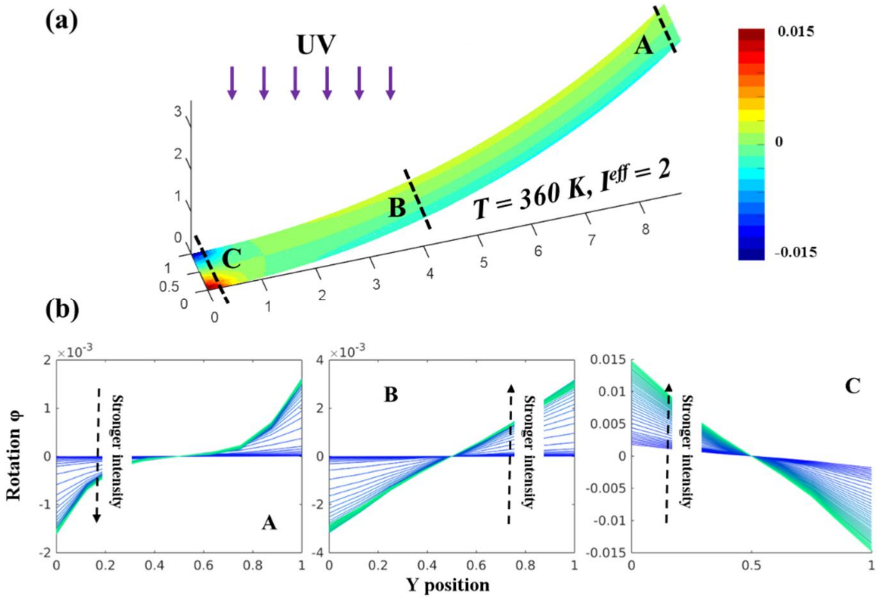

FIG. 2.5.5. (a) Deformed profile and the local rotation ϕ of the smectic solid with given stimuli (T = 360 K, I^{eff} = 2) and (b) profile of the rotation with increasing light intensity and greater nonlinearity.

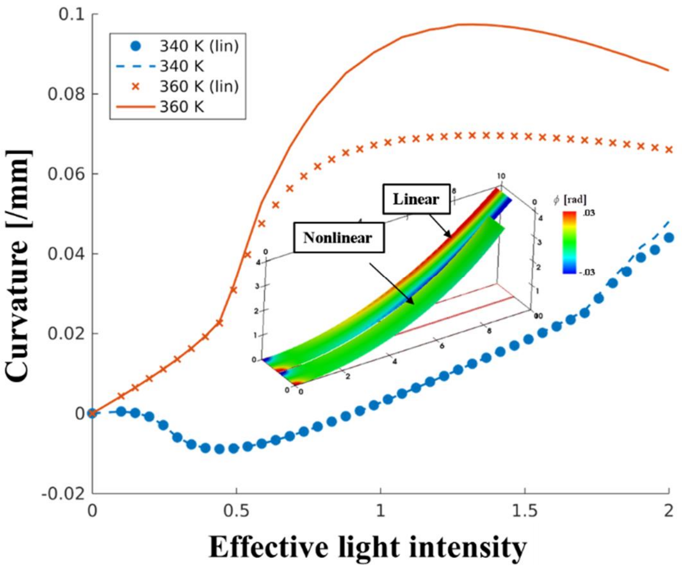

FIG. 2.5.6. Effect of nonlinearity depending on the temperature and intensity (inset) of the bent geometry of the smectic solid, where the rotation ϕ is marked by the color on the surface. The overestimation of the curvature and rotation is observed when nonlinearity is not taken into account.

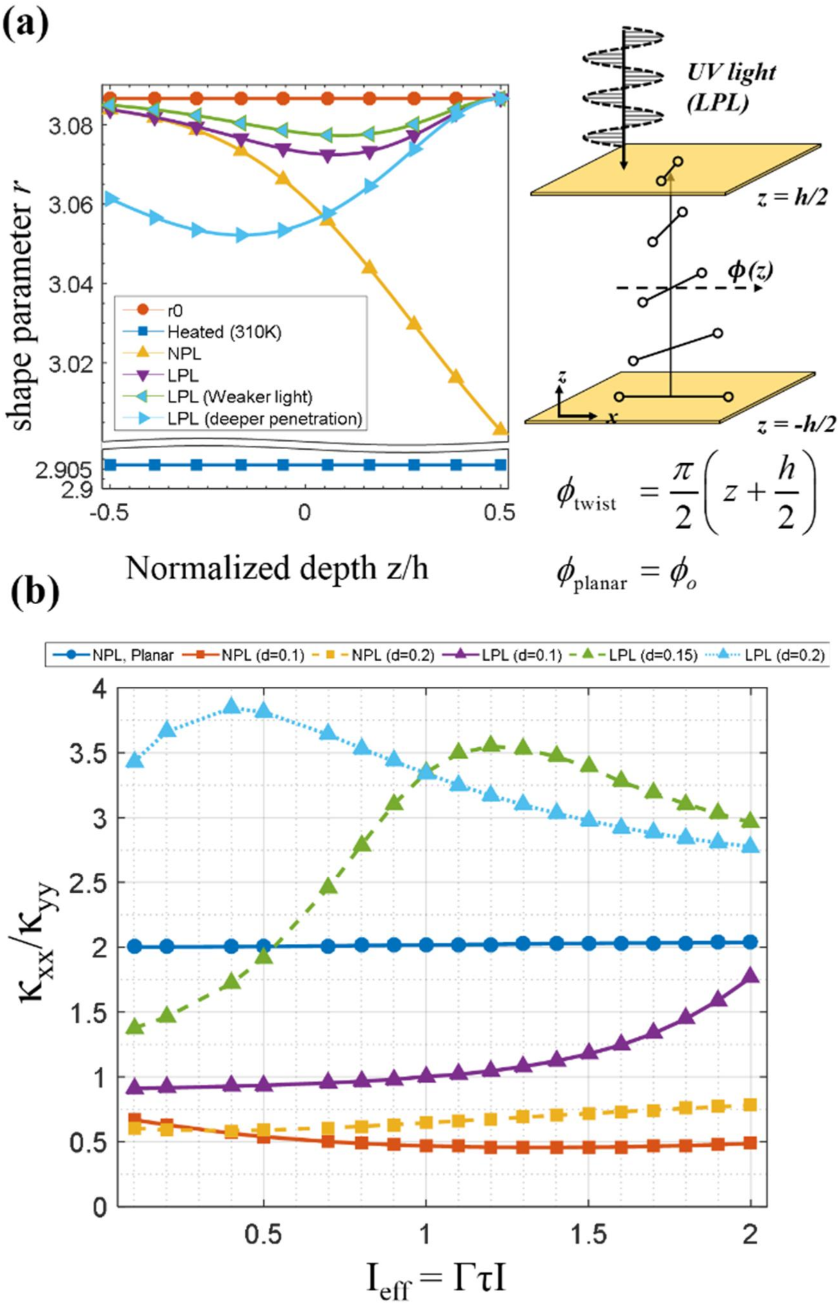

FIG. 2.6.1. (a) Evolution of shape parameter of twisted configuration depending on external stimuli (NPL: non-polarized light; LPL: linearly polarized light in the *x*-direction). (b) Ratio of principal curvatures with various external stimuli and penetration depths.

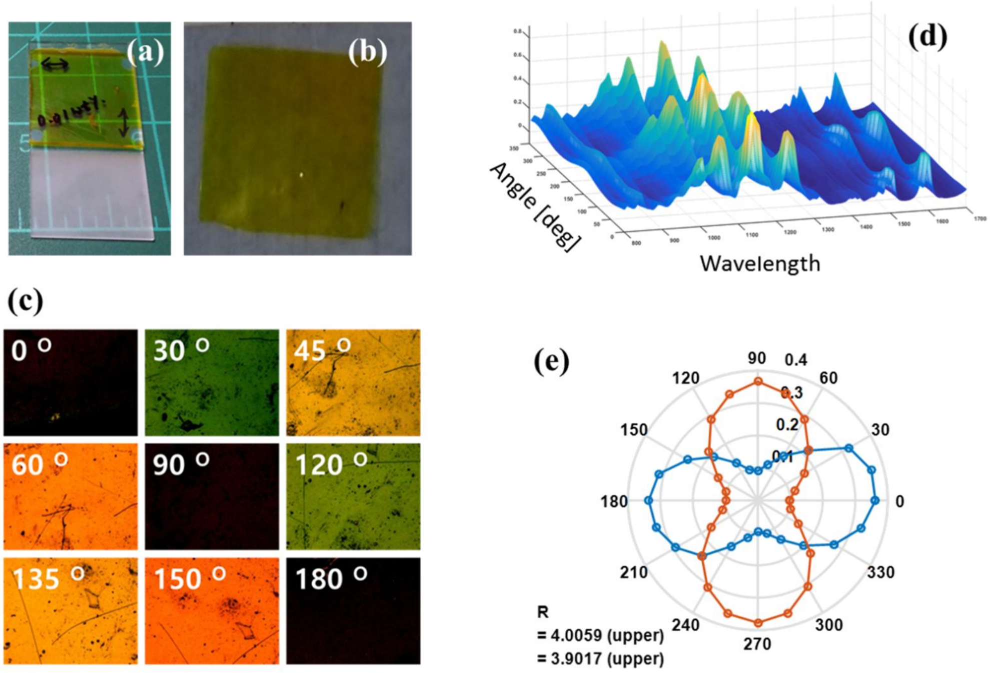

FIG. 2.6.2. (a) glass cell with injected compound (b) a TN-LCP after peel-out (c) a rotation-induced changing color of polarized optical microscopy (d) raw data of FTIR data (e) an alignments of Kuhn segment obtained by FTIR (ATR) data. Dataset of upper surface and the lower surface are marked orange and blue, respectively.

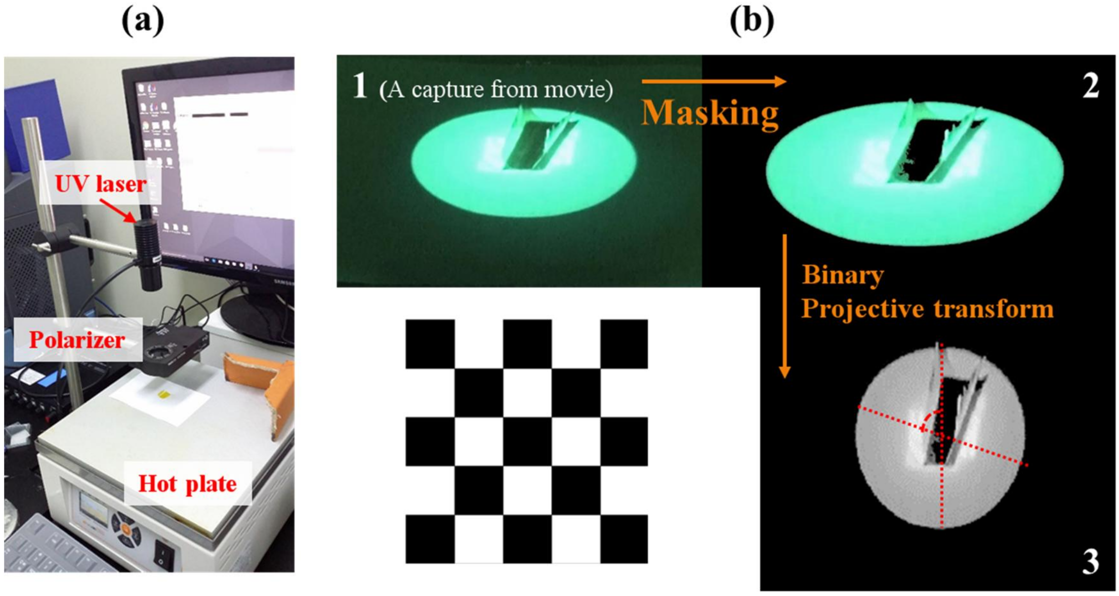
(a)
(b)
UV laser
Polarizer
Hot plate
1 (A capture from movie)
Masking
2
Binary
Projective transform
3

FIG. 2.6.3. (a) setup for light-exposure to the specimen (b) a sequence of image processing with the aid of MATLAB image processing toolbox™ (inset) checkerboard pattern to compute projective transformation tensor

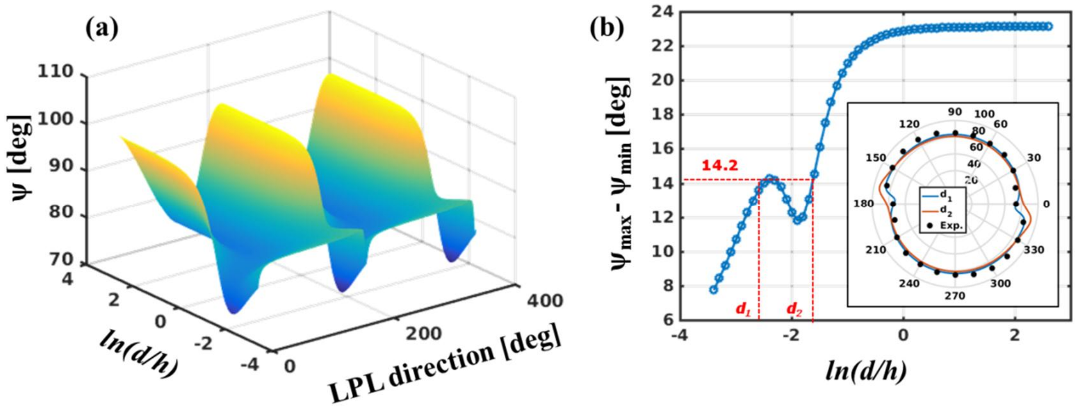

FIG. 2.6.4. (a) a principal bending axis ψ with given LPL direction and logarithmic penetration depth d (b) a min-max gap of ψ with logarithmic penetration depth; when compared with the experiment (ψ_{max} - ψ_{min} = 14.2), two possible penetration depth (d_1 , d_2) is found (inset) polar plots of ψ vs. LPL direction for d_1, d_2 with experimental values.

TABLE 2.1.1 Pseudocode of the present multiscale schematic

```
SETUP          molecular configuration, mesh (node, elem), $I_0$, $T$
INITIALIZE     $t = t_0$, $u = 0$, $n_{cis} = 0$
FOR (t = 0; t < t1; t += dt)
    FOR every Element
        FOR every Gauss point
            COMPUTE    $I = I(z,u,I_0)$
            COMPUTE    $n_{cis} = \dot{n}_{cis}dt = \{\eta I(1-n_{cis}) - \tau_c^{-1} n_{cis}\} dt$
            IMPORT     $r(n_{cis},T)$                from molecular dynamics
            COMPUTE    $\sigma(r,u), C(r,u)$         from constitutive equation
        END FOR
        COMPUTE    $[\underline{\underline{A}},\underline{\underline{B}},\underline{\underline{D}}],\{\underline{N}^{ph},\underline{M}^{ph}\}$    from Simpson's rule
    END FOR
    ASSEMBLE   $\mathbf{K}(u,I), \mathbf{R}(u,I)$    from Corotational formulation
    UPDATE     $u = u + du$
END FOR
POST-PROCESS  $u, \sigma$
```

TABLE 2.1.2 Simulation parameters; μ is the shear modulus.

Value [Units]		Value [Units]	
ηI^{ref} , τ_o	0.01, 25.3 [s^{-1}]	$Lx \times Ly \times h$	36 × 4 × 0.5 [mm]
Δ	4 x 10^{-20} [J]	d/h	0.4
μ [35]	1.5 [GPa]	I / I^{ref}	0.1–15
T_o / T_o^c	0.70	T / T_c^o	0.70, 0.80, 0.90

TABLE 2.3.1. Molecular dynamics (MD)-based microstate parameters. Standard deviation (S.D.) is calculated for cells with different locations of *cis*- molecules. References include thermodynamic properties from the acrylate side-chain [11] and elastomer-based nematic polymer [54].

n_{cis}	T_c [K] (S.D.)	α (S.D.)	ζ (S.D.)
0.00	462.50	1.40	0.33
0.25	425.17 (33.32)	1.00 (0.10)	0.37 (0.03)
0.51	392.50 (9.70)	0.92 (0.25)	0.39 (0.06)
0.75	373.70 (7.52)	0.91 (0.33)	0.40 (0.13)
1.00	363.01	0.90	0.40
0 [11]	443.15	N.A.	N.A.
0 [54]	340.15	0.51	0.19

TABLE 2.3.2 Constitutive parameters for Landau-formulation for phase transition

Parameter	**Value**	**Parameter**	**Value**
a_o	1	b_2	100
b	100	$\tilde{c}$	3000
c	400	T^*	370
$\hat{a} = \hat{b}$	400	T_{NA}	350

TABLE 2.6.1. A mixing ratio of TN-LCP compound

RM82 (Mesogen)	87.9 wt%
A3ZA3 (azo-derivative)	10 wt%
Photo-initiator (Ingacure)	2 wt%
Chiral-dopant (R1011)	0.1 wt%

Table 6.2.2. Principal bending axis ψ for each face and LPL: significant digits are 2 and 3, for ψ and *d/h* respectively.

LPL [deg]	ψ (sideA) [deg]	ψ (sideB) [deg]
0	75.74	76.5
15	75.4	78.44
30	80.56	79.17
45	83.45	80.32
60	83.45	81.27
75	85.01	82.39
90	84.95	84.05
105	87.34	84.14
120	89.35	87.51
135	88.78	88.8
150	87.29	84.43
165	85.25	81.52
180	75.05	80.74
d/h	0.103	0.137

Chapter 3. Designs of LCP actuation

Having discussed the onset of bending and the nonlinear considerations in preceding chapter, the effects originated from the design parameters to the behavior of light-responsive LCP sheets are presented, both of which retains either nematic or smectic phase. This is on the same line of idea of the designing LCP-based actuation systems invented recently. Unlike other active materials based on a bi-phasic transition that exert uniaxial length change (e.g. shape memory alloy), the behavior of the light-responsive LCP can be tuned on both pre-synthesis and post-synthesis steps. Throughout the present thesis, a pre-synthesis step refers an alternation of the liquid crystal alignment before its crosslinking and peeling out from the cell, where induced microscale changes can be observed only by microscopic measurements such as polarized optical microscopy (POM). On the other hand, a post-synthesis step refers a change that can be seen by bare eye: the shape of the specimen, and the way of cutting that comes before peeling are the examples of the category.

It is worth to remark that the both results evidence the enhanced simulation capability of the present work, showing that it is suitable for photomechanical discussions about generic PRP deformation and design of the applications such as actuators and self-folding materials. Most of all, it does not require designed eigenstrain as in the micromechanics-based study [17, 18, 82], which cannot account for the effect of a changing shape parameter that interacts with the decaying profile of light, and quasi-rotation of the local order of mesogens.

3.1. Changes of extrinsic variables: geometry and orientation

Following typical methods, a LCP fabrication involves an alignment technique; by attaching two glass plates rubbed in parallel directions, a uniform alignment is generated along the prescribed mesogenic director. The extrinsic variable dealt herein indicates the variation imposed in post-crosslinking step, where the mono-axiality of the director remains intact. The angular deviation between nematic director and longitudinal direction of LCP strip, and the shape of the specimen are investigated in this section. A distribution of the light irradiation to obtain desired deviation is also computed based on the light-to-photo strain relationship elucidated in the previous photomechanical description.

3.1.1. Directional orientations of nematic LCP

The directed bending driven by in-plane rotation of the globally uniform director is shown in Fig. 3.1.1. Such configuration is classically fabricated by cutting the specimen out in the non-parallel direction to the monodomain alignment, which alters the principal bending direction. The light is assumed to be non-polarized without losing generality, and the angle j_o is defined as the difference between the x direction and the local orientation **n**. It is clearly seen that maximal tip deflection monotonically decreases as j_o increases from 0° to 90°.

Three different light penetration depths are displayed, all of which show a similar trend as torsional deformation replaces bending while their maximal displacement varies. In all cases, the vertical tip deflection becomes zero when the directional difference increases to 60°, after which the sheet starts to bend away from the light. These results agree well with the experimental results obtained for glassy polymers with various director orientations [70].

The point at which zero-vertical displacement emerges is another indicator of the nonlinearity need of the 3D shell model compared with the 2D confined model. When j_o is not 0° or 90°, in-plane shear N_{12}^{ph} and torsion M_{12}^{ph} resultants become nonzero by rotation of the principal direction. As a result, the effects of shear and torsion become profound and the tip is moved upward to compensate for the driving momentum. Consequently, this in-plane phenomenon attenuates the occurrence of zero tip deflection, and this behavior becomes more profound in the co-rotational formulation because geometrically driven rigid-body rotation between Ω^o and

Ω^R is added to pure element rotation $\bar{\theta}_z$. In conclusion, the orientation effect results show that n_o is not only an important design parameter of actuation exhibited by LCP materials, but is also an effective measure for demonstrating the need for the present framework.

3.1.2. Directional orientations of smectic solids

Even though smectic solids retain one more symmetry in rubbed direction), their uniaxial configuration is assumed to be maintained; hence a directional orientation is similarly defined.

Conversely, the director change specified in the pre-synthesis state also produces prominent changes in deflection. As an anisotropic material, the longitudinal axis of the specimen may not necessarily be coaxial to the layer normal; such deviation, for example, is possibly created by cutting out the specimen that is in a nonparallel direction to the rubbing direction (i.e. monodomain direction). The change of principal bending behavior is demonstrated in Fig. 3.1.2.

where θ indicates the prescribed angle difference between the layer normal $\vec{n}_o$ and a longitudinal axis (i.e. $\vec{n}_o = \{\cos\theta, \sin\theta\}^T$). The magnitude of deflection is strongly alternated when θ changes from 0 to $\pi/2$, whereby the principal bending direction is rotated and thus bending-twisting coupling is generated. As discussed in Fig. 3.1.2, a deflection generally increases proportional to *d*, while the direction of deflection is determined by light intensity when the operating temperature is selected within a range that provokes the pre-transitional effect. It is worth noting that such finding is analogous to the experimental results [74] and steady-state solution [5] of nematic solids, although the point where zero-deflection (i.e. purely twisting deformation) differs due to the non-monotonic profile of the shape parameter. The present findings suggest that the direction of cutting is an efficient design parameter to determine the mode of deflection, and the meticulous selection of temperature and light intensity is critical.

3.1.3. Anticlastic behavior of nematic LCP

A nonzero Gaussian curvature developed by the illumination of a non-square LCP is shown in Fig. 3.1.3(a). An initially flat, ellipsoidal sheet with $R_{x,}$, R_y as its principal radii is examined herein. The nematic director is assumed to be aligned in the x direction without losing generality. I set the thickness h to 0.5 mm and the penetration depth d to 0.2 mm, which correspond to maximal deflection in LCP cantilever and are significantly smaller than the fixed value of the LCP sheet's longitudinal radius $R_x =$ 20 mm. The curvatures on the surface and local principal axes are computed via the least-square fitting of the surface composed of local neighboring vertices to a quadratic patch.

The evolution of the saddle shape induced by light irradiation is clearly represented by the developing negative Gaussian curvature, whereas the tipping point of irradiation and maximum curvature vary according to the aspect ratio. I show that shorter length in the direction perpendicular to the nematic direction is preferred for severe anticlasticity generation.

According to the "swimming" LCP sheet experiment [21], which utilizes the instantaneous emergence of anticlasticity upon irradiation, induced curvature is closely related to the energy transfer that drives the swimming. Equation (3.1.1) illustrates a crude estimation of the energy, where Y is the Young modulus, κ is the Gaussian curvature, h is the thickness, and A is the domain area:

$$\frac{E_{est}}{Y} = \frac{A}{24}\frac{h^3}{\kappa} \quad . \qquad (3.1.1)$$

A response of the strain energy shown in Fig. 3.1.3(b) also exhibits non-monotonic behavior. However, a more moderate difference is shown between the energies corresponding to the different aspect ratios, unlike the Gaussian curvature itself. These results assert that the larger aspect ratio is favorable for stronger light intensity in order to achieve the maximal efficiency when the length of the nematic orientation axis is fixed. These findings indicate that designing optimized and efficient actuators requires the investigation of various parameters because stronger light does not necessarily imply more thrusting power, and is strongly affected by geometric conditions.

3.2. Optimum extrinsic property: irradiation pattern

It is likely that a carefully designed nontrivial spatial distribution of the photostrain will generate more intriguing shapes [83], so the prospect exists for it to be realized through the use of modern optical techniques such as filtering [84], masking [85], and local irradiation. To obtain a desirable shape change of the PRP film that is stimulated by a nonhomogeneous distribution of the light irradiation, an eigenstrain-patterning technique that is based on topology optimization is employed here. A topology-optimization scheme is originally applied to obtain an optimal layout regarding the structural design, whereby the minimum compliance that sustains the loading is the main objective for the effective design of the mechanical structure. Because the high versatility of the technique has been proven, other scientific fields [86-90] utilize the optimization technique through modifications of the objective and the constraint function that are physically related to the target materials. For the simulation of the PRP film, the eigenstrain that is induced from the light irradiation is selected as the design variable. The photomechanical fundamentals regarding the light-induced eigenstrain are then investigated, which involves a consideration of the relationship between the light irradiation and the strain generation and the resultant force and moment that lead to the mechanical deformation that is incorporated into the finite element methods [55]. Such design schemes enable the performance of an analysis of non-uniform deformations in terms of the complex behavior in the PRP structure, as well as regarding the design of the proper eigenstrain distribution. The eigenstrain-pattern design for the attainment of a certain predefined deformation is obtained through the use of the topology-optimization methodology for which the pattern solution of the inverse mechanism is found; moreover, this technique can be used to design the eigenstrain distribution of PRP films for the creation of 3D selfassembling structures.

But optimization results of a complex shape and non-uniform intensities are not feasible when the technological capabilities regarding the fabrication of patterns on a material specimen are considered; therefore, to obtain a simplified strain distribution, a material-interpolation scheme is adopted for the pattern-design approach. Bendsoø and Sigmund [91] derived a physically feasible design through a treatment of the gray-scale intensity that is according to the interpolation of the intermediate intensities. The solid isotropic material with penalization (SIMP) model is used to artificially tune the design variable so that the intermediate densities are penalized, and this leads to the attainment of a feasible strain pattern. The design variables are then interpolated to the pseudo-density, whereby the values are bounded from 0 to 1, and these values are directly connected to the light-induced strain.

3.2.1. Methodology based on topology optimization

The objective function that is a squared value of the distance between the target point and the cantilever tip is represented by Eq. (3.2.1), as follows:

$$\boldsymbol{f}_{\mathrm{obj}} = (\boldsymbol{u}_{\mathrm{tip}} - \boldsymbol{u}_{\mathrm{target}})^2 \tag{3.2.1}$$

This objective function was originally proposed by Howard, Pajot, and Dunn as an inverse-design methodology; however, in this research, a forward-design simulation from the flat to the deformed cantilever is performed. An optimized strain pattern is the main goal of topology optimization, and the final deformed shape is obtained later. Design objectives and geometric constraints can also be applied in consideration of the type of strain pattern and the desired geometric functioning.

The design variable that is exerted on each of the four-node overlaid elements that comprise four individual triangular elements is an element-wise eigenstrain; here, the eigenstrain can be induced by photo illumination or thermal change. The order changes of a polymeric chain are coupled with side effects including light and temperature. The reported experimental data shows the complexity of the strain occurrence and the correlation of the external stimuli have not been fully investigated; furthermore, the modeling of light-driven shape changes is mostly expressed with assumed coefficients that are fitted from experimental or computational simulation results [5]. Complicated procedures are omitted from the topology-optimization methodology here, and only the subsequently induced strain from the external stimulation is considered. The order-change process is a time-variant process because the characteristic of the isomerization process is diffusive when such chemical changes occur in localized areas; moreover, such time-dependent properties are neglected, and it is assumed that they occur instantly, leading to the consideration of a static bending problem. In optimization terms, the number of design variables is determined in consideration of the computational time and the pattern-making process.

For an excessive number of elements, a precise control of the gripper is possible, but a convergence risk regarding an ill-conditioned local minimum also arises. This problem is basically of a non-convex nature, and an infinite quantity of local minimums can satisfy the objectives and the constraints; therefore, even for an adequately converged objective value, the solution keeps moving over the solution space and is shifted to another minimum point nearby, where the values of the design variables are almost identical. The proper number of design variables therefore prevents the solutions from wandering between multiple local points, and they are converged rapidly to save the computational cost; conversely, a too-low number of design variables may cause a deficiency of the degree of freedom in terms of the design of the strain pattern, and this leads to an imperfect convergence of the objective functions. The proper number of design variables should therefore be selected.

The applied geometric constraint is the surface curvature of a specific node. The curvature constraint can control the flatness of the cantilever that is related to the bending-shape design of the gripping-cantilever shape and the local photo-inactive area. The surface curvature is obtained using Chen and Schmitt’s method, which is used to calculate the surface curvature of a specific node; here, the positions of the neighbor nodes are used to calculate the surface curvature. Further, triangular meshes should be used for the modeling of a finite-element structure.

For the optimization process, the SIMP method that was suggested by Bendsoø and Sigmund was applied [91] to solve not only the singularity issue, but also the non-convergence and non-existence problems regarding the expression of the solid-void interpolation in isotropic materials. In eigenstrain-based topology optimization, however, and unlike the isotropic materials, the light-induced strains can be discrete and the intermediate intensities can be expressed through the control of the irradiated light intensity. This interpolation scheme is consequently used purely for the cancelation of the intermediate intensity strain, leading to clearly identified boundaries and admissible black-and-white strain-pattern shapes; furthermore, this process provides an admissible strain pattern that can be transformed into a light filter. The design variable ρ is bounded from 0 to 1, and as given by Eq. (3.2.2), its intensity is interpolated according to the order of the penalization parameter p, as follows:

$$\varepsilon_{ph}(\rho) = \varepsilon_{ph,\max} \cdot \rho^{p} \tag{3.2.2}$$

where $\varepsilon_{ph,\max}$ is the maximum light-induced strain, which is 0.2, that is referred from the experimental reports [12]. The penalization parameters are usually set as 3. The total-strain amount, which is a volume fraction in the minimum-compliance problem, is calculated according to the mean value of all of the design variables, which are limited here to the following two cases: 0.5, and 0.8. The total-optimization problem statement can be written as Eq. (3.2.3), as follows:

$$\begin{aligned}&\min_{\rho} f_{obj}\left(\mathbf{u}(\rho)\right)\\&\text{s.t.}\ \ g_{\text{curv}}\left(\mathbf{u}(\rho)\right) - \kappa_m \ \le\ 0 \ \ \text{and}\ \ g_{\text{vol}}\left(\rho\right)\ \le\ S\\&S = \sum_{i=1}^{N} \rho_i\end{aligned} \tag{3.2.3}$$

where g_{curv} and g_{vol} are the constraint function for the surface curvature and the amount of the induced eigenstrain, respectively.

The topology optimization process is conducted using the *fmincon, a* built-in function in MATLAB, for which the interior-point algorithm is selected as a solver. The interior-point algorithm is a commonly used gradient-based solver that can be applied to a variety of problem conditions. The objective function includes the co-rotational formulation and the constraint includes the curvature calculation, whereby the nonlinearity of both cases regarding the design variables is high, and the gripping objective implies non-convexity as well. The treatment of such complications in each iteration, which can cause an instability throughout the entire simulation, leads to the usage of the interior-point algorithm because of its robustness and efficiency. The algorithm moves the solution path through a simultaneous consideration of the gradients of the objective function and the constraints, and this can provide a feasible solution in every iteration.

The sensitivity analysis is performed in the corotational formulation according to the adjoint method that was proposed by Pajot and Maute [92]. For the adjoint method, the pre-calculated stiffness matrix, which mitigates the incurred computational time of the numerical finite-difference scheme that is provided by the built-in MATLAB function, is reused.

$$\begin{aligned}\frac{df_{obj}}{d\rho_i} &= \frac{\partial f_{obj}}{\partial \rho_i} - \frac{\partial f_{obj}^{\mathrm{T}}}{\partial \mathbf{u}}\mathbf{K}_T^{-1}\frac{\partial \mathbf{R}}{\partial \rho_i} \\ \frac{dg_{curv}}{d\rho_i} &= \frac{\partial g_{curv}}{\partial \rho_i} - \frac{\partial g_{curv}^{\mathrm{T}}}{\partial \mathbf{u}}\mathbf{K}_T^{-1}\frac{\partial \mathbf{R}}{\partial \rho_i}\end{aligned} \tag{3.2.4}$$

In Eq. (3.2.4), while partial analytical values can be provided and an objective-function derivative is directly calculated, the residual derivative is not intuitively calculated and should be obtained from the EICR formulation. The partial derivative of the residual is expressed using Eq. (3.2.5), as follows:

$$\begin{aligned}\frac{\partial \mathbf{R}}{\partial \rho_i} &= \frac{\partial \mathbf{f}_{\mathrm{int}}}{\partial \rho_i} - \frac{\partial \mathbf{f}_{\mathrm{ext}}}{\partial \rho_i} = \frac{\partial\left(\mathbf{T}^{\mathrm{T}}\mathbf{P}^{\mathrm{T}}\mathbf{H}^{\mathrm{T}}\overline{\mathbf{f}}_{\mathrm{int}}^{(\mathrm{e})}\right)}{\partial \rho_i} - \frac{\partial\left(\mathbf{T}^{\mathrm{T}}\mathbf{H}^{\mathrm{T}}\overline{\mathbf{f}}_{\mathrm{ext}}^{(\mathrm{e})}\right)}{\partial \rho_i} \\ &= \frac{\partial \mathbf{T}^{\mathrm{T}}}{\partial \rho_i}\left(\mathbf{P}^{\mathrm{T}}\mathbf{H}^{\mathrm{T}}\overline{\mathbf{f}}_{\mathrm{int}}^{(\mathrm{e})} - \mathbf{H}^{\mathrm{T}}\overline{\mathbf{f}}_{\mathrm{ext}}^{(\mathrm{e})}\right) + \mathbf{T}^{\mathrm{T}}\frac{\partial \mathbf{P}^{\mathrm{T}}}{\partial \rho_i}\mathbf{H}^{\mathrm{T}}\overline{\mathbf{f}}_{\mathrm{int}}^{(\mathrm{e})} \\ &\quad + \mathbf{T}^{\mathrm{T}}\left(\mathbf{P}^{\mathrm{T}}\frac{\partial \mathbf{H}^{\mathrm{T}}}{\partial \rho_i}\overline{\mathbf{f}}_{\mathrm{int}}^{(\mathrm{e})} - \frac{\partial \mathbf{H}^{\mathrm{T}}}{\partial \rho_i}\overline{\mathbf{f}}_{\mathrm{ext}}^{(\mathrm{e})}\right) + \mathbf{T}^{\mathrm{T}}\left(\mathbf{P}^{\mathrm{T}}\mathbf{H}^{\mathrm{T}}\frac{\partial \overline{\mathbf{f}}_{\mathrm{int}}^{(\mathrm{e})}}{\partial \rho_i} - \mathbf{H}^{\mathrm{T}}\frac{\partial \overline{\mathbf{f}}_{\mathrm{ext}}^{(\mathrm{e})}}{\partial \rho_i}\right)\end{aligned} \tag{3.2.5}$$

For the design variable, the eigenstrain originates from the light illumination, the elemental external force is the only term that is dependent upon the design variable, and all of the other terms are functions of the nodal displacements and the rotations. The partial derivative of the external forces is consequently the only term that is taken into consideration, making all of the other derivative terms equal to zero, as given by Eq. (3.2.6), as follows:

$$\frac{\partial \mathbf{T}^{\mathrm{T}}}{\partial \rho_i} = \frac{\partial \mathbf{P}^{\mathrm{T}}}{\partial \rho_i} = \frac{\partial \mathbf{H}^{\mathrm{T}}}{\partial \rho_i} = \frac{\partial \bar{\mathbf{f}}_{\mathrm{int}}^{(\mathrm{e})}}{\partial \rho_i} = 0 \tag{3.2.6}$$

Equation (3.2.7) can then be expressed in a simplified form. The derivative of the elemental external forces are calculated directly from the penalized form of the eigenstrain.

$$\frac{\partial \mathbf{R}}{\partial \rho_i} = -\mathbf{T}^{\mathrm{T}}\mathbf{H}^{\mathrm{T}} \frac{\partial \bar{\mathbf{f}}_{\mathrm{ext}}^{(\mathrm{e})}}{\partial \rho_i} \tag{3.2.7}$$

The dimensions of the PRP-cantilever specimen are 80 x 10 x 2 [mm] for the length, width, and thickness, respectively, and it is assumed that the left tip is clamped. The light that is irradiated on the upper surface causes the specimen to bend upward. The nematic orientation is identical regarding the length direction, and the eigenstrain in the perpendicular direction is also considered for the volume-conserving condition from the Poisson's effect [93]. A contraction of the length direction induces an expansion of the y and z directions for a satisfaction of the incompressible material assumption. The Young's modulus and the Poisson's ratio are obtained from the general LCE properties [70]. The aspect ratio of the modeled specimen is 40, which is relatively thick for the adoption of the plate and shell elements for an FEM computation; here, it is assumed that stress does not be exist on the thickness direction, meaning that it can be considered as a two-dimensional plane structure.

The workflow of the present work is now summarized as shown in Table 3.2.1. After parsing of the inputs, problem is setup with dimension, meshes, and the set of the stimuli (either light-depth pair or eigenstrain-depth pair). In this step, the pair of the stimuli is fitted into the effective parameter of the pair of eigenstrain-depth if needed. The Newton-based optimization steps are nested for *fmincon* (MATLAB built-in function) usage, where the internal structural tensors are computed via EICR formalism. When the objective functions and its norm of change for given instances are within the given tolerance (TOL), the computation is then terminated, followed by post-processing. Note that the two separate kinds of model describe the bending behavior of the PRP herein: One is a light-order coupled model described in the chapter 2.3.1, and the other is a simplified model that is used in topology optimization. Each model accepts different stimuli in this study, which are the light intensity and the photo-induced eigenstrain, respectively. A connection between the light and the strain should be established to convert the optimized solution into the light intensity that is the controllable stimulus in the experimental field. The difference between the two models is the order-dependent material property of the light-order coupling model, whereby the bending stiffness changes with the nematic-order changes that are caused by the external stimuli; furthermore, the bending moment is not proportionally increased with the increasing of the light intensity because the light-penetrating profile comprises a form of the Lambert-W function. The curvature is tabulated with I_o and d, while d is fixed to produce a 1-to-1 correspondence between the photostrain and the light intensity. It is known that d is related to the polymeric conformation and the cross-link ratio, and this enables its use as a fixed value in this study. The tabulation of such correspondence is executed *a priori* to reduce a computational time, and used only when specified, which is presented as a *photomechanics* flag.

3.2.2. Numerical examples on light-fueled gripper

Under the contact condition, the displacement of the specimen tip is equal to the value of the designated target displacement to ensure that the tip reaches the pinching location. The tip displacement is selected at the center point of the cantilever tip, and the target displacement is the initial distance between the selected center tip point and the designated target point. The objective function is the squared value of the distance from the target point to the pinching position in the cantilever tip, as mentioned in Eq. (3.2.1); therefore, the convergence of f_{obj} to the minimum is equivalent to the self-contact that occurs in the pinching position that is located above the clamped root at a height of 50.93 [mm] For multiple specimens with optimized bending behaviors, the gripping mechanism is considered to be satisfied. The initial value setting of the design variables is homogeneous (ε_o^{ph} = 0.2). By using the interior-point optimizer, the decrease of f_{obj} that is presented in Fig. 3.2.1(a) occurs; however, the convergence trend differs significantly.

To demonstrate the rapid convergence, the objective-function value is shown in the logarithmic scale and settles within approximately hundreds of iterations. The pinching mechanism is considered well-satisfied when $\log_{10}\left(f_{obj}\right) < -2$, as it demonstrates that a distance between the target point and the gripping tip is within 0.1 mm. With such criteria, the objective function converged when S = 0.5 and S = 0.8; when S = 0.5, the optimization stopped within 60 iterations, while the 0.8 value resulted in a repetition of the iterations that is more than a hundred times. Both of the simulations are terminated when the change of the design variable is less than 1e-6, which is represented as the norm value of the design-variable vector; as shown in the insets of the convergence graph, the objective value of the intermediate solutions can be similar or even smaller with the optimized solution. When S is constrained to 0.2, however, the solution does not converge to an optimal minimum point because of an insufficient amount of total strain; the maximum bending moment, which corresponds to the analytic bending moment that is computed by the eigenstrains that are presumably concentrated near the clamped area, shows such an insufficiency.

The eigenstrain pattern that is obtained during the iteration is also presented in Fig. 3.2.1(b). In the early stage of optimization, the strain is evolved in the root area (i.e., near the clamped region), because in the initial state, the movement of the cantilever tip to a target point is efficiently accomplished with the use of a long bending arm that makes it advantageous to exert a strain in the root position; alternatively, when the iteration number is around 30, the pinching point in the cantilever tip moves back and forth near a target point, and the strain pattern shows a collapsed and distorted shape. Such fluctuations of the convergence graph stem from the fact that the suboptimal solutions of the objective function are numerous (i.e., local minimum), whereby a solution point is constantly moving from one local minimum to another. When the value of the design variable that is directly related to the bending-strain amount is being constrained, an excessive amount of induced strain is the risk when numerous solutions are made. The gripping point in the tip may overshoot the target location for the determined step size in the optimization algorithm; in this case, the tip point moves slightly back and forth near the target point. In the final optimized solution, the strain patterns are of a 40 mm length and a form that looks like a half-oval/half-rectangle shape. Although the function value is not fairly converged to the global minimum position when it is compared to previous iterations, the iteration stops according to the criterion whereby the variation of the design variable is smaller than the tolerance.

Additionally, concentrated strain patterns have been performed in the experimental research studies regarding localized irradiation. Programmable bending or folding mechanisms have also been investigated, whereby they were designed and demonstrated using photo-active mechanical applications. This research shows the usefulness of a pattern-design methodology that can be widely connected to the actual development of a mechanical structure.

As light eigenstrain-distribution profiles show consistent pattern shapes, they can be parametrized from their location and size, and they can also be used for the prediction of the pinching point. The constraint of the volume fraction is the total strain amount in the eigenstrain optimization. The SIMP method that facilitates different forms of the strain pattern that provide a variety of solutions is combined into optimization to constrain the penalizing intermediate intensities. While it is concentrated or distributed, the specimen shows a distinct bending behavior and fabrication for the light filter that is also in accordance with a different process regardless of whether its irradiation intensity is of a medium strength or not. The controlling of the constraint value with the SIMP method can result in the drawing of a realizable pattern shape, and because the solution is prevented from wandering around the local minimums, the convergence of the solution is guaranteed. The optimization simulation is performed for the 0.5 and 0.8 volume fractions, and the target point is designated to 0.6 D, where D is defined as the diameter of a circle with a half of the arc length as the length of the specimen, while l represents the cantilever length, ($D = 2l / \pi$)

The optimized strain pattern and the deformed shape are presented in Fig. 8, where the specimen is modeled with 512 design variables. The number of elements are 64 and 8 for each of the horizontal and vertical directions, respectively. For both dense and coarse meshes, the consistency of the converged solution remained under the same simulation condition. The number of design variables was adjusted to prevent an excessive computational-time cost.

Figure 3.2.2(b) shows the strain pattern that was found under different S conditions, where differences of both the shape and the intensity are shown. For the 0.8 case, the distinction between the intense and weak areas is not sufficiently clear and the intermediate intensity area is marked by the red color as a consequence; whereas in the 0.5 case, the boundaries between the two areas are clearly identified and are therefore definitely divided. The strain patterns are concentrated in the localized area, so the bending behavior occurs in the narrow area with a large curvature. The 0.8 case shows the blurry distributed-strain pattern that induces the bending strain throughout the whole specimen; therefore, the bending curvature is smaller than that of the S = 0.5 case, and this small curvature reduces the risk of failure from the wrinkling and the crack generation that are caused by a repeated folding process. It is also possible that an abrupt change of the eigenstrain in the specimen can initiate structural defects, and this necessitates an ongoing consideration of the continuity of the strain intensity.

In addition, the additional curvature-flatness constraint has been imposed to demonstrate the simulation capability of the present work; as shown in Fig. 3.2.3, significantly different bending shapes were obtained. The constraint was applied on the different specimen locations with the target point that is fixed to D. The number of design variables is 128, with 4 for the vertical direction and 32 for the horizontal direction.

Pinching is well-achieved in the three different locations of the curvature constraint. The constraint is applied on multiple points near the selected location, as follows: 10 mm, 20 mm, and 30 mm. For *S* = 0.5, the patterns are split into two pieces, and the values of the black-and-white patterns are converged to 0 and 1, respectively. The numerical fluctuations of the converged values, however, are present within both the intensely irradiated area and the vague area. Although the light-intensity-value differences do not correspond with the major changes of the deformational behavior, they make it difficult to realize and fabricate the light-irradiation pattern. Post-processing is therefore performed through an averaging of the pattern areas, whereby the intensities are equalized while the total strain amount and the deformation profile are conserved. The weak-strain values are set as 0, which is ignorable in the total strain. According to Eq. (3.2.8), $\varepsilon_{\text{post}}$, the average value of the cubed design variables for which the SIMP method is used, is calculated as follows:

$$\varepsilon_{\text{post}} = \varepsilon_{\max} \cdot \frac{1}{N_w} \left(\sum_{i=1}^{N_w} \rho_i^3 \right) \tag{3.2.8}$$

where N_w is the number of design variables that is/are greater than 0.5.

For *S* = 0.8, the intensity does not converge to a consistent value, and it varies uniformly between the 0 and 1 boundaries; therefore, the averaged post-process intensity value is totally collapsed from the original result data, and it is also very difficult to decide the cut-off value for the cancelation of the ignorable intensity because of the intermediacy regarding the existence of the value. Intermediate intensities appear near the tip areas where the effect of the design variable changes. The sensitivity toward the targeting objective is lower when it is close to the tip position, while the distance from the element to the target point, which is considered as the rotating-arm length, determines the sensitivity toward the objective function. The appearance of the enhancement effect of the design variables during each iteration is therefore a far distance from the tip position at first. Although it is not shown here, the sensitivity distribution also shows a localized shape near the root and the constrained area that is similar to the light-intensity distribution.

In terms of the redistributive strains, the deviation of the post-processing strains from the original ones is not conspicuous and the objectives are consequently retained. Obviously, a lower volume fraction is shown here to partly resolve the non-uniqueness problem that is inherent in gripping solutions; that is, a limited total strain-amount condition contracts the solution space regarding the satisfaction of the pinching objective, making the convergence with the optimized solution faster and with less iterations.

The location of the target point is controlled using the versatility of the PRP specimen in terms of the strain patterns. The distance from the cantilever root is changed with the ratio of *D* and the results are presented in Fig. 3.2.4:

Each pattern shows elliptical or rectangular shapes with a rounded apex. Similar to the previous results, in the 0.8 volume fraction, the intermediate (red) area appears between the intense (black) and the weak (white) areas, and a lower volume fraction shows clearly defined boundaries. The strain pattern is moving toward the root direction through an increasing of the height of the target point, while the shape of the elliptical pattern remains. In the 0.5 case, the height of the pattern is longer than the higher target-point case because the structure needs more bending moments for the targeting of a lower point. In Table 3.2.1 and Table 3.2.2, the patterns are parametrized for the location and the intensity profile, and the locations are normalized according to the length of the specimen. In $S = 0.5$, the center position of the strain pattern is calculated through a finding of a position where the cumulative value of the induced strain is half of the total induced-strain intensity; this is performed according to the length and the width, which appear as the x and y directions, respectively. For $S = 0.8$, the strain pattern is fitted to the Gaussian-distribution function in accordance with Eq. (3.2.9), as follows:

$$\varepsilon_w = p_1 \cdot \exp\left(-\left((x - p_2)/p_3\right)^2\right) \tag{3.2.9}$$

where ε_w is the induced strain that is summed for the width direction, and each of the parameters from p_1 to p_3 represent the maximum height, mean, and deviation of the strain intensity, respectively; namely, p_2 determines the location of the strain pattern and p_3 determines a scattering state for the element-wise eigenstrains. This function can be applied to a limited case where intermediate intensities that are concentrated in a lumped shape are shown.

Although the strain distribution in the longitudinal direction is only parametrized and therefore lacks the total pattern-shape information, the overall behavior retains validity in terms of the following objective functions.

Table 3.2.1 and Table 3.2.2 show the trend regarding the changes of the parameters. For S = 0.5, the Y position remains the same on the center position with less than 1 % of error, while the X position decreases as the pinching point moves higher; furthermore, a similar trend is shown for p_2 in terms of S = 0.8. The value of p_1 is the largest at 0.6 D and gradually decreases as the pinching point moves upward. The deviation value of p_3 is the lowest at 0.6 D and increases for the upper pinching point. The monotonic change of p_1 indicates that the maximum strain that is induced is stronger in the lower target point. For the lower target point, the specimen needs to bend more than the higher target, and this is verified in both the p_1 value and the bending deformation of Fig. 3.2.4(a); furthermore, the same trend appears in p_2 and can be explained in the same manner.

A parameter change implies the movement of the pattern location. A p_3 parameter change means that the strain pattern is concentrated at a lower target point, and the explanation for parameter p_1 also applies here. The parameter result provides information regarding the requirement of the lower target point for a more-localized and intense eigenstrain for large bending moments that are intuitively sound. Through this parametric analysis, the location and fitting parameters include information regarding the pattern shape and an effective distribution. It is worth remarking that such monotonic increases/decreases of these parameters suggest that the eigenstrain pattern is obtained whenever the target pinching point is determined; moreover, the present design methodology that incorporates topology optimization into parametric discussions should possibly be extended to the general behavior of the cantilevered PRP strip, as its status as a powerful and effective measure has been proved.

3.3. Changes of intrinsic variables: Texture design for the actuation

A “texture design” refers the alignment that exhibits variation found within in-plane, while uniform in the thickness direction. A brief explanation about the optical textures that minimizes nematic distortion energy (i.e. Frank energy) is firstly given; an evaluation of the distortion energy of the liquid crystal and an estimation an optical texture of the molecular distribution given by energetic measure that ensures the configuration confers with infimum energy to the domain. Numerical solution of 2D flat surface is following the explanation, with essential boundary conditions such as holes (i.e. non-simply connected domain) or inhomogeneity (i.e. disclination core). It is worth to mention that textures of flat surface with intrinsic curvature are computed in nontrivial manner, due to the metric changes of the domain; ref. [18, 30, 94] are recent reports about the curvature-induced disclinations in simply-connected Riemann surface.

3.3.1. Frank elasticity and nematic texture

The generation of an n_o distribution across a domain, which is essential to obtain programmable LCPs, is explained herein. I adopted the term “optical texture” from liquid crystal physics [1], since a liquid crystal deflects a light curve, causing a non-uniform n_o to result in a nontrivial schlieren optical texture, as is often observed in images obtained through polarized optical microscopy [1, 2, 57]. In this research, two distinct types of textures, which have different origins, were examined.

Firstly, I utilized a well-defined texture, which is characterized by a single disclination defect together with its vicinal nematic orientation. The disclination strength m, which roughly indicates the order of symmetry around a defect, is assumed to be arbitrary in such textures, whereas m = ±1/2, ±1 would emerge naturally. This assumption corresponds to the photoalignment technique [32, 33], in which an arbitrary texture is imprinted without considering the stability of the nematics. Equation (3.3.1) describes n_o as a variable field vector that depends on the position (x, y):

$$\left\{ n_x \quad n_y \right\}^T = \left\{ \cos\left(m\theta + c\right) \quad \sin\left(m\theta + c\right) \right\}^T, \tag{3.3.1}$$

where $\theta = \tan^{-1}(y/x)$ and c is an angle constant, which is assumed to be uniform within the material. Next, the textures induced by inhomogeneities were simulated. Unlike in the well-defined texture examples, no explicit description was designated *a priori*; instead, I assumed that the textures were first determined by the liquid crystalline distortion in the uncrosslinked state and that they were fixed only after crosslinking, thereby becoming constant throughout the material. Here, a Frank distortion energy is assumed as an energy that penalize the LC distortion. As shown in Eq. (3.3.2), a standard form of Frank elasticity, where three modes constitute the general distortion: Splay, twist and bend.

$$F_n = \int_\Omega K_1 \left|\nabla \cdot \vec{n}\right|^2 + K_2 \left|\vec{n} \cdot \left(\nabla \times \vec{n}\right)\right|^2 + K_3 \left|\vec{n} \times \left(\nabla \times \vec{n}\right)\right|^2 d\Omega \tag{3.3.2}$$

In the equation, $\vec{n}\left(x\right)$ is a director field, $\left|\bullet\right|$ is a L2-norm of ($\bullet$), and Ω is a domain of interest. Frank constants K_i (i = 1,2,3) are associated with each distortion modes. In this work, we adopt one-constant approximation ($K_1 = K_2 = K_3$) [1, 2, 31] and 2D planar distribution of LC ($n_0 = \left(\cos\theta, \sin\theta\right)^T$), by which the Eq. (3.3.2) degenerates into the Eq. (3.3.3).

$$\theta = \underset{\theta \in (-\pi/2, \pi/2]}{\arg\min} \int_\Omega \left\|\nabla\theta\right\|^2 dA \tag{3.3.3}$$

Note that a non-convex constraint $\left|\vec{n}\right| = 1$ is substituted to the domain of θ, by which complexity of energy minimization is similarly provoked due to its periodicity. Many works has been therefore suggested to solve the equation by numerically [31, 95-97], or analytically [98]. In this work, we follow the literature that utilizes iterative relaxation method [96], inspired by the similarity between the Eq. (3.3.3) with a Poisson problem associated with Laplace operator. The directionality of a liquid crystal is determined by its inhomogeneities and its vicinity. Two types of inhomogeneities, core defects and voids, are discussed herein; these types are distinguishable by the domain continuity, since a simply connected domain becomes non-simply connected if voids are introduced. The anchoring type was chosen to be homeotropic, so that the liquid crystals would be anchored perpendicular to the prescribed location (core) or free boundary (voids), as functionalized nanoparticles are [31, 37].

The microscopic parameters (n_o and r) for mesogen and polymeric state characterization were defined element-wise. This method of definition is equivalent to assuming that each monodomain is allocated to an individual element, which requires that the characteristic length of the element be less than or equal to the experimentally reported characteristic domain size within a polydomain LCP (~5 μm) [1,2]. However, I set the lower bound on the length of each triangular facet to 100 μm due to computational limitations; the mesh dependence of the solution was thereby checked for each texture, since more complex strain and alignment distributions require finer meshes. For the configurations discussed herein, no mesh dependence was observed up to the maximum level of complexity that was investigated in this study.

Textures not defined *a priori* were firstly examined. Compared to special case where analytic solutions are attainable, present study involves more complex prescribed conditions such as simultaneously applied homeotropic LC interaction and arbitrary locations of multiple hedgehog (i.e. $m = +1$) defects. Throughout the computation, homeotropic condition is imposed as a Drichlet boundary condition to the problem, while defect is described by radially distributed director $\vec{n}$ found in the vicinity of the center of the defect. The initial configurations are specified by red, and computed stable LC are displayed by blue lines. . Figure 3.3.1 illustrates the textures (marked by blue lines) that evolved from given anchoring conditions (indicated in red): (a) two $m = +1$ defect cores with central symmetry, (b) two $m = +1$ defect cores with tilted locations, (c) three uniformly distributed $m = +1$ defect cores, and (d) two and (e) three voids with 5 mm radii. In all of these examples, the anchoring conditions were assumed to be homeotropic (i.e., aligned normal to a specified boundary), as in functionalized nanoparticles and surface anchoring. Similar textures are described in the literature [31].

As shown in Fig. 3.3.1(a)-(c), where prescribed hedgehog defects are specified, their stable LC configurations exhibit an additional distortion at the centroid of the prescribed defects; the centers of an emerged distortion are marked by black dots, which are parameterized by strength of defect displayed in the inset of the figures. Note that their strengths are determined by the number of prescribed cores. It is worth noting that a pair of half-integer defects emerges naturally in lowest energy LC configurations in the absence of initial defects, which is possibly computed by analytic conformal transformation method. For the prescribed void cases depicted in Figs. 3.3.1(d) and 3.3.1(e), lines of disclination were created between the voids. All of the disclinations were assumed to be equivalent regardless of their origins, even though additional constraints must be taken into account when defect stability is of interest. Unlike emergent defects, artificially prescribed defects are often caused by inhomogeneities that mechanically anchor one liquid crystal to its neighboring crystals. Thus, artificially prescribed defects and their vicinal orientations are relatively stable and therefore remain fixed.

The shape changes obtained by applying photo- and thermal stimuli to the textures shown in Figs. 3.3.1(a), 3.3.1(b), 3.3.1(c), 3.3.1(d), and 3.3.1(e) are illustrated in Figs. 3.3.2(a), 3.3.2(b), 3.3.2(c), 3.3.2(d), and 3.3.2(e1) and 3.3.2(e2), respectively. The amount of deflection and detailed topography were found to depend significantly upon the number and locations of prescribed defect cores. When two disclinations were applied symmetrically on the LCP surface, yielding the results shown in Fig. 3.3.2(a), elliptical light-induced deformations were obtained with a uniform bulge whose major axis coincided with the line connecting the disclinations with the central m = -1 defect. On the other hand, in the asymmetric case that produced the results depicted in Fig. 3.3.2(b), a highly skewed 3D protrusion was obtained, while the elliptic axis of the bulge was similarly determined by the location of the dislocation core. In addition, the increased number of disclinations that produced the results shown in Fig. 3.3.2(c) generated a further corrugated surface, indicating that various surface configurations could be realized depending on the characteristics of the introduced inhomogeneities. Finally, the results obtained for the LCPs with non-simply connected domains are depicted in Figs. 3.3.2(d), 3.3.2(e1), and 3.3.2(e2), where the first two images correspond to different boundary conditions. Even though the optical textures are similar to those obtained in the cases in which the central void was instead a disclination core (see Figs. 3.3.2(a) and 3.3.2(b)), their deformed shapes are remarkably different; the elliptical apex has been replaced by a local W-shape (clamped) or a local flat region (simply supported), since bending resultants were applied to the void boundaries. Although not shown here due to its straightforwardness, the anchoring effect is also important in design. Specifically, homogeneous anchoring conditions are beneficial since they yield larger deformations, although the textures are topologically equivalent. This difference is attributable to the reversal of the bending resultant direction, which increases the amount of deflection. Such results are predictable from analytic solutions based on metric changes [17,30]. Note that the possibility of the inverse design that bridges the prescription of the inhomogeneity (i.e. the location of fixed hedgehog defect) to the evolved exotic topography of the LCP sheet is of interest in the present study; hence the sensitivity of the stimuli to the configuration is not studied parametrically.

3.3.2. Texture induced exotic shape change

In this section, the photo-responsiveness of the LCP with a well-defined disclination whose core was located at the domain center, was firstly simulated. The alignment vector n_o was fixed separately for each element in which the light-induced strain was defined naturally. After stimulation, local bulge patterns protruded out from the originally flat surface, generated by the interaction between the locally distributed photo-induced bending and the stretching resultant on the midplane. Figure 1 shows selected illustrations of the topographies that resulted from the disclination topology.

When compared with the hill-and-valley surfaces obtained experimentally (Fig. 3.3.3(a)), these simulated surfaces are phenomenologically fairly consistent. I considered two extreme boundary conditions, whose results are shown in Figs. 3.3.3(b) (clamped) and 3.3.3(c) (simply supported). However, it should be noted that experiments are conducted in fluid contact conditions wherein the number of DOFs is constrained by penalization, so experimental environments are equivalent to neither the clamped nor the simply supported boundary conditions.

It is essential to consider geometric nonlinearities to achieve accurate solutions, since many-pole configurations require correct strain measurements. Deformed shapes with simply supported boundary conditions are shown in Figs. 3.3.3(c) and 3.3.4, demonstrating significant nonlinearity. The solution obtained without considering geometric nonlinearities exhibits a shape that is overly simplified compared to those of many-pole confirmations found in solutions obtained by considering geometric nonlinearities.

As shown in the previous literature [5] that compares linear and nonlinear solution for the given amount of stimuli, linear solutions overestimate nodal displacements resulting in energy overestimation, as exhibited by the E/μ versus I_{eff} profile in Fig. 3.3.4(b). Monotonic increases in energy are observable in both the linear and nonlinear cases. The magnitudes of the energy increases, however, differ by four orders of magnitude since rigid-body motion is not considered in the linear solution; such energy-free deformation becomes significant as the symmetry of the texture increases, and thus its consideration is essential when performing computations related to exotic LCP surface formation. In general, a deviation between these two solutions would be diminished in case of moderate deflections (i.e. low optical and thermal stimuli). In the Fig. 3.3.4(a) with $m = -1$ disclination positioned at the center, however, exemplifies the case when nonlinearity becomes severe even at the low light intensity; linear solution dramatically distorts the original mesh because non-consistent tangent stiffness is computed from undeformed configuration, and used consistently. Although not shown here because the linear and nonlinear solutions had the same topographical feature locations and were thus not phenomenologically distinguishable, the energies found in the simply supported cases also differed by four orders of magnitude.

3.3.3. Snap-through instability of LCP with Hedgehog defect

In this section, the photo-triggered instability of a nematic solid is discussed. When imprinted with an $m = +1$ hedgehog defect, an LCP system experiences a radially inwards eigenstrain and deforms following a negative Gaussian curve, as predicted by metric theory [18,30,67] and verified experimentally [33]. Therefore, the LCP shell under light irradiation suffers from geometric instability, similar to a bifurcated thermomechanical shell. In other words, the system alleviates the strain incompatibility by changing into a distinct deformed shape.

In the preceding chapter 2, a capability of the analysis framework concerning primary snap-through behavior is demonstrated. Light and heat stimuli switch the deformation from a sombrero (i.e., Mexican hat) shape to a saddle shape, by considering geometric nonlinearities; a linear solution would fail to capture the transition of the deforming mode and therefore would yield an inconsistent shape. I perform further stability analyses related to the critical light intensity in various conditions. It is the first study where the origin of photo-induced instability has been investigated in an energetic manner; the results demonstrate that simulations can be employed in the design process and reveals the effects of stimuli upon material properties.

As shown in Fig. 3.3.5(a), the abrupt shape change that accompanies the snap-through transition is parameterized by two separate measures. The displacement-based parameter std$W$/mean$W$, [5] utilizes the vertical deflection W of the perimeter nodes. Obtained by scaling the standard deviation of W by the mean of W, a shape transition can be visualized easily and clearly. On the other hand, the energetic criterion d^2E_{el} / dI_{eff}^2, which is the second derivative of the energy E_{el} with respect to

I_{eff}, should be a constant if the strain energy increases quadratically. Interestingly, the critical point, which is defined to be the point at which std$W$/mean$W$ first exceeds 10^{-2}, coincides with the point at which d^2E_{el}/dI_{eff}^2 exhibits a strong discontinuity. This consistency validates the use of std$W$/mean$W$ as a snap-through criterion. Thus, I anticipate that std$W$/mean$W$ can be employed as a design parameter. The accuracy of W relative to the stress measure that is applied in FEA is also advantageous.

Figure 3.3.5(b) illustrates the variation of I_{eff}^{crit} with d for each wrinkling mode, indicating the symmetry of the deformed shapes. For instance, the principal transition mode is that in which a change from a sombrero shape to a saddle shape occurs. Buckled configurations with higher degrees of symmetry were observed whenever I_{eff} was increased beyond I_{eff}^{crit}, which caused greater stress to be induced on the perimeter. An LCP with increased light penetration, by which more significant in-plane membrane shrinkage is induced, also requires less irradiation. The light profiles were found to follow the power series shown in Eq. (3.3.4) strictly, with the parameters that are listed in Table 3.3.1.

$$I_{eff}^{crit} = \alpha\left(d/h\right)^{\beta} + I_{eff}^{\infty} \tag{3.3.4}$$

The present I_{eff}^{crit} results elucidate some of the characteristics of the LCP buckling that is induced by disclination. First of all, they imply that the saddle-shaped mode is the mode that primarily emerges following stimulation [33]. Additionally, d, which is pivotal in determining I_{eff}^{crit}, does not reduce I_{eff}^{crit} to 0 for the higher modes. In other words, I_{eff}^{crit} has a limiting value of I_{eff}^{∞}, which depends upon the buckling mode. Although not shown herein, it has been demonstrated previously [5] that increasing T also does not influence the buckling mode hierarchy. The mode that exhibits the least buckling (i.e., mode 1) is therefore always preferred over the others, provided that the material parameters remain constant.

It should be noted that only even-symmetry wrinkled shapes emerged in this study since I modeled only one-quarter of a circular LCP for efficiency. Therefore, other symmetries, such as three-fold ones, which must be considered to obtain comprehensive maps of the deformations that occur under actinic light, are not discussed herein since the emergence and stability of the different types of buckling were the topics of interest in this research.

In addition to the aforementioned capabilities of the sensitivity analysis, it is worth remarking upon the advantages of the present analysis technique in the context of design. The method discussed herein is relatively simple and is compatible with conventional FEA techniques since it does not requires pre-conditioning, in contrast to the conventional methods, such as analytic ones [96]. The advantages of the proposed technique result from the fact that the global rank deficiency that may cause catastrophic divergence of numerical solutions does not occur in the method presented herein since such behavior results in local instabilities rather than global ones. The intrinsic bending moment produced by the transverse gradient of the shrinkage also prevents divergence, as has been shown previously through pre-defined geometric imperfection analysis [97]. The curve of I_{eff}^{crit} versus $\log_{10}(d/h)$ (see Fig. 3.3.5(b)) again supports this argument, because it is evident that membrane shrinkage is more influential than bending. This assertion is valid because a smaller amount of irradiation intensity is required when the in-plane shrinkage is greater, regardless of the size of the bending moment. LCP configuration with $d/h > 100$, in which case only negligible light decay occurs (i.e., in which the bending moment is negligible), and an LCP configuration with a higher temperature in which the thermal shrinkage uniformly increases with increasing thickness are two illustrative examples.

Lastly, the effects of phase property changes were examined. The phase transition is a roughly second-order transition near T_{NI}^{0}. The transition profile is governed by the material-dependent phase parameters α, ζ, and β, which determine the slope of the curve, the abruptness of the transition, and the location of the transition, respectively. Recent investigations [6,10,11] have revealed that these parameters are influenced by the material properties of the LCP, such as the geometric connectivity of its chains to the photochromic dye, and crosslinking condition changes. Figure 3.3.6 depicts the values of I_{eff}^{crit} at the onset of the primary transition for various α, ζ, and β.

Decreases in α, ζ, and β all cause I_{eff}^{crit} to decrease monotonically, which indicates that the LCP undergoes snap-through when only slight stimuli are applied. According to the results of recent molecular dynamics simulations [6], ζ, which is the most influential parameter among the investigated phase parameters, is a function of the isomerization and the stacking density. Therefore, I anticipate that reducing the isomerization and stacking density would effectively cause LCPs to exhibit snap-through behavior following only slight stimulation, which would increase the actuation efficiency.

The present report, however, does not completely describe post-buckling deformations, since an examination of these deformations is beyond the scope of stability analysis and would require precise knowledge of the rank-deficiency of the stiffness as well as preconditioned displacements. The transition shapes shown in this report should therefore be understood as the deformation modes. More comprehensive global, rather than local, instabilities would be considered, for instance, if the damping energy were to be included numerically in the formulation in order to stabilize an observed C_2 energy discontinuity (see Fig. 3.3.5(a)), as is done in the commercially applied techniques [99].

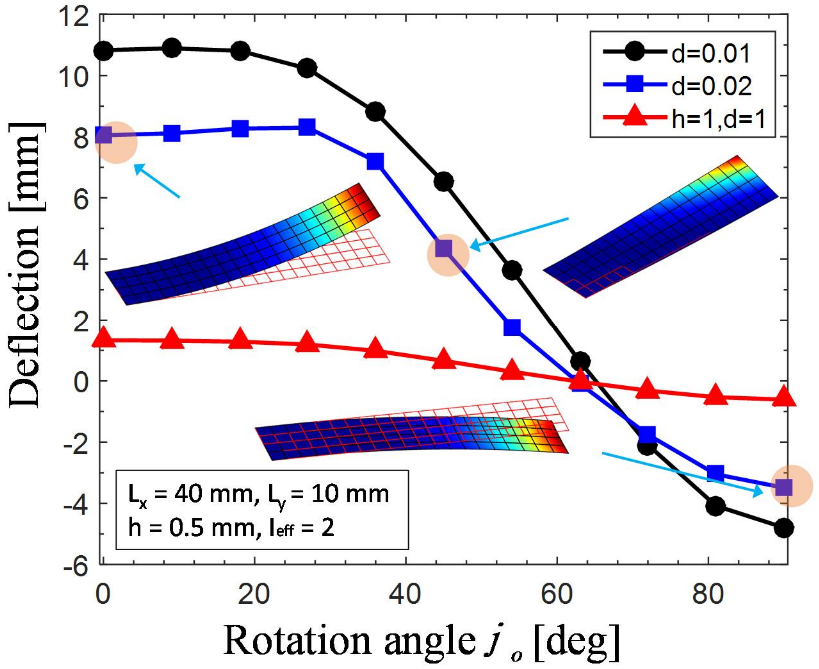

FIG. 3.1.1. Effect of director rotation on the bending direction, and the emergence of twist-bend coupling.

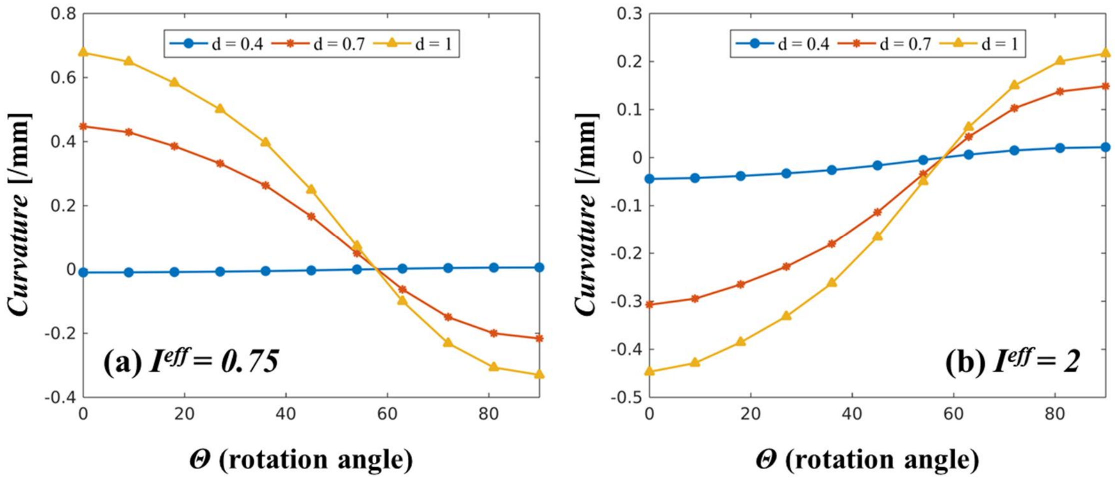

FIG.3.1.2. Alternation of the bending curvature depending on the uniformly deviated angle θ between layer normal $\vec{n}$ and the longitudinal direction, with fixed temperature T = 330 K. The bending direction is found to be strongly dependent on intensity and θ.

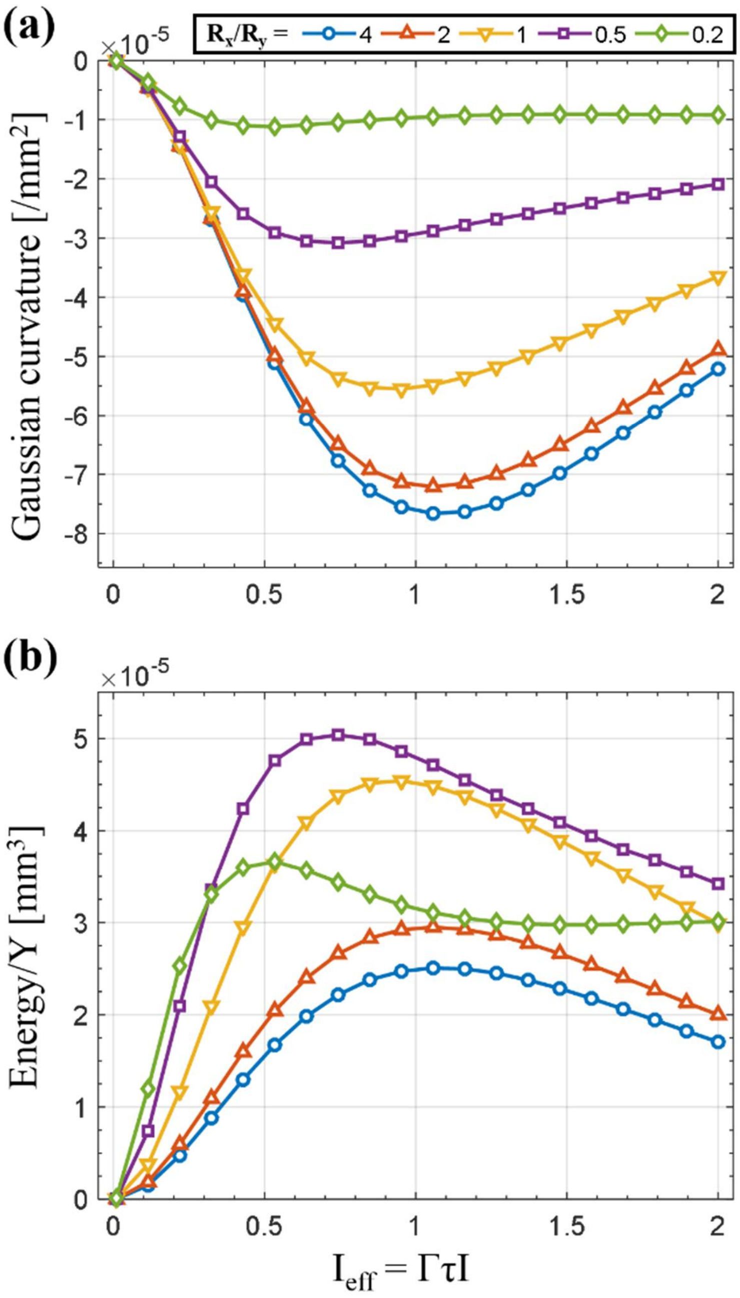

FIG. 3.1.3. "Swimming" non-square LCP sheet under illumination for different aspect ratios R_x/R_y. (a) Gaussian curvature and (b) estimated strain energy scaled by modulus.

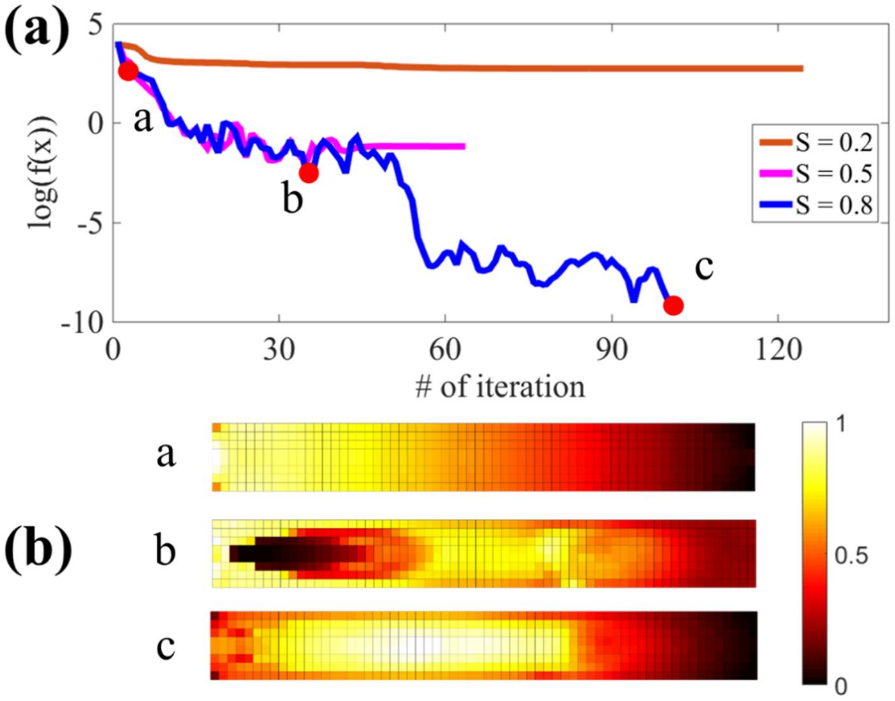

FIG. 3.2.1. (a) Convergence for iteration number and (b) intermediate pattern shapes. Black area indicates no induced strain, white area undergoes maximum light-induced strain, and red and yellow areas indicate intermediate intensities.

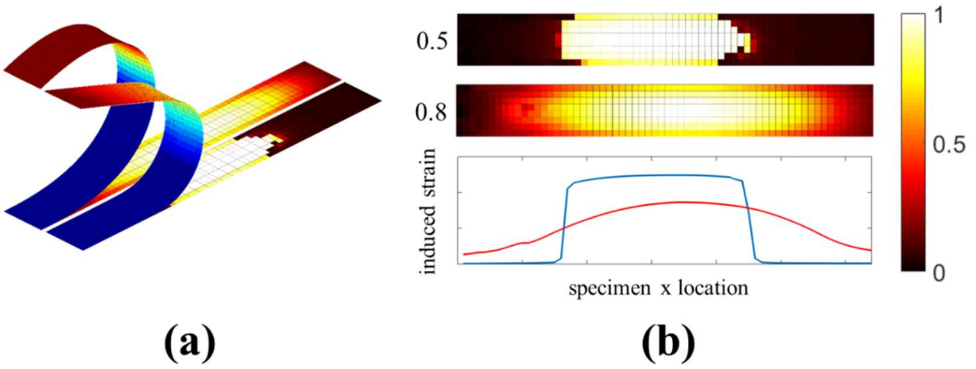

FIG. 3.2.2. (a) Bending behavior and (b) strain distribution with different S constraints. (a) Deformed specimen wherein surface color expresses the height of each element, which is the Z displacement. (b) Intensity graph wherein relative strain intensity is plotted. Blue line indicates $S = 0.5$, red line indicates $S = 0.8$.

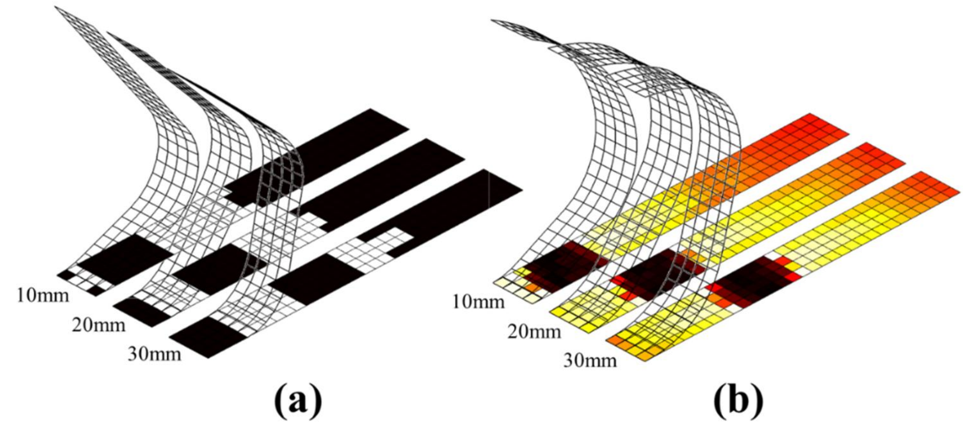

FIG. 3.2.3. Curvature-constrained strain pattern for (a) *S* = 0.4 (strain patterns are post-processed by canceling out small strains and averaging the intense-strain area) and (b) *S* = 0.8. Curvature is constrained for 10 mm, 20 mm, and 30 mm.

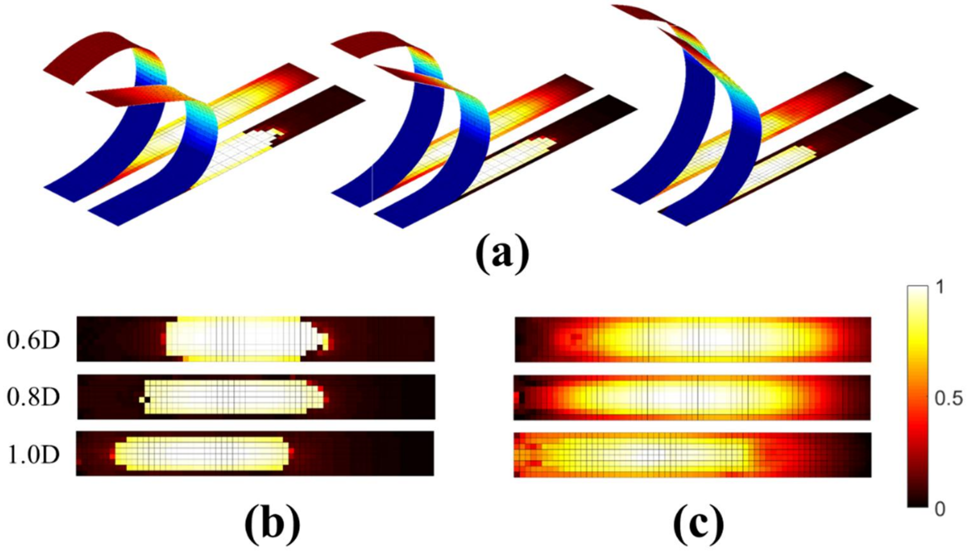

FIG. 3.2.4. (a) Bending behavior of various pinching locations for 0.6 D, 0.8 D, and 1.0 D (from left to right), and strain pattern for: (b) *S* = 0.5 and (c) *S* = 0.8. In (b) and (c), the target location is 0.6 D, 0.8 D, and 1.0 D (from up to down). In deformed specimen of (a), the surface color expresses the height of each element that is the *Z*-displacement.

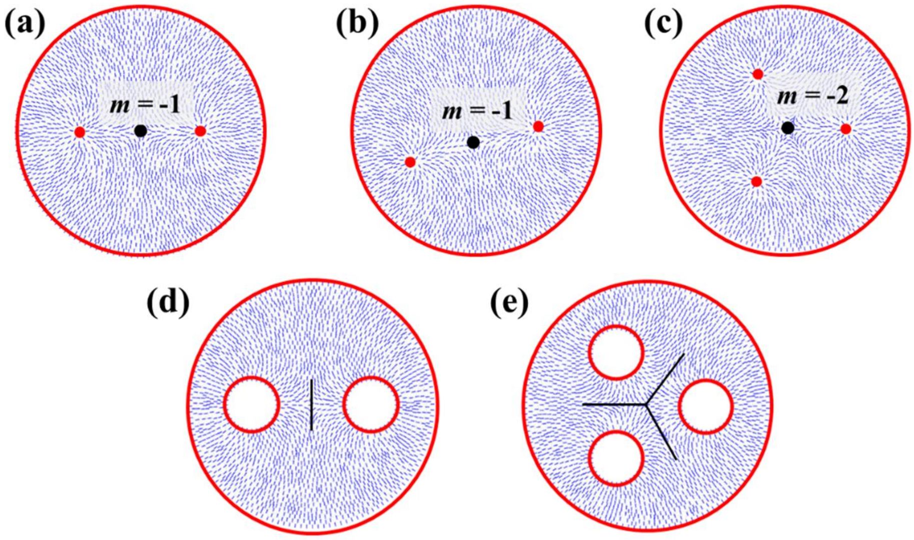

FIG. 3.3.1. Optical textures naturally arising in relaxed state of liquid crystal distortion. Locations at which homeotropic boundary conditions were applied are specified in red, and newly formed disclinations are marked in black. Three prescribed hedgehog defect cases are depicted: (a) two axisymmetric defects, (b) two non-axisymmetric defects, and (c) three axisymmetric defects, and two prescribed void cases are shown: (d) two axisymmetric voids and (e) three axisymmetric voids, each with 5 mm radius.

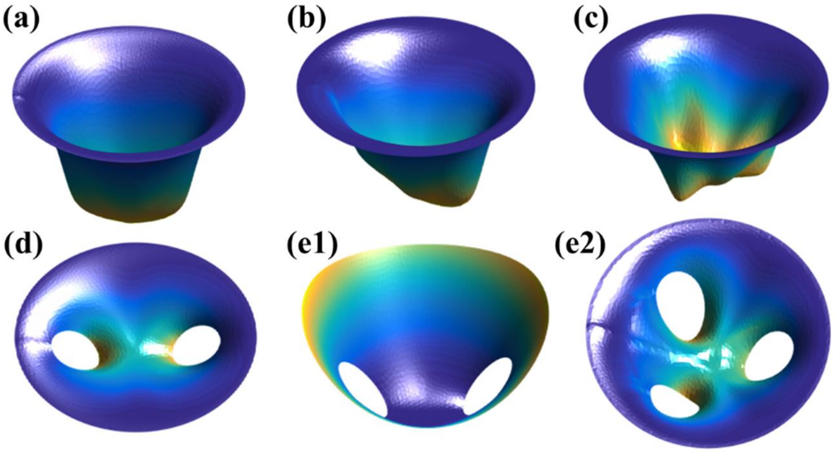

FIG. 3.3.2. Illustration of light-induced deformations whose topographies are indicated by the same alphabetic indicators as in Fig. 3.3.1. Clamped boundary conditions were employed to obtain all images except that shown in (e1).

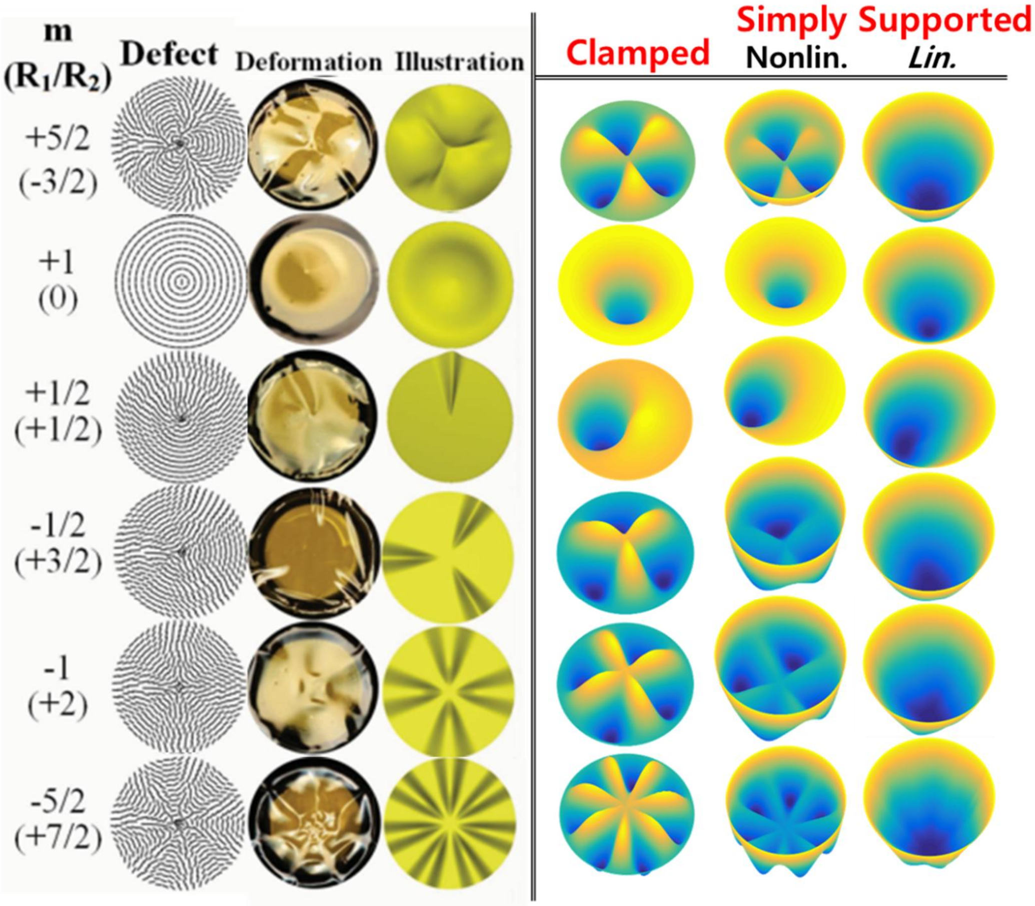
m
(R$_1$/R$_2$)
Defect
Deformation
Illustration
Clamped
Simply Supported
Nonlin.
Lin.
+5/2
(-3/2)
+1
(0)
+1/2
(+1/2)
-1/2
(+3/2)
-1
(+2)
-5/2
(+7/2)

FIG. 3.3.3. Photo-induced textures generated by nematic textures with given disclination core with given strength *m* and anglular constant $c = \pi/2$. Experimental surface topography results (a) were well reproduced by photo-responsive LCP simulations performed using (b) clamped boundary conditions and (c) simply supported boundary conditions. Significant deviation between the nonlinear and linear solutions is observable in (c).

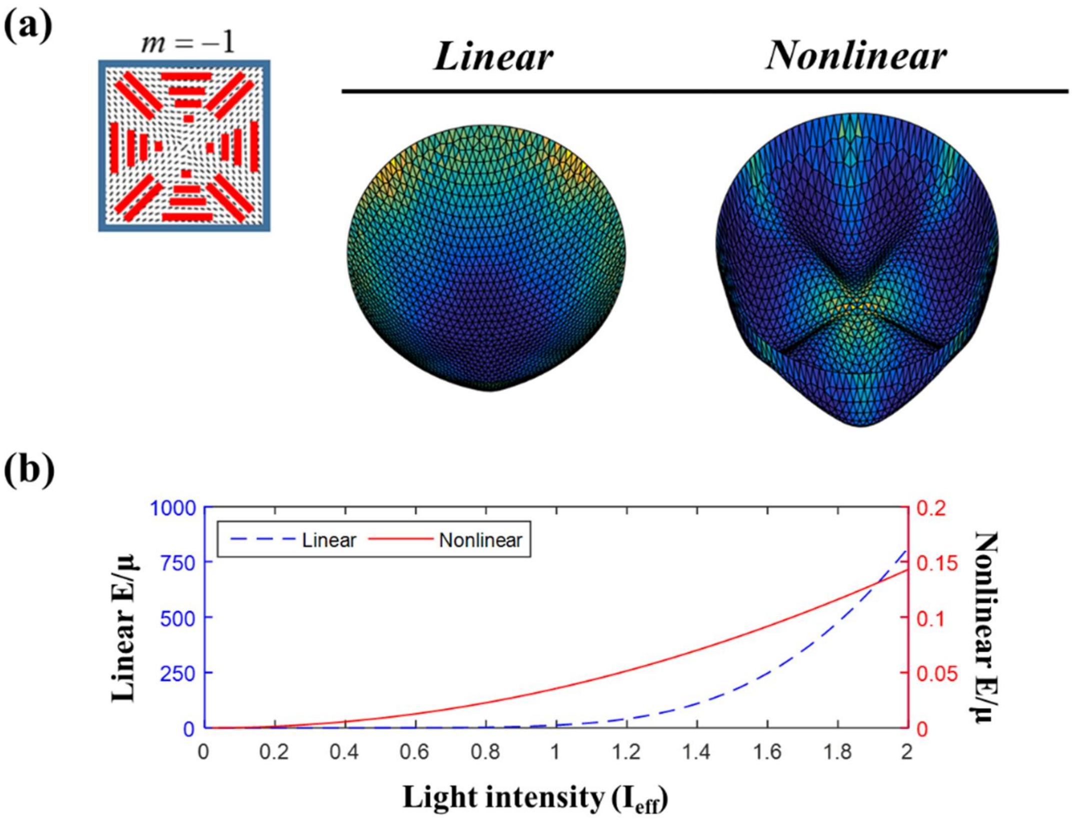

FIG. 3.3.4. Effects of geometric nonlinearities on solution accuracy. (a) Configuration deformed by disclination with m = -1. Nonlinear solution shows accurate quadrupole topography; linear solution exhibits mesh distortion. Elements are colored by strain energy. (b) Scaled strain energy (E/μ) induced by light irradiation. Fourth-order energy differences and non-quadratic energy evolution are observable in linear solution.

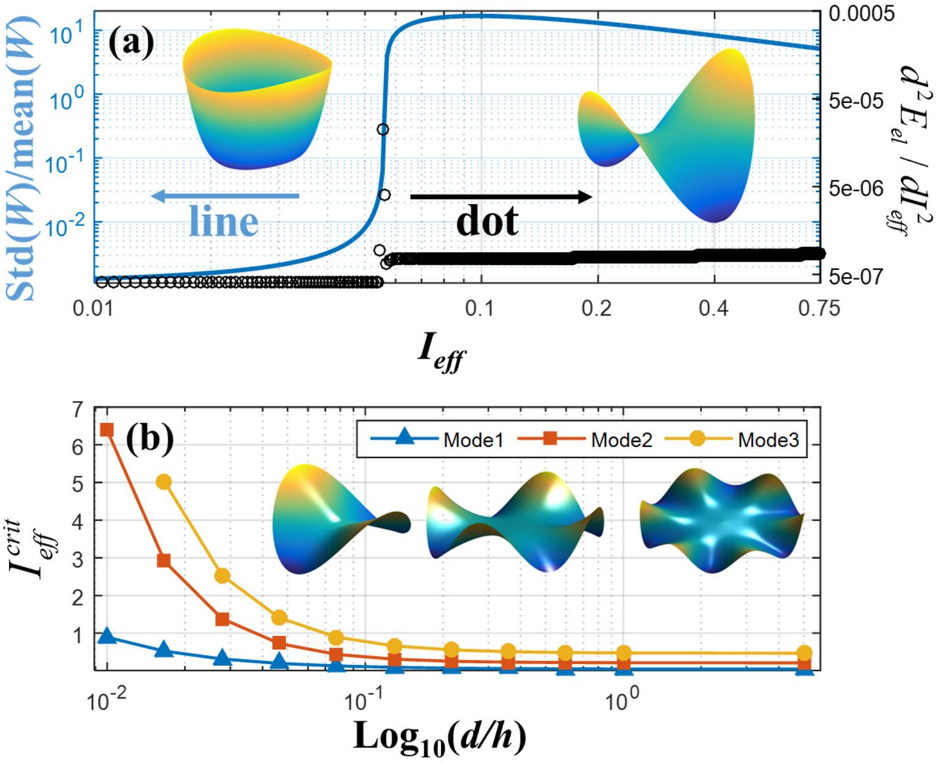

FIG. 3.3.5. Instability-induced shape change of LCP sheet with hedgehog disclination defect. (a) Instability onset locations determined using elastic energy E_{el}- and displacement-based criteria. Insets show deformed shapes before and after bifurcation point. (b) Logarithmic profiles of I_{eff}^{crit} for various penetration depths d divided by thickness h, and transition modes.

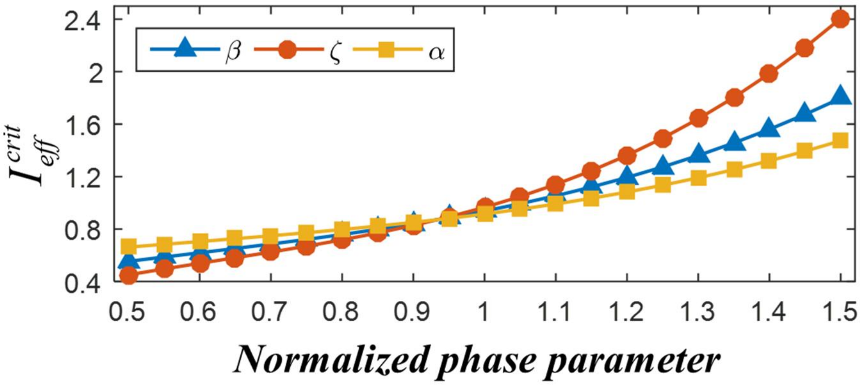

FIG. 3.3.6. Profile of I_{eff}^{crit} for various α, ζ, and β normalized by their original values. Monotonic proportionality is evident, and ζ is the most influential parameter.

Table 3.2.1. Pseudocode of the present work. Hat indices indicate functions

```
Setup dimension, mesh (node, elem), stimuli set: ($\varepsilon^{ph}, d$) or ($I, d$), $u^{\text{target}}$
Initialize the data
        $\varepsilon^{ph}|_o$, $V_o$, $\hat{f}_{obj}\left(u, u^{\text{target}}; \varepsilon^{ph}\right)$, $\hat{f}_{const}\left(u, u^{\text{target}}; \varepsilon^{ph}\right)$
        if photomechanics then
        Obtain effective parameter $\hat{\varepsilon}^{ph}$ and $\hat{d}$ for given set of I, T, and $d$
        end if
For $f_{obj}$ < TOL (10^-8) && $\left\|\Delta f_{obj}\right\|$ < TOL (10^-8)
        $\left[u, \theta, f_{obj}, f_{const}\right] = fmincon(u, \theta, \varepsilon^{ph}(x))$
                For every elem
                Get $C^{CR(e)}, \bar{u}_d^{(e)}, \bar{\omega}_d^{(e)}$, $\bar{\mathbf{K}}^{(e)}\left(\bar{u}_d^{(e)}, \bar{\omega}_d^{(e)}\right), \bar{\mathbf{R}}^{(e)}\left(\bar{u}_d^{(e)}, \bar{\omega}_d^{(e)}\right)$
                Get $\mathbf{K}^{(e)}\left(u^{(e)}, \theta^{(e)}\right), \mathbf{R}^{(e)}\left(u^{(e)}, \theta^{(e)}\right)$
                Assemble $\mathbf{K}(u, \theta), \mathbf{R}(u, \theta)$
                End for
                Get $f_{obj}\left(u; \varepsilon^{ph}\right), f_{const}\left(u; \varepsilon^{ph}\right)$
                Get $\partial f_{obj} / \partial \varepsilon^{ph}, \partial f_{const} / \partial \varepsilon^{ph}$
                Update $u, \theta, \varepsilon^{ph}(x)$ by either SQP or Interior-point
End for
Post-process the output
```

TABLE 3.2.1. Center position of strain pattern in $S = 0.5$

Target	**0.6 D**	**0.8 D**	**1.0 D**
x_c	0.4684	0.4325	0.3597
y_c	0.5039	0.5009	0.5006

TABLE 3.2.2. Gaussian-distribution fitting result for $S = 0.8$

Target	**0.6 D**	**0.8 D**	**1.0 D**
p_1	1.0190	0.8333	0.6829
p_2	0.5510	0.5009	0.3861
p_3	0.3770	0.4146	0.5084

TABLE 3.31. I_{eff}^{crit} fit parameters

Mode	α	β	I_{eff}^{∞}
Mode 1	0.0050	-1.114	0.0441
Mode 2	0.0035	-1.620	0.2126
Mode 3	0.0084	-1.539	0.4676

Chapter 4. Concluding remarks

With light-sensitive molecules incorporated, a light-responsive liquid crystal polymer exhibits exotic coupling between structure and photothermal stimuli, by which the material becomes a hybrid, active material; the mechanical properties are strongly correlated to the optical components found in the material. In the recent years, where a number of the researchers have pushed forward the possibility of such coupling, since they were enticed by the fact that the triggering energy is remotely delivered. Many Interesting works are hence reported that ranges from the theoretical investigation of the mechanisms to the design of the light-responsive maneuvers.

However, there is a less paved road in terms of high-fidelity numerical model although it is essential to predict the material behavior in high-precision and render the material into the product. The model requires the fair account of the interdisciplinary nature of the photomechanical behavior, especially its multiscale characteristics driven by interplay of distinctive physical regimes.

In this regards, the present work investigate the multiscale framework and its extension to the design of such photo-mechanical coupling. The two branches of CAE modeling is hence utilized herein: the finite element model of the photo-responsive liquid crystal polymer and the parametric studies of their exotic behaviors.

In the chapter 1, backgrounds of the liquid crystal polymer structures and its light-responsiveness are introduced, by reviewing references and summarizing them. Firstly, the liquid crystal nature is presented in the view of its optical properties and phase changes induced by various stimuli. The alternating geometry of the liquid crystal is also discussed with respect to the imprinted conformation of the polymeric counterpart as it is essential to understand the phase behavior, where the multiscale nature of the material is originated from. To introduce the possibility of the design of the material, a brief introduction to the synthesis procedures are also illustrated.

In the chapter 2, the multiscale framework to the material modeling is investigated for the first time. A sequential multiscale model of the light-responsiveness is constructed by incorporating coupled constitutive model into the nonlinear shell finite element, where the microscopic information is derived either from molecular dynamics simulations with the light-active interatomic potential, or classical Landau modeling. By combining low-level information into the continuum level of study, the understanding to the characteristics of mesogen crosslinking and its effect to the mechanical behavior is facilitated. It is worth to remark that the geometric nonlinearity is considered as a pivotal constituent for the multiscale modeling to obtain high-fidelity solution, because the local meshes subject to light-induced motions often undergoes severe distortions.

Through seamless multiscale modeling, the present model successfully reproduces the mechanical behavior reported in the various experiments with various optical configurations that ranges from nematic, twisted nematic, and smectic. The constitutive models are constructed for each cases, and their shape change are investigated in terms of the light and thermal stimuli, and the optical properties of the material.

The chapter 3 presents and discusses the prospect of the design of the light-responsive mechanisms, inspired by the fact that the mesogenic traits are fixated during the crosslinking procedure. In this respect, the design parameters are divided into the two categories: the extrinsic and the intrinsic. The former indicates the parameters determined after crosslinking and fixation of the mesogen to the structure, while the latter indicate ones before it.

First of all, the extrinsic modifications, in which the geometric characteristics of the mesogen are fixed, this work present three possibilities: (1) a geometric shape change, (2) a mesogenic alignment modulation, (3) a stimuli patterning obtained by the concept of topology optimization. Note that the last branch of the study is an analogy to the schematic design of the porous material, and it is inspired by the accurate light controllability frequently utilized in the industry.

The intrinsic modification, on the other hand, where the homogeneity of the alignment is severely violated on purpose, is also investigated. The diverse origin may contribute the perturbation, such as a photo-alignment and a doped inhomogeneity (e.g. functionalized nanoparticle). The concept of Shilerene texture and the Frank distortion of the nematic are thoroughly implemented to model the director distribution with high fidelity. As the local director varies to accommodate the perturbations, the eigenstrain induced by light is similarly directed as well. The exotic deformations are hence produced whenever the material is subject to the stimuli, which possibly paves the way to forthcoming inverse solutions of the designated behavior of the light-driven mechanisms.

In summary, these 3 chapters present both the analysis and design of photo-responsive liquid crystal polymers, employing its multiscale and mulitphysical natures that ranges from atomistic van der walls interactions, phase transitions, and continuum modeling. As finite-element models, and variational methods are continuously utilized, the present dissertations possibly provides an efficient and consistent framework to analyze the LCP behavior with the complex internal structures and combined stimuli; hence the design of the novel mechanical elements driven by light is facilitated, whenever large, complex and precise manipulation is a virtue, rather than load-carrying capability. For example, a shutters and controllers of microfluidic systems, microrobotics, and environment –adapting gadgets.

Nevertheless, in spite of the large number of publications –including this dissertation-, it is worth to remark that that the investigations of the numerical modeling and analysis of the LCP-based material is not a closed book; to name a few, a quantum-mechanics coupled to the polymer system wherein mechanical load may enhances or disturbs the geometric kinking induced by isomerization, and robust light-responsive actuators with high load-sustaining capability, which is another branch of the LCP usage. To such aims, many interdisciplinary physical regimes must be considered in depth, including investigations towards a degrees of coupling (e.g. weak vs. strong) between light and structures. For instance, the soft elasticity of the material, of which user may encounter frequently whenever the LCP is subjected to mechanical loading (i.e. not a stress-free condition), has not been integrated within the photomechanical framework. Upon stretch (mechanical loading), the uniaxiality of nematic orientation is violated, and micro-scaled textures evolve. The imposed elastic energy is therefore dissipated through the change of the internal parameter (i.e. director). Such non-convex behavior cannot be attained in the present scheme, as I've presumed infinitesimal rotation of the local director, which is admissible only in stress-free configurations. Both analytic and numeric approaches have been widely investigated, such as quasi-convexation of the total functional or relaxation. However, the seamless integration that is required for complex cases, say mechanical-optical coupled load, is not presented up to present. On the other hand, the present multiscale schematic lacks quantum mechanical consideration attributed to the photoisomerization of an azobenzene chromophore, as noted in the analysis section (Chapter II). Although the light-induced stimulation of the single molecule has been thoroughly investigated in analogy to the Arrhenius model with the aid of energetic barrier between each state, the time gap between molecular transition (~ns) to mechanical behavior (~s) inhibits the integration between quantum mechanics and the present model. To overcome such issue, a large scale quantum mechanical simulation with the many-molecule condition is strongly required, as well as a sequential multiscale framework that bridges the molecular transition and the photon interaction with the atoms.

References

1. de Gennes P-G, Prost J (1995) *The physics of liquid crystals*. Oxford university press
2. Warner M, Terentjev EM (2003) *Liquid crystal elastomers*. Oxford: Clarendon Press
3. Sánchez-Ferrer A, Finkelmann H (2009) Thermal and mechanical properties of new Main-Chain Liquid-Crystalline Elastomers. Mol Cryst Liq Cryst 508:348–356.
4. Corbett D, Warner M (2009) Changing liquid crystal elastomer ordering with light – a route to opto-mechanically responsive materials. Liq Cryst 36:1263–1280.
5. Chung H, Choi J, Yun J-H, Cho M (2015) Light and thermal responses of liquid-crystal-network films: A finite element study. Phys Rev E 91:1–12
6. Chung H, Choi J, Yun J-H, Cho M (2016) Nonlinear photomechanics of nematic networks: upscaling microscopic behaviour to macroscopic deformation. Sci Rep 6:20026
7. Cheng L, Torres Y, Min Lee K, et al (2012) Photomechanical bending mechanics of polydomain azobenzene liquid crystal polymer network films. J Appl Phys 112:013513.
8. Lin Y, Jin L, Huo Y (2012) Quasi-soft opto-mechanical behavior of photochromic liquid crystal elastomer: Linearized stress–strain relations and finite element simulations. Int J Solids Struct 49:2668–2680
9. Jin L, Zeng Z, Huo Y (2010) Thermomechanical modeling of the thermo-ordermechanical coupling behaviors in liquid crystal elastomers. J Mech Phys Solids 58:1907–1927
10. Sánchez-Ferrer A, Finkelmann H (2013) Opto-mechanical effect in photoactive nematic main-chain liquid-crystalline elastomers. Soft Matter 9:4621.
11. Yu Y, Nakano M, Shishido A, et al (2004) Effect of Cross-linking Density on Photoinduced Bending Behavior of Oriented Liquid-Crystalline Network Films Containing Azobenzene. Chem Mater 16:1637–1643.
12. Finkelmann H, Nishikawa E, Pereira G, Warner M (2001) A New Opto-Mechanical Effect in Solids. Phys Rev Lett 87:15501.

13. van Oosten CL, Bastiaansen CWM, Broer DJ (2009) Printed artificial cilia from liquid-crystal network actuators modularly driven by light. Nat Mater 8:677–82.

14. White TJ, Tabiryan NV, Serak SV et al (2008) A high frequency photodriven polymer oscillator. Soft Matter 4:1796-1798

15. van Oosten CL, Harris KD, Bastiaansen CWM, Broer DJ (2007) Glassy photomechanical liquid-crystal network actuators for microscale devices. Eur Phys J E Soft Matter 23:329–36

16. Skandani AA, Chatterjee S, Smith ML, et al (2016) Discrete-state photomechanical actuators. Extrem Mech Lett.

17. Modes CD, Bhattacharya K, Warner M (2010) Gaussian curvature from flat elastica sheets. Proc R Soc A Math Phys Eng Sci 467:1121–1140. doi: 10.1098/rspa.2010.0352

18. Modes CD, Warner M (2011) Blueprinting nematic glass: Systematically constructing and combining active points of curvature for emergent morphology. Phys Rev E 84:021711.

19. Yu Y, Nakano M, Ikeda T (2003) Photomechanics: directed bending of a polymer film by light. Nature 425:145.

20. Adams JM, Warner M (2005) Elasticity of smectic-A elastomers. Phys Rev E - Stat Nonlinear, Soft Matter Phys 71:1–15.

21. Camacho-Lopez M, Finkelmann H, Palffy-Muhoray P, Shelley M (2004) Fast liquid-crystal elastomer swims into the dark. Nat Mater 3:307-310

22. Jiang HY, Kelch S, Lendlein a. (2006) Polymers Move in Response to Light. Adv Mater 18:1471–1475

23. Chen M, Xing X, Liu Z, et al (2010) Photodeformable polymer material: Towards light-driven micropump applications. Appl Phys A Mater Sci Process 100:39–43.

24. Torras N, Zinoviev KE, Camargo CJ, et al (2014) Tactile device based on opto-mechanical actuation of liquid crystal elastomers. Sensors Actuators, A Phys 208:104–112.

25. Priimagi A, Shimamura A, Kondo M, et al (2012) Location of the Azobenzene

moieties within the cross-linked liquid-crystalline polymers can dictate the direction of photoinduced bending. ACS Macro Lett 1:96–99.

26. Li C, Lo CW, Zhu D, et al (2009) Synthesis of a photoresponsive liquid-crystalline polymer containing azobenzene. Macromol Rapid Commun 30:1928–1935.
27. Serak S, Tabiryan N, Vergara R, et al (2010) Liquid crystalline polymer cantilever oscillators fueled by light. Soft Matter 6:779–783.
28. Iamsaard S, Aßhoff SJ, Matt B, et al (2014) Conversion of light into macroscopic helical motion. Nat Chem 6:229–235.
29. Cheng F, Zhang Y, Yin R, Yu Y (2010) Visible light induced bending and unbending behavior of crosslinked liquid-crystalline polymer films containing azotolane moieties. J Mater Chem 20:4888–4896.
30. Pismen LM (2014) Metric theory of nematoelastic shells. Phys Rev E 90:4–8.
31. Zakharov a. P, Pismen LM (2015) Reshaping nemato-elastic sheets. Eur Phys J E 38:1–4.
32. McConney ME, Martinez A, Tondiglia VP, et al (2013) Topography from topology: photoinduced surface features generated in liquid crystal polymer networks. Adv Mater 25:5880–5.
33. de Haan LT, Sánchez-Somolinos C, Bastiaansen CMW, et al (2012) Engineering of complex order and the macroscopic deformation of liquid crystal polymer networks. Angew Chem Int Ed Engl 51:12469–72. doi: 10.1002/anie.201205964
34. Li Y, Pruitt C, Rios O, et al (2015) Controlled shape memory behavior of a smectic main-chain liquid crystalline elastomer. Macromolecules 48:2864–2874.
35. Nealon GL, Greget R, Dominguez C, et al (2012) Liquid-crystalline nanoparticles: Hybrid design and mesophase structures. Beilstein J Org Chem 8:349–370.
36. Sánchez-Ferrer A (2011) Light-induced disorder in liquid-crystalline elastomers for actuation. In: SPIE Nanosci. Eng. International Society for Optics and Photonics, p 810702
37. Sun Y, Evans JS, Lee T, et al (2012) Optical manipulation of shape-morphing elastomeric liquid crystal microparticles doped with gold nanocrystals. Appl Phys

Lett 100:1–5.

38. Mukherjee PK (2014) Isotropic to smectic-A phase transition: A review. J Mol Liq 190:99–111.

39. Clarke S, Hotta a., Tajbakhsh a., Terentjev E (2001) Effect of crosslinker geometry on equilibrium thermal and mechanical properties of nematic elastomers. Phys Rev E 64:61702.

40. Yu Y, Nakano M, Maeda T, et al (2005) Precisely Direction-Controllable Bending of Cross-Linked Liquid-Crystalline Polymer Films by Light. Mol Cryst Liq Cryst 436:281/[1235]-290/[1244].

41. Yu Y, Nakano M, Shishido A, et al (2004) Effect of Cross-linking Density on Photoinduced Bending Behavior of Oriented Liquid-Crystalline Network Films Containing Azobenzene. Chem Mater 16:1637–1643.

42. Zhang Y, Xu J, Cheng F, et al (2010) Photoinduced bending behavior of crosslinked liquid-crystalline polymer films with a long spacer. J Mater Chem 20:7123.

43. Wang DH, Wie JJ, Lee KM, et al (2014) Impact of Backbone Rigidity on the Photomechanical Response of Glassy, Azobenzene-Functionalized Polyimides. Macromolecules 47:659–667.

44. Cheng F, Yin R, Zhang Y, et al (2010) Fully plastic microrobots which manipulate objects using only visible light. Soft Matter 6:3447.

45. White TJ, Broer DJ (2015) Programmable and adaptive mechanics with liquid crystal polymer networks and elastomers. Nat Mater 14:1087–98.

46. Sánchez-Ferrer A, Merekalov A, Finkelmann H (2011) Opto-mechanical effect in photoactive nematic side-chain liquid-crystalline elastomers. Macromol Rapid Commun 32:671–8.

47. Skacej G, Zannoni C (2012) Molecular simulations elucidate electric field actuation in swollen liquid crystal elastomers. Proc Natl Acad Sci 109:10193–10198.

48. Urayama K, Honda S, Takigawa T (2006) Slow dynamics of shape recovery of disordered nematic elastomers. Phys Rev E 74:41709.

49. Corbett D, Warner M (2007) Linear and nonlinear photoinduced deformations of

cantilevers. Phys Rev Lett 99:174302.

50. Corbett D, Warner M (2008) Bleaching and stimulated recovery of dyes and of photocantilevers. Phys Rev E 77:51710.

51. Serra F, Terentjev EM (2008) Nonlinear dynamics of absorption and photobleaching of dyes. J Chem Phys 128:224510.

52. Wang H, Lee KM, White TJ, Oates WS (2012) Trans-cis and trans-cis-trans microstructure evolution of azobenzene liquid-crystal polymer networks. Macromol Theory Simulations 21:285–301.

53. Choi J, Chung H, Yun J-H, Cho M (2014) Photo-isomerization effect of the azobenzene chain on the opto-mechanical behavior of nematic polymer: A molecular dynamics study. Appl Phys Lett 105:221906.

54. Hogan PM, Tajbakhsh AR, Terentjev EM (2002) Uv manipulation of order and macroscopic shape in nematic elastomers. Phys Rev E - Stat Nonlinear, Soft Matter Phys 65:41720.

55. Howard M, Pajot J, Maute K, Dunn ML (2009) A computational design methodology for assembly and actuation of thin-film structures via patterning of eigenstrains. J Microelectromechanical Syst 18:1137–1148.

56. Dunn ML (2007) Photomechanics of mono- and polydomain liquid crystal elastomer films. J Appl Phys 102:13506. doi: 10.1063/1.2745063

57. Mbanga BL, Ye F, Selinger J V., Selinger RLB (2010) Modeling elastic instabilities in nematic elastomers. Phys Rev E - Stat Nonlinear, Soft Matter Phys 82:51701.

58. Toshchevikov V, Saphiannikova M, Heinrich G (2011) Light-Induced Deformation of Azobenzene Elastomers: A Regular Cubic Network Model. J Phys Chem B 116:913–924.

59. Xu J, Bedrov D, Smith GD, Glaser MA (2009) Molecular dynamics simulation study of spherical nanoparticles in a nematogenic matrix: Anchoring, interactions, and phase behavior. Phys Rev E - Stat Nonlinear, Soft Matter Phys 79:11704.

60. Katayama K, Choi Y, Kang JW, et al (2014) Depth-selective microscopic observation of a photomobile liquid crystal polymer under UV illumination. Phys

Chem Chem Phys 16:27074–27077.

61. Felippa C a., Haugen B (2005) A unified formulation of small-strain corotational finite elements: I. Theory. Comput Methods Appl Mech Eng 194:2285–2335.

62. Sze K, Liu X, Lo S (2004) Popular benchmark problems for geometric nonlinear analysis of shells. Finite Elem Anal Des 40:1551–1569.

63. Felippa CA (2003) A study of optimal membrane triangles with drilling freedoms. Comput Methods Appl Mech Eng 192:2125–2168.

64. Batoz J-L, Bathe K-Jür, Ho L-W (1981) A study of three-node triangular plate bending elements. Comput Des 13:244.

65. McMillan WL (1973) Measurement of smectic-phase order-parameter fluctuations in the nematic phase of heptyloxyazoxybenzene. Phys Rev A 8:328–331.

66. Biscari P, Calderer MC, Terentjev EM (2007) Landau-de Gennes theory of isotropic-nematic-smectic liquid crystal transitions. Phys Rev E - Stat Nonlinear, Soft Matter Phys 75:1–11.

67. Cirak F, Long Q, Bhattacharya K, Warner M (2014) Computational analysis of liquid crystalline elastomer membranes: Changing Gaussian curvature without stretch energy. Int J Solids Struct 51:144–153.

68. Conti S, DeSimone A, Dolzmann G (2002) Soft elastic response of stretched sheets of nematic elastomers: a numerical study. J Mech Phys Solids 50:1431–1451.

69. Zhu W, Shelley M, Palffy-Muhoray P (2011) Modeling and simulation of liquid-crystal elastomers. Phys Rev E 83:51703.

70. White TJ, Serak S V., Tabiryan N V., et al (2009) Polarization-controlled, photodriven bending in monodomain liquid crystal elastomer cantilevers. J Mater Chem 19:1080.

71. Heinz H, Vaia RA, Koerner H, Farmer BL (2008) Photoisomerization of azobenzene grafted to layered silicates: Simulation and experimental challenges. Chem Mater 20:6444–6456.

72. Cembran A, Bernardi F, Garavelli M, et al (2004) On the Mechanism of the cis-trans Isomerization in the Lowest Electronic States of Azobenzene: S0, S1, and T1. J

Am Chem Soc 126:3234–3243.

73. Brown AW, Adams JM (2013) Numerical study of stretched smectic-A elastomer sheets. Phys Rev E - Stat Nonlinear, Soft Matter Phys 88:1–13.

74. Aßfalg N, Finkelmann H (2001) A Smectic A Liquid Single Crystal Elastomer (LSCE): Phase Behavior and Mechanical Anisotropy. Macromol Chem Phys 202:794–800.

75. Selinger J V., Jeon HG, Ratna BR (2001) Isotropic-Nematic Transition in Liquid-Crystalline Elastomers. Phys Rev Lett 89:4.

76. Adams J, Conti S, DeSimone A (2006) Soft elasticity and microstructure in smectic C elastomers. Contin Mech Thermodyn 18:319–334.

77. Najafizadeh MM, Eslami MR (2002) Buckling analysis of circular plates of functionally graded materials under uniform radial compression. Int J Mech Sci 44:2479–2493.

78. Nishikawa E, Finkelmann H (1997) Orientation behavior of smectic polymer networks by uniaxial mechanical fields. Macromol Chem Phys 198:2531–2549.

79. Yun J, Li C, Chung H, et al (2015) Predicting photoisomerization profile of the highly polymerized nematic azobenzene liquid crystal network: First principle calculation. Chem Phys Lett 627:20–25.

80. Warner M, Modes CD, Corbett D (2010) Suppression of curvature in nematic elastica. Proc R Soc A 466:3561–3678.

81. Harris KD, Cuypers R, Scheibe P, et al (2005) Large amplitude light-induced motion in high elastic modulus polymer actuators. J Mater Chem 15:5043.

82. Chen HT, He LH (2008) Photoinduced surface topography of nematic elastomers: a Green function approach. J Phys Condens Matter 20:285107.

83. Fuchi K, Ware TH, Buskohl PR, et al (2015) Topology optimization for the design of folding liquid crystal elastomer actuators. Soft Matter 11:7288–7295.

84. Wei J, Yu Y (2012) Photodeformable polymer gels and crosslinked liquid-crystalline polymers, Soft Matter. 8:8050.

85. Mamiya J (2012) Photomechanical energy conversion based on cross-linked liquid-

crystalline polymers, Polym. J. 45:239–246.

86. Maute K, Nikbay M, Farhat C (2001) Coupled analytical sensitivity analysis and optimization of three-dimensional nonlinear aeroelastic systems, AIAA J. 39:2051–2061.
87. Wilfredo R, Silva EC, Bordatchev E V, Zeman M (2008) Topology optimized design, microfabrication and characterization of electro-thermally driven microgripper. J. Intell. Mater. Syst. Struct.
88. Kiyono C, Nakasone P, Silva E (2010) Design of piezoelectric laminated shell structures with material gradation and fiber orientation using topology optimization. In: 13th AIAA/ISSMO Multidiscip. Anal. Optim. Conf. P 9098
89. Rodrigues H, Fernandes P (1995) A material based model for topology optimization of thermoelastic structures. Int J Numer Methods Eng 38:1951–1965.
90. Ozaki T, Nomura T, Fujitsuka N, et al (2014) Topology optimization using multistep mapping from 2D photomask to 3D structure for designing reinforcing rib. Sensors Actuators A Phys 215:130–135.
91. Bendsøe MP, Sigmund O (1999) Material interpolation schemes in topology optimization. Arch Appl Mech 69:635–654.
92. Pajot JM, Maute K (2006) Analytical sensitivity analysis of geometrically nonlinear structures based on the co-rotational finite element method. Finite Elem Anal Des 42:900–913.
93. Pajot JM, Maute K, Zhang Y, Dunn ML (2006) Design of patterned multilayer films with eigenstrains by topology optimization. Int J Solids Struct 43:1832–1853.
94. Geng J. Self-assembly, elasticity and orientational order in soft matter (Doctoral dissertation, Kent State University).
95. Adler JH, Atherton TJ, Emerson DB, MacLachlan SP (2015) An Energy-Minimization Finite-Element Approach for the Frank--Oseen Model of Nematic Liquid Crystals. SIAM J Numer Anal 53:2226–2254.
96. Alouges F (1997) A New Algorithm For Computing Liquid Crystal Stable Configurations: The Harmonic Mapping Case. SIAM J Numer Anal 34:1708–1726.

97. Vitelli V, Nelson DR (2006) Nematic textures in spherical shells. Phys Rev E 74:021711.

98. Faetti S (1987) Azimuthal anchoring energy of a nematic liquid crystal at a grooved interface. Phys Rev A 36:408–410.

99. de Borst R, Crisfield MA, Remmers JJC, Verhoosel CV (2012) *Nonlinear Finite Element Analysis of Solids and Structures*. Wiley, New York

국문 요약

액정 고분자 (liquid crystal polymer)란 액정의 특성을 갖는 단분자 (monomer)가 화학적인 과정을 통하여 고분자화 된 것으로, 액정의 광학적, 기계적 특성이 고분자 내에서 잔존하는 특성을 갖는다. 이 중 하나가 상전이 현상과 관련된 지능재료적 성질로, 외부 자극으로 인해 변형되는 액정의 상이 고분자 내 사슬의 기하학 구조 (conformation)에 영향을 미침에 따라 전체 구조체의 거시적 변형을 유발하는 현상을 의미한다.

본 논문에서는 그 중 자외선 파장 대역의 빛과 열원의 조합으로 인해 발생하는 광반응 액정 고분자의 기계적 특성에 집중하여, 광-상전이-기계 거동 간의 연성현상이 고려된 멀티스케일 유한요소 모델을 제시하고자 하였다. 이는 기존의 단독 스케일에서의 해석을 통합한 것으로, 낮은 스케일에서 발생하는 분자 구조의 변화 및 액정상의 변화에 대한 정보를 거시 스케일에서 적용함으로써 촉발되는 기계적 거동을 해석하는 모델이다. Corotation formulation 기반 3차원 비선형 쉘 유한요소 해석을 이용하여 변형과정에서 유발되는 기하비선형성을 고려하였으며, 이와 더불어 분자스케일에서 발생하는 상전이 비선형이 동시에 구성 방정식 내의 변수로 도입되었다. 다수의 수치적 결과를 통하여 이와 같은 멀티스케일 모델은 기존 단독 스케일, 선형 모델에서는 해석이 불가하거나, 과소평가된 결과를 바로잡는 해를 제시하는 것을 확인할 수 있었다.

설계 과정에서는 구축된 모델과 실제 실험 및 설계 간의 관계를 확인하고자 구조체의 변인에 따른 파라메트릭 연구를 수행하였다. 액정 고분자의

제작 과정에 착안, 액정상의 변형에 영향을 미칠 수 있는 변인을 내부 변인 (intrinsic parameter), 액정상이 고정된 뒤의 변인을 외부 변인 (extrinsic parameter)로 분류하였으며, 이와 같은 분류에 따라 해석된 해를 제시하였다. 외부 변인으로는 구조체의 기하학적 형태와 광량의 변화 등을 선정하였으며, 특히 후자의 경우 위상최적화 기법에 근거하여 원하는 변형 형상에 대한 최적화된 광량의 패턴을 도출하였다. 내부 변인으로는 내부 액정상의 배향을 선정하고, 변인의 변화가 수반하는 변형 양상을 확인하였다. 이는 광학적 특성이 액정 고분자의 설계 시 회위 결함 (disclination defect)이나, 삽입된 나노 입자 (nanoparticle) 등을 이용하여 개질 가능하다는 것을 상기해 볼 때 의미가 있다 하겠다.

본 논문에서 제안하는 멀티스케일 해석과 이를 이용한 설계 모델은 액정고분자의 특이 거동을 해석하는 데에 있어 해석과정의 수월성은 물론 다양한 비선형 거동을 수월하게 해석할 수 있는 장점이 있다. 특히 광반응 액정 고분자가 마이크로 로보틱스나 유동 제어와 같이 고립, 미소계의 원거리, 대변형이 필요한 환경에서 매력적인 재료로 손꼽히고 있는 것을 상기할 때 향후 이에 대한 해석과 설계를 수행하는데 이바지를 할 것으로 기대된다.

주요어: 액정 고분자, 유한 요소 해석, 멀티스케일 해석, 민감도 해석, 기계적 불안정성, 최적화

학번: 2010-24073